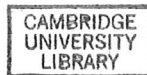


PhD. 33495

BENDING AND BUCKLING OF A
FALLING VISCOUS THREAD

Maurice John Blount
Churchill College



This dissertation is submitted for the degree of Doctor of Philosophy,
University of Cambridge

September 2010



The research described in this thesis was performed in the Institute of Theoretical Geophysics, Department of Applied Mathematics and Theoretical Physics at the University of Cambridge between October 2006 and September 2010 and was supervised by Professor John Lister.

This dissertation is the result of my own work and, except for the usual student-supervisor discussions, includes nothing which is the outcome of work done in collaboration. No part of this thesis has been submitted for any qualification other than the degree of Doctor of Philosophy at the University of Cambridge.

A manuscript based on the material in chapters 4 and 5 has been submitted to the *Journal of Fluid Mechanics*.

Cambridge, September 2010

ACKNOWLEDGEMENTS

I would like to thank a number of people for their help and support throughout the preparation of this thesis. First and foremost, I am grateful to my supervisor, John Lister, for his help and encouragement. He has always been happy to hear of my progress and to provide insight and guidance where needed. I am particularly thankful for his thorough and constructive feedback on earlier drafts of this thesis, which has resulted in a thesis that is much easier to read. I have learnt a lot through working with him.

The presence of an active and friendly Fluid Mechanics community at DAMTP has greatly enhanced my time here. Particular thanks go to Chris Cawthorn, Dominic Vella, Andrew Wells and Rob Style for their company and encouragement as we worked in our corner of Pavillion H, and for their provision of (and numerous contributions to) the 'ITG Quote Board'.

I would also like to thank Daisuke Takagi for his assistance in binding this thesis, and for providing me with some logistical footsteps to follow as I prepared to submit it. While typesetting this thesis I made use of a \LaTeX style file, and I acknowledge Dirk Notz, who I believe was its original author.

I should also thank my family for their support over the years, and Churchill College Boat Club for keeping me in shape. Finally, I gratefully acknowledge financial support from EPSRC, DAMTP and Churchill College.

ABSTRACT

This thesis analyses the behaviour of a slender viscous thread as it falls through air from a nozzle and lands on a solid surface, whereupon it bends and twists. If the diameter of the nozzle is much smaller than the height of fall, then numerical solution of a slender-thread model yields predictions in good agreement with experiment. Moreover, if the thread falls through a height large enough that extensional forces are important, then bending forces are significant only in a small region near the point of impact and negligible in the remainder of the thread, which forms a 'tail'. In this thesis the effects of bending forces near the point of impact are examined by means of asymptotic analysis in the limit of a very slender thread and the key processes that govern the behaviour of such threads is elucidated.

The analysis focuses on three particular physical problems that have recently been studied experimentally. The first problem concerns the steady motion of a thread as it lands on, and is dragged sideways by, a horizontally moving belt. It is shown herein that there are three distinct asymptotic regimes which correspond to the belt speed being faster than, slower than or roughly equal to a 'free-fall' speed at the bottom of the tail. Solutions are obtained for each regime, which provide good predictions of the shape and dragout distance of the thread.

The second problem concerns the stability of such a steadily dragged thread to transverse meandering. It is shown that meandering is caused by bending forces near the impact point, which cause the thread to slump slowly sideways, and the restoring tension in the tail, which is pinned at the nozzle. The competition between these effects and the structure of the eigenmode is analysed, and quantitative asymptotic estimates are obtained for the onset of meandering and the frequency of meandering at onset.

The third problem concerns steady coiling of a viscous thread as it lands on a stationary surface. Provided the fall height is not too small, steady coiling is known to fall into one of three distinct regimes, depending on the relative importance of gravity and inertia within the thread. The asymptotic structure of the thread near the contact point is determined in each regime, and the role of bending forces in this region is analysed. In particular, an analysis of the interaction between the region of bending forces and the 'tail' yields quantitative estimates for the coiling frequency and radius.

CONTENTS

1	Introduction	1
1.1	The deformation of slender viscous and elastic bodies under applied stresses and torques	2
1.1.1	Stretching under applied longitudinal stresses	2
1.1.2	Bending and twisting under applied torques	3
1.2	The buckling instability of slender threads and sheets under compression . .	3
1.2.1	Slender-sheet models	4
1.2.2	Periodic folding of viscous sheets	4
1.3	Outline of thesis	5
2	Slender thread approximation	7
2.1	Geometry of the centreline	8
2.2	Velocity and angular velocity in the thread	9
2.3	Stress and stress-moments in the thread	12
2.3.1	Constitutive relations	12
2.3.2	Stress balance	15
2.3.3	Stress-moment balance	16
2.4	Discussion	17

3	Falling viscous threads	19
3.1	Steady vertical fall of an infinitely long viscous thread	21
3.1.1	Gravity-viscosity balance	21
3.1.2	The relevance of inertia	22
3.2	Nondimensionalisation	24
3.2.1	Dimensionless governing equations	25
3.2.2	Significance of parameters	26
3.3	Stress-free vertical fall of a viscous thread of finite height for $Fr \ll 1$	27
3.4	The effects of small forces exerted at the bottom of the thread for $Fr \ll 1$.	30
3.4.1	Deceleration due to a small vertical force	30
3.4.2	Deflection due to a small horizontal force	31
3.5	Vertical fall of an inertia-dominated thread for $Fr \gg 1$	32
3.5.1	The free-fall speed of an inertia-dominated thread	33
3.5.2	Deceleration due to a vertical force	33
3.6	The whirling of a viscous thread	34
3.6.1	Constant radius	35
3.6.2	Non-constant radius	38
3.7	Discussion	40
4	Steadily-dragged threads	42
4.1	Introduction	42
4.2	Problem description	44
4.2.1	Numerical solution	45
4.3	Asymptotic behaviour of a slender thread	46
4.3.1	Boundary-layer structure	47
4.4	Compressional heel: $U_b < U_f$	49
4.5	Gravitational heels: $U_b \approx U_f$	50
4.6	Curvature-adjustment layer: $U_b > U_f$	56
4.6.1	Perturbation to the tail	58
4.6.2	Boundary layer at the nozzle	59
4.7	Dragout distance of asymptotic solutions and full numerical solutions	61
4.8	Discussion	62
5	Stability analysis of a dragged thread	64
5.1	Introduction	64
5.2	Perturbation equations	67
5.2.1	Numerical solution	69
5.3	Asymptotic solution for the perturbation eigenmode as $\epsilon \rightarrow 0$	69
5.3.1	Matching conditions towards the tail, $1 \ll \eta \ll L_\delta$	70

5.4	Estimation of onset and frequency of instability	71
5.5	Quantitative estimates	72
5.6	Discussion	75
6	Steady fluid coiling	77
6.1	Introduction	77
6.2	Steady fluid coiling	80
6.2.1	Problem description	80
6.2.2	Boundary conditions	81
6.2.3	Numerical solution	82
6.3	Boundary-layer structure	84
6.3.1	Twisting motion in the tail	85
6.4	Inertia-dominated coiling for $Fr \gg \epsilon^{1/2}$	86
6.4.1	Stress and length scalings	86
6.4.2	Matching the bending stresses towards the tail	87
6.4.3	Estimates of the coiling speed and frequency	89
6.4.4	Stress exerted by the coil	91
6.5	Gravity-dominated coiling for $Fr \ll \epsilon \ln \epsilon$	93
6.5.1	Stress and length scalings	95
6.5.2	Matching the bending stress towards the tail	95
6.5.3	Pinning of thread at the nozzle	96
6.5.4	Asymptotic structure of the coil for $0 < \epsilon \ll 1$	97
6.5.5	Estimates of the coiling frequency and radius	101
6.6	Inertio-gravitational coiling for $Fr \sim \epsilon \ln \epsilon$	103
6.6.1	Stress and length scalings	104
6.6.2	Forcing of the tail by the coil away from resonance	104
6.7	Summary and discussion	105
7	Closing remarks	110
7.1	Summary of results	110
7.2	Future work	112
	Bibliography	113

5.4	Estimation of onset and frequency of instability	71
5.5	Quantitative estimates	72
5.6	Discussion	75
6	Steady fluid coiling	77
6.1	Introduction	77
6.2	Steady fluid coiling	80
6.2.1	Problem description	80
6.2.2	Boundary conditions	81
6.2.3	Numerical solution	82
6.3	Boundary-layer structure	84
6.3.1	Twisting motion in the tail	85
6.4	Inertia-dominated coiling for $Fr \gg \epsilon^{1/2}$	86
6.4.1	Stress and length scalings	86
6.4.2	Matching the bending stresses towards the tail	87
6.4.3	Estimates of the coiling speed and frequency	89
6.4.4	Stress exerted by the coil	91
6.5	Gravity-dominated coiling for $Fr \ll \epsilon \ln \epsilon$	93
6.5.1	Stress and length scalings	95
6.5.2	Matching the bending stress towards the tail	95
6.5.3	Pinning of thread at the nozzle	96
6.5.4	Asymptotic structure of the coil for $0 < \epsilon \ll 1$	97
6.5.5	Estimates of the coiling frequency and radius	101
6.6	Inertio-gravitational coiling for $Fr \sim \epsilon \ln \epsilon$	103
6.6.1	Stress and length scalings	104
6.6.2	Forcing of the tail by the coil away from resonance	104
6.7	Summary and discussion	105
7	Closing remarks	110
7.1	Summary of results	110
7.2	Future work	112
	Bibliography	113

CHAPTER 1

INTRODUCTION

The buckling of slender fluid threads and sheets is a phenomenon that arises in many situations. Everyday examples include the coiling of a thread of honey as it is poured onto a slice of toast, or of a thread of shower gel as it is poured onto one's hand. In industrial processes it is often desirable to inhibit fluid buckling, for example during filling processes where a buckled sheet of product entrains air or ambient fluid which can result in a lower quality of product (figure 1.1*a*; Tome & McKee, 1999; Yamamura *et al.*, 2000). Conversely, fluid buckling may be exploited, for example to assist the mass production of confectionery such as Vienetta ice cream (Unilever, 2006), or during the fabrication of foams and emulsions within microfluidic channels (figure 1.1*b*; Cubaud & Mason, 2009). Buckling phenomena also arise in geological processes, and can result in intricate rock formations (figure 1.1*c*; Buckmaster *et al.*, 1978; Guillou-Frottier *et al.*, 1995). A physical understanding of fluid buckling phenomena therefore has far-reaching applications.

This thesis addresses problems concerning the behaviour of a slender viscous thread as it falls through air and then buckles as it lands onto a rigid surface. It analyses the key force balances near the surface, and determines the way in which they govern the motion of the thread. There is particular attention paid to the physical effects of bending forces that are generated in the thread as it buckles.

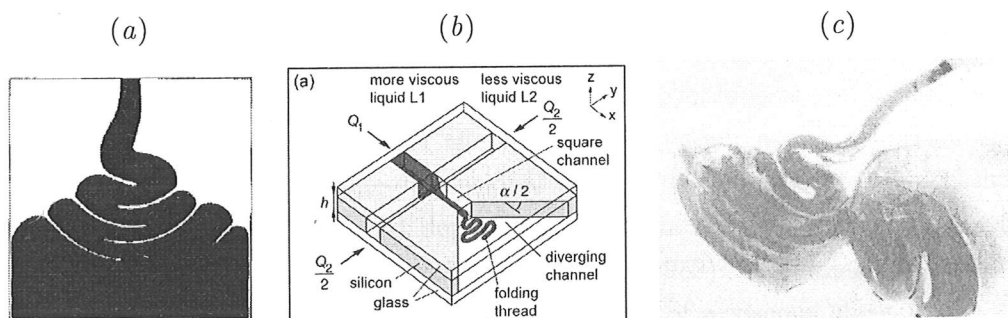


Figure 1.1: Examples of buckling phenomena. (a) Numerical simulation of the entrainment of air within folds of fluid during industrial filling processes (Tome & McKee, 1999). (b) Schematic diagram showing the folding of a fluid thread as it is extruded with another fluid through a microchannel (Cubaud & Mason, 2009). (c) Experimental model of tectonic plates that fold during subduction. Here, a sheet of corn syrup is extruded from a slot, and falls under gravity before reaching a density interface whereupon it buckles (Guillou-Frottier et al., 1995).

1.1 The deformation of slender viscous and elastic bodies under applied stresses and torques

The buckling phenomena analysed in this thesis are viscous deformations due to the stresses that arise when a viscous thread lands on a surface. The behaviour of a viscous material under an applied stress is analogous to that of an elastic material. The local deformation, or strain, of an elastic material depends linearly on the local stress that is applied. For a viscous material, it is instead the rate of strain that depends linearly on the applied stress. The majority of this thesis analyses a steadily moving viscous thread, and for problems of this type the role of the rate-of-strain tensor is closely analogous to that of the strain tensor in problems concerning static elastic deformations.

A slender, steadily moving viscous thread has three basic modes of deformation, which are analogous to those of elastic threads. It undergoes stretching or compression under an axial stress, twisting under an axial torque and bending when a torque is applied transverse to it. In the problems analysed here, a thread stretches under gravity before it lands onto a rigid surface, where it undergoes compression, bending and twisting. We briefly outline the progress made towards understanding the stretching and buckling of slender viscous bodies under applied loads.

1.1.1 Stretching under applied longitudinal stresses

The stretching of a thread of viscous fluid is commonly seen when pouring honey slowly from a bottle, or when allowing it to fall from a spoon. For such flows the weight of the thread causes a longitudinal stress to be applied to it. If the thread is slender, so that

its diameter is much smaller than its axial lengthscale, then the stress-free condition on the free surface of the thread implies that the velocity profile is approximately given by extensional flow, and at leading order the velocity is constant across a horizontal cross-section. This allows a simple one-dimensional theory to be derived for which the fluid velocity of a steadily falling thread depends only on the vertical distance beneath the extrusion point (Trouton, 1906; Matovich & Pearson, 1969). A similar one-dimensional model has also been derived to describe the stretching of a viscous sheet under gravity (Brown, 1960).

1.1.2 Bending and twisting under applied torques

While the theory for the bending of a slender elastic body under an applied torque is well established (Love, 1944; Timoshenko & Goodier, 1970), similar progress towards understanding the bending of a slender viscous body has been made only fairly recently. For example, experiments and numerical simulations have investigated the deflection of a horizontal viscous sheet or thread by gravity when it is steadily extruded from a slot (Munson, 1981). Similar work has analysed slumping liquid bridges (Tuck *et al.*, 1997; Teichman & Mahadevan, 2001; Hunt, 2002). In these situations, the torque that is necessary for bending to occur is due to the weight of the fluid, and to the support of the sheet at its ends.

The twisting of a viscous thread under an applied axial torque has not received as much attention. However, its effects are likely to be an important factor in recent experiments which investigate fluid thread coiling when the thread falls from a nozzle that is rotating about its axis (Ribe *et al.*, 2009).

1.2 The buckling instability of slender threads and sheets under compression

Early experiments showed that a viscous thread buckles and undergoes periodic coiling as it falls onto a rigid surface, provided the fall height is not too small (Barnes & Woodcock, 1958; Barnes & MacKenzie, 1959). Since there is no torque directly applied to the thread, the underlying cause of this buckling is not immediately obvious. An early theoretical advance was made by Taylor (1968), who floated very viscous threads of SAIB (a food additive) on a bed of mercury, and then placed them under axial compression by slowly moving the ends together. The resulting shapes made by the threads were observed to be similar to those made by elastic threads as they buckle under axial compression (Love,

1944). Taylor postulated that fluid buckling is an instability of the thread that is similar to the 'Euler' buckling instability exhibited by elastic beams when placed under sufficient axial compression. This observation was borne out by subsequent experiments which found that a falling fluid thread only undergoes coiling when the fall height is large enough to place the thread under sufficient axial compression near the contact point (Cruickshank & Munson, 1981; Griffiths & Turner, 1988). A subsequent calculation used a slender-thread model to confirm the hypothesis that the onset of buckling instability is a bifurcation from the steady-state stagnation-point flow as the fall height increases (Tchavdarov *et al.*, 1993).

1.2.1 Slender-sheet models

The problems analysed in this thesis involve balances between compression and bending forces in a viscous thread. These problems are closely analogous to similar problems that involve fluid sheets rather than threads. Hence an understanding of the buckling of viscous sheets is applicable to the buckling of viscous threads.

Early work to understand the buckling of fluid sheets was motivated by the geophysical observations of folds in rock formations, which result from the end compression of thin layers of rock within the Earth's crust (Buckmaster *et al.*, 1978). Subsequent experiments demonstrated that, for slow deformations, folding occurs with a characteristic wavelength that depends only on the physical properties and dimensions of the sheet, rather than on the nature of any small initial perturbations to the shape of the sheet (Blake & Bejan, 1984). This characteristic wavelength indicates that buckling is governed by a balance between the applied end compression and the forces that arise from the bending resistance of the sheet. The bending resistance of the sheet depends both on the properties of the fluid and on the thickness of the sheet.

More recently, theoretical models have been developed to apply to industrial situations such as the shaping of molten glass sheets, or paper milling. In these flows three-dimensional and inertial effects may be significant, and models have been developed that include these effects (Howell, 1996; Dyson, 2007). Ribe (2001) performed a thorough analysis of the force and velocity scales associated with stretching and with bending of thin viscous sheets, and determined the accuracy of different slender-sheet approximations in various physical contexts.

1.2.2 Periodic folding of viscous sheets

The periodic folding of a viscous sheet (Cruickshank & Munson, 1981; Cruickshank, 1988) is closely related to the steady coiling of a viscous thread, which is one of the problems analysed here. Both phenomena represent a buckling instability that is exhibited by a slender

viscous body when it is placed under longitudinal compression. The close correspondence between the two phenomena allowed the early progress made toward understanding viscous coiling to be applied to understand viscous sheet folding (Cruickshank & Munson, 1981; Cruickshank, 1988; Yarin & Tchavdarov, 1996).

If a slender fluid sheet buckles when it lands then its motion will settle to form regular periodic folds (Skorobogatiy & Mahadevan, 2000; Ribe, 2003). The folding frequency is determined by a balance that involves bending stress within the folds. If the fall height is small, then bending stress is dominant and folding is forced kinematically by the extrusion speed and the fall height. This regime is known as a 'viscous' regime, since it is dominated everywhere by the viscous bending stress in the sheet. If the fall height is moderately large, then the sheet is stretched by gravity before it lands on the surface, and the sheet buckles only at the bottom of the sheet. This regime is known as a 'gravitational' regime, since the bending stress at the bottom of the sheet is balanced by the local weight of the sheet. Within both viscous and gravitational regimes, the frequency scaling obtained agrees well with experiment and with numerical simulations (Skorobogatiy & Mahadevan, 2000; Ribe, 2003).

1.3 Outline of thesis

The aim of this thesis is to understand the dynamical effect of bending stress on a slender fluid thread. Two phenomena are examined that have recently been the subject of several theoretical and experimental investigations. One of these phenomena is the buckling of a slender fluid thread as it falls onto a moving belt, and the other is the steady coiling of a slender fluid thread as it falls onto a stationary surface. A slender-thread approximation has successfully been used to predict the behaviour of the thread in these contexts (Ribe, 2004; Ribe *et al.*, 2006*c*). While the theory yields accurate predictions of the thread behaviour, it encapsulates many dynamical effects, and obscures the key physical processes that govern the motion of the thread. Simpler models have previously been developed to understand the motion of slender threads (Chiu-Webster & Lister, 2006; Hlod *et al.*, 2007; Hlod, 2009; Gotz *et al.*, 2008; Marheineke & Wegener, 2009), but these omit the effects of bending stress. This omission is made with the justification that the resistance of a slender thread to bending is very small (Chiu-Webster & Lister, 2006, hereafter CWL). The analysis in this thesis demonstrates that while the bending resistance of a slender thread is indeed small, bending stress is nonetheless important within a boundary layer at the bottom of the thread. The inclusion of the effects of this boundary layer represents a significant improvement to previous models.

The analysis in the later chapters of this thesis is based on a slender-thread theory that is described in Chapter 2. Several preliminary problems are analysed in Chapter 3 that concern the behaviour of the stretching-dominated ‘tail’, in which bending stress is unimportant. The results obtained in this chapter are of direct relevance to the analysis in the subsequent chapters.

Chapters 4 and 5 concern the behaviour of a slender fluid thread as it falls onto, and is dragged by, a moving belt. The steady shapes made by the thread are analysed in Chapter 4, and the leading-order effects of bending stress are determined. Chapter 5 concerns the onset of transverse oscillations (hereafter referred to as ‘meanders’) that are observed as the belt speed is decreased. Asymptotic estimates are derived of the onset and frequency of meandering at onset, and it is shown that the tail plays an important dynamical role.

Chapter 6 concerns the steady coiling of a slender fluid thread as it falls onto a stationary surface. Particular attention is paid to the dynamical interactions between the bending stress at the bottom of the thread and the tail, and quantitative estimates of the coiling frequency are thereby derived. The main results of the thesis are summarised in chapter 7, and possible avenues for future research are discussed.

CHAPTER 2

THEORETICAL DESCRIPTION OF A SLENDER THREAD

The phenomena analysed in this thesis involve the behaviour of a slender viscous thread as it lands onto a rigid surface. These phenomena are three-dimensional free-boundary flows, which are traditionally very expensive to resolve numerically. While some progress has been made using direct methods such as front tracking (Tome & McKee, 1999), these methods offer little theoretical insight into the physical processes that govern the motion of the thread. It is therefore desirable to describe the motion of the thread using a simplified theory that includes all of the important dynamical processes in the thread.

If the thread is slender, then the problem may be simplified significantly using a slender-thread approximation (e.g. Entov & Yarin, 1984; Mahadevan *et al.*, 1998; Ribe, 2004, hereafter R04). The key assumption is that the radial lengthscale a^* of the thread is much smaller than its characteristic axial lengthscale s^* . If this assumption is valid, then the thread may be described by its curved axis. The axis is parametrised by the arclength s along it and has dynamical properties derived by taking averages over the cross-section of the thread. Treating the thread as a one-dimensional line rather than attempting to fully resolve the three-dimensional flow in the thread dramatically reduces the computational

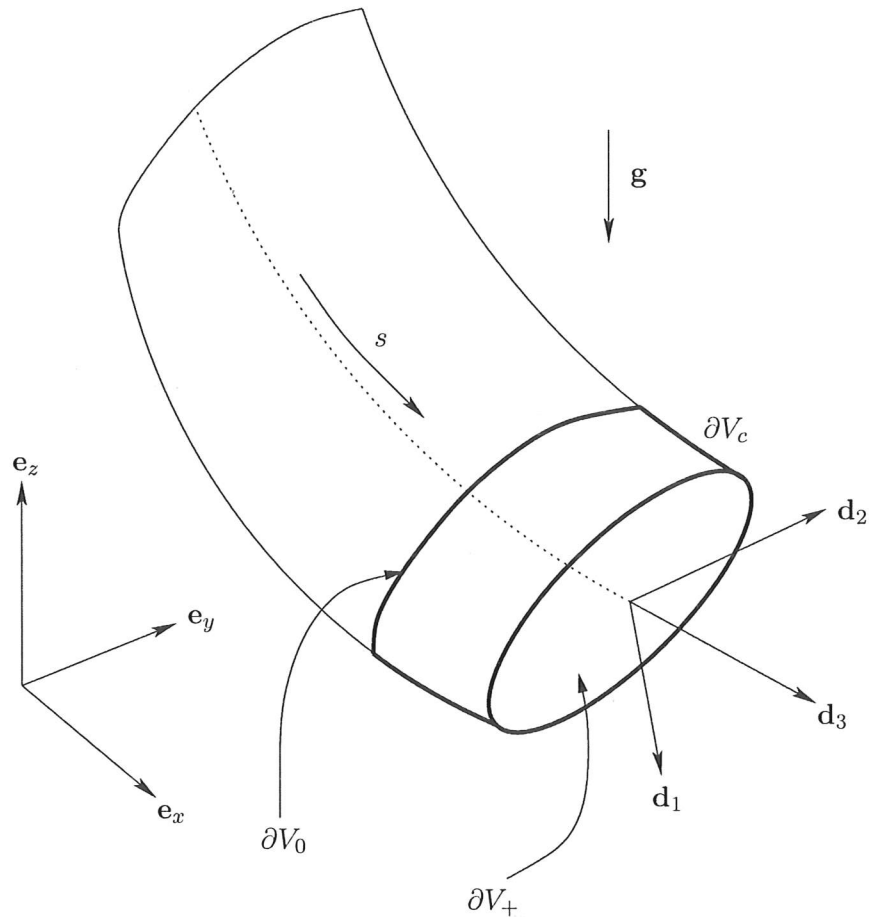


Figure 2.1: Diagram showing fixed and rotating coordinate axes, and the control volume considered in the force and torque balances. The control volume V is marked in bold, and is bounded by the cross-sections ∂V_0 and ∂V_+ , at arclengths s and $s + \delta s$ respectively. The coordinate axes \mathbf{e}_i are fixed in the laboratory frame and the Lagrangian basis vectors \mathbf{d}_i rotate with the thread.

cost. Nonetheless, the predictions obtained using a slender-thread approximation agree very closely with experiment (e.g. Entov & Yarin, 1984; Ribe *et al.*, 2006a;c).

In this chapter we describe the slender-thread theory that is used in subsequent chapters to examine and explain the key dynamical processes that govern the buckling of a slender thread. In the derivation that follows we describe the dominant balances that govern the behaviour of a slender thread, and use these to derive a system of equations to describe the motion of the thread.

2.1 Geometry of the centreline

We denote the position of the thread's centreline by $\mathbf{x}(s, t)$ and its radius by $a(s, t)$, where $\mathbf{x} = (x, y, z)$ with respect to a fixed Cartesian basis \mathbf{e}_i . We also define an orthonormal

basis $\mathbf{d}_i(s, t)$ aligned with the thread that thus varies along the centreline. We define \mathbf{d}_3 to be the tangent vector to the centreline, so that

$$\mathbf{d}_3 = \mathbf{x}', \quad (2.1.1)$$

where the prime denotes differentiation with respect to s . The vectors \mathbf{d}_1 and \mathbf{d}_2 that complete the basis are mutually perpendicular vectors that lie within the cross-section of the thread. The geometry of the fixed and rotating bases is shown in figure 2.1. The specific orientation of \mathbf{d}_1 and \mathbf{d}_2 within the cross-section is arbitrary, and may be selected for convenience. The curvature $\boldsymbol{\kappa}$ of the centreline is defined by the spatial variation of the basis vectors \mathbf{d}_i according to the Frenet relation

$$\mathbf{d}'_i = \boldsymbol{\kappa} \times \mathbf{d}_i. \quad (2.1.2)$$

Since \mathbf{d}_3 is defined to be tangential to the centreline of the thread, the curvature components $\kappa_1 = \boldsymbol{\kappa} \cdot \mathbf{d}_1$ and $\kappa_2 = \boldsymbol{\kappa} \cdot \mathbf{d}_2$ are determined by the shape of the centreline. However, since the orientation of \mathbf{d}_1 and \mathbf{d}_2 is arbitrary, so too is their variation with s . The twist rate κ_3 of the basis about \mathbf{d}_3 may therefore also be selected for convenience.

The slender-thread model of Entov & Yarin (1984) defines κ_3 by the torsion of the centreline, so that \mathbf{d}_1 and \mathbf{d}_2 may be defined by the principal normal and the binormal to the centreline. However, in the problems we will consider, there are regions of the thread that are almost straight. In these regions the direction of the principal normal can change rapidly, and hence the resulting system of equations would be numerically unstable. This difficulty is resolved by instead defining the basis \mathbf{d}_i by material vectors that rotate with the thread as it flows (e.g R04; Ribe *et al.*, 2006c, hereafter R06c), as we discuss further in §2.2.

2.2 Velocity and angular velocity in the thread

We now consider the fluid velocity $\mathbf{u}(\mathbf{x}, t)$ in the thread. We assume that the cross-section of the thread is circular everywhere. Under this assumption, the average fluid velocity of a cross-section is

$$\mathbf{U}(s, t) = \frac{1}{\pi a^2} \int \mathbf{u} dA. \quad (2.2.1)$$

Any linear variation of \mathbf{u} across the cross-section would result in no difference between \mathbf{U} and the velocity \mathbf{u} on the centreline. Any difference between \mathbf{U} and \mathbf{u} is therefore due only to quadratic and higher-order variations of \mathbf{u} . As we will see in §2.3.1, where we expand the velocity profile within the cross-section to second order in the thread radius,

this difference is $O(\mathbf{U}a^{*2}/s^{*2})$ (or smaller) and negligible in the asymptotic limit of a very slender thread. We may therefore use $\mathbf{u}(\mathbf{x}, t)$ and $\mathbf{U}(s, t)$ interchangeably.

There is a third velocity field, defined only on the centreline by $D\mathbf{x}/Dt$, where

$$\frac{D}{Dt} = \left(\frac{\partial}{\partial t} \right)_s - \left(\frac{\partial \mathbf{x}}{\partial t} \right)_s \cdot \mathbf{d}_3 \frac{\partial}{\partial s} + U_3 \frac{\partial}{\partial s} \quad (2.2.2)$$

is the rate of change measured by an observer moving tangentially to the centreline with speed $U_3 - (\partial \mathbf{x} / \partial t)_s \cdot \mathbf{d}_3$ relative to points with fixed values of s , where $U_3 = \mathbf{U} \cdot \mathbf{d}_3$ is the average axial velocity component of fluid at \mathbf{x} . The third term in (2.2.2) is the advective rate of change due to the axial velocity component in the lab frame, and the second term is a correction term that accounts for the motion of the arclength coordinate along \mathbf{d}_3 due to distributed stretching of the thread. This correction term is relevant only for time-dependent problems, and therefore arises only in chapter 5. However, the problem analysed there is a linear perturbation about the steady state which induces no extra stretching, and thus this correction term does not appear in the linear problem. We therefore assume henceforth that the material derivative is given simply by

$$\frac{D}{Dt} = \frac{\partial}{\partial t} + U_3 \frac{\partial}{\partial s}. \quad (2.2.3)$$

The material velocity $D\mathbf{x}/Dt$ of the centreline, defined above, is not necessarily equal to the true fluid velocity $\mathbf{u}(\mathbf{x}, t)$ on the centreline, in part because \mathbf{x} is the average position over a cross-section and in part because the fluid particles that comprise a cross-section change with time. However, it can again be shown (Ribe, 2002) that if the thread is slender, then the difference between these two velocities is only $O(\mathbf{U}a^{*2}/s^{*2})$ and therefore negligible. We may therefore approximate the centreline velocity by

$$\mathbf{u}(\mathbf{x}, t) = \mathbf{U}(s, t) = \frac{D\mathbf{x}}{Dt} = \frac{\partial \mathbf{x}}{\partial t} + U_3 \mathbf{d}_3. \quad (2.2.4)$$

The contribution $\partial \mathbf{x} / \partial t$ represents the time-dependent motion of the centreline normal to the thread and $U_3 \mathbf{d}_3$ represents advection along the thread due to the axial velocity component.

We now consider the local velocity variation in the thread. We make a linear expansion of the velocity \mathbf{u} about a point $\mathbf{x}(s, t)$ on the centreline,

$$\mathbf{u}(\mathbf{x} + \delta \mathbf{x}) = \mathbf{U}(s) + \mathbf{\Delta}(s) \cdot \delta \mathbf{x} + \boldsymbol{\omega}(s) \times \delta \mathbf{x}, \quad (2.2.5)$$

where the tensor $\mathbf{\Delta}$ is the strain rate and the vector $\boldsymbol{\omega}$ is the angular velocity of the fluid at the centreline position \mathbf{x} . Substitution of (2.2.5) into the incompressibility condition $\nabla \cdot \mathbf{u} = 0$ implies that $\mathbf{\Delta}$ is trace free.

An expansion for the variation of the centreline velocity along the thread can be derived by substituting $\delta \mathbf{x} = \delta s \mathbf{d}_3$ into (2.2.5) to obtain

$$\mathbf{U}' = \Delta \cdot \mathbf{d}_3 + \boldsymbol{\omega} \times \mathbf{d}_3. \quad (2.2.6)$$

The local angular velocity $\boldsymbol{\omega}$ is linked kinematically to the shape and to the velocity of the centreline. To see this, we use the Frenet relation (2.1.2) to expand $\mathbf{U}' = U'_i \mathbf{d}_i + U_i \boldsymbol{\kappa} \times \mathbf{d}_i$ in (2.2.6), and then project onto \mathbf{d}_1 and \mathbf{d}_2 . Omitting for the moment the components Δ_{13} and Δ_{23} of the strain tensor, which are shown in §2.3 to be zero at leading order, the angular velocity components ω_1 and ω_2 are given by

$$\omega_1 = -U'_2 - \kappa_3 U_1 + \kappa_1 U_3 \quad (2.2.7a)$$

$$\omega_2 = U'_1 - \kappa_3 U_2 + \kappa_2 U_3. \quad (2.2.7b)$$

The kinematic evolution of \mathbf{d}_3 along the thread can be derived by differentiating (2.2.4) with respect to s to obtain

$$\mathbf{U}' = \frac{\partial}{\partial s} \frac{D\mathbf{x}}{Dt} = \frac{D\mathbf{d}_3}{Dt} + U'_3 \mathbf{d}_3. \quad (2.2.8)$$

Then by substituting $\mathbf{U}' = U'_i \mathbf{d}_i + U_i \boldsymbol{\kappa} \times \mathbf{d}_i$ and projecting onto \mathbf{d}_3 , we obtain

$$\frac{D\mathbf{d}_3}{Dt} = (U'_2 + \kappa_3 U_1 - \kappa_1 U_3) \mathbf{d}_2 + (U'_1 + \kappa_2 U_3 - \kappa_3 U_2) \mathbf{d}_1. \quad (2.2.9)$$

Substitution of (2.2.7) then yields

$$\frac{D\mathbf{d}_3}{Dt} = \omega_1 \mathbf{d}_2 - \omega_2 \mathbf{d}_1. \quad (2.2.10)$$

As noted in §2.1, it is usually convenient to relate the variation of the basis vectors \mathbf{d}_1 and \mathbf{d}_2 along the thread such that they rotate with the local angular velocity of the thread. It is sometimes convenient also to add an offset $\omega_0 \mathbf{d}_3$ to the rotation rate, which exploits the arbitrary choice of twisting rate of \mathbf{d}_1 and \mathbf{d}_2 about \mathbf{d}_3 . With this definition, (2.2.10) may be generalised so that it also describes the variation of \mathbf{d}_1 and \mathbf{d}_2 along the thread, according to

$$\frac{D\mathbf{d}_i}{Dt} = (\boldsymbol{\omega} + \omega_0 \mathbf{d}_3) \times \mathbf{d}_i. \quad (2.2.11)$$

By following a similar process as was used to derive (2.2.7), the projection of (2.2.6) onto \mathbf{d}_3 yields

$$\Delta_{33} = U'_3 - \kappa_2 U_1 + \kappa_1 U_2. \quad (2.2.12)$$

The other components of Δ are determined by stress boundary conditions imposed on the free surface of the thread, and we discuss these in §2.3.

If the thread motion is steady, then $U_1 = U_2 = 0$. In the time-dependent perturbation analysis performed in chapter 5, the terms $\kappa_2 U_1$ and $\kappa_1 U_2$ in (2.2.12) are higher-order perturbations to the steady state. From now on, we therefore identify

$$\Delta_{33} = U_3', \quad (2.2.13)$$

and we denote the axial velocity component U_3 by U .

2.3 Stress and stress-moments in the thread

The motion of the thread depends on the physical properties of the fluid through its dynamic viscosity μ , its density ρ and the surface-tension coefficient γ of the free surface. The equations that govern the motion of the thread are derived by considering force and torque balances on an infinitesimal slice of the thread. We define a control volume V as depicted in figure 2.1, so that it is bounded by circular cross-sections ∂V_0 and ∂V_+ at arclengths s and $s + \delta s$ and by the curved surface ∂V_C . The surface ∂V_C is bounded by the two circular lines C_0 and C_+ . The resultant force and torque that act on a cross section are given by

$$\mathbf{N} = \int \boldsymbol{\sigma} \cdot \mathbf{d}_3 dA \quad \text{and} \quad \mathbf{M} = \int \mathbf{y} \times \boldsymbol{\sigma} \cdot \mathbf{d}_3 dA, \quad (2.3.1a,b)$$

where $\boldsymbol{\sigma}$ is the local stress tensor of the flow and \mathbf{y} is the displacement from the centreline within the cross-section. Although \mathbf{N} and \mathbf{M} are a force and torque respectively, we use the terminology of beam theory (e.g. Timoshenko & Goodier, 1970) and refer to them as the (resultant) stress and the (resultant) stress moment. We first determine the constitutive relations that link variations in the velocity or the angular velocity of the thread to the resultant axial stress N_3 or resultant stress moment \mathbf{M} exerted on a cross-section. We then consider force and torque balances on V to show how the variation of \mathbf{N} and \mathbf{M} along the centreline of the thread determines the motion of the thread.

2.3.1 Constitutive relations

For simplicity, we treat stretching and bending motions separately in the derivations that follow. There are small effects that arise from the coupling of stretching and bending motions through the curvature of the centreline, but these are negligible for a slender thread. Further discussion is given in §2.4.

Stretching

We begin with the linear velocity expansion (2.2.5). The stress tensor

$$\boldsymbol{\sigma} = -p\mathbf{I} + \mu(\nabla\mathbf{u} + \nabla\mathbf{u}^T) \quad (2.3.2)$$

of this velocity profile is clearly given by

$$\boldsymbol{\sigma} = -p\mathbf{I} + 2\mu\boldsymbol{\Delta}. \quad (2.3.3)$$

The dynamic boundary condition on the free surface of the thread is

$$\boldsymbol{\sigma} \cdot \mathbf{y} = -\frac{\gamma}{a}\mathbf{y} \quad \text{at } |\mathbf{y}| = a. \quad (2.3.4)$$

Since this boundary condition holds independently of the orientation of \mathbf{y} within the cross-section, the local stress tensor $\boldsymbol{\sigma}$, and therefore also $\boldsymbol{\Delta}$, are diagonal to leading order. Further, the strain-rate components Δ_{11} and Δ_{22} in the cross-section are equal. Incompressibility implies that $\Delta_{11} + \Delta_{22} = -\Delta_{33}$, and hence (2.2.13) implies that $\Delta_{11} = \Delta_{22} = -U'/2$. Substituting this result into (2.3.3) and the stress condition (2.3.4) gives the leading-order pressure distribution $p = -\mu U' + \gamma/a$ in the cross-section. The axial component of the stress tensor is obtained by substituting (2.2.13) and p into (2.3.3), which gives

$$\sigma_{33} = 3\mu U' - \frac{\gamma}{a}. \quad (2.3.5)$$

Finally, the resultant axial stress is found by substituting (2.3.5) into (2.3.1a), which gives

$$N_3 = 3\mu\pi a^2 U' - \pi\gamma a. \quad (2.3.6)$$

Bending

The leading-order stress vector $\boldsymbol{\sigma} \cdot \mathbf{d}_3 = \sigma_{33}\mathbf{d}_3$ is constant across the cross-section and hence substitution into (2.3.1b) gives no resultant stress moment \mathbf{M} at this order. To determine the resultant stress moment acting on a cross-section, it is necessary to expand the velocity profile (2.2.5) within the cross-section to second order in \mathbf{y} .

Consider a thread whose cross-sectional velocity profile is

$$\mathbf{u} = \mathbf{U} + \boldsymbol{\omega} \times \mathbf{y} + H_1(y_1, y_2)\mathbf{d}_1 + H_2(y_1, y_2)\mathbf{d}_2 + O(y^3), \quad (2.3.7)$$

where H_1 and H_2 are quadratic functions of y_1 and y_2 . Then expansion of the incompressibility condition to $O(y)$ implies that in the absence of stretching,

$$(\boldsymbol{\omega}' \times \mathbf{y}) \cdot \mathbf{d}_3 + \frac{\partial H_1}{\partial y_1} + \frac{\partial H_2}{\partial y_2} = 0. \quad (2.3.8)$$

Hence

$$\frac{\partial H_1}{\partial y_1} + \frac{\partial H_2}{\partial y_2} = (\boldsymbol{\omega}' \cdot \mathbf{d}_2)y_1 - (\boldsymbol{\omega}' \cdot \mathbf{d}_1)y_2 + O(y^2). \quad (2.3.9a)$$

Since \mathbf{U} is defined as the average velocity, (2.3.7) gives

$$\int_{|y| \leq a} H_1 dy_1 dy_2 = \int_{|y| \leq a} H_2 dy_1 dy_2 = 0. \quad (2.3.9b)$$

The tangential stress condition on the free surface of the thread is

$$\sigma_{12} = \sigma_{21} = \mu \left(\frac{\partial H_1}{\partial y_2} + \frac{\partial H_2}{\partial y_1} \right) = O(y^2) \quad \text{on } |y| = a. \quad (2.3.9c)$$

The quadratic functions that satisfy the conditions (2.3.9) are

$$H_1 = \frac{1}{4} \boldsymbol{\omega}' \cdot [(y_1^2 - y_2^2) \mathbf{d}_2 - 2y_1 y_2 \mathbf{d}_1] \quad \text{and} \quad H_2 = \frac{1}{4} \boldsymbol{\omega}' \cdot [(y_1^2 - y_2^2) \mathbf{d}_1 + 2y_1 y_2 \mathbf{d}_2] \quad (2.3.10)$$

The normal-stress boundary condition on the free surface $|y| = a$ is given by

$$\mathbf{n} \cdot \boldsymbol{\sigma} \cdot \mathbf{n} = \frac{1}{a^2} (y_1^2 \sigma_{11} + y_2^2 \sigma_{22}) = -\frac{\gamma}{a}. \quad (2.3.11)$$

From (2.3.7) and (2.3.10), the stress components σ_{11} and σ_{22} are

$$\sigma_{11} = \sigma_{22} = -p + \mu(\boldsymbol{\omega}' \cdot \mathbf{d}_1)y_2 - \mu(\boldsymbol{\omega}' \cdot \mathbf{d}_2)y_1. \quad (2.3.12)$$

Since $y_1^2 + y_2^2 = a^2$ and $\sigma_{11} = \sigma_{22}$ on $|y| = a$, the pressure varies linearly across the cross-section as

$$p = \mu(\boldsymbol{\omega}' \cdot \mathbf{d}_1)y_2 - \mu(\boldsymbol{\omega}' \cdot \mathbf{d}_2)y_1 + \frac{\gamma}{a}. \quad (2.3.13)$$

We now compute the leading-order stress moment acting on the cross-section. The components of $\boldsymbol{\sigma} \cdot \mathbf{d}_3$ vary linearly across the cross-section as

$$\sigma_{31} = -\mu(\boldsymbol{\omega}' \cdot \mathbf{d}_3)y_2 \quad (2.3.14a)$$

$$\sigma_{32} = \mu(\boldsymbol{\omega}' \cdot \mathbf{d}_3)y_1 \quad (2.3.14b)$$

$$\sigma_{33} = -\frac{\gamma}{a} + 3\mu(\boldsymbol{\omega}' \cdot \mathbf{d}_2)y_1 - 3\mu(\boldsymbol{\omega}' \cdot \mathbf{d}_1)y_2. \quad (2.3.14c)$$

Substitution of (2.3.14) into the definition (2.3.1b) of the stress moment \mathbf{M} yields

$$M_1 = \frac{3\mu\pi a^4}{4} \boldsymbol{\omega}' \cdot \mathbf{d}_1 \quad (2.3.15a)$$

$$M_2 = \frac{3\mu\pi a^4}{4} \boldsymbol{\omega}' \cdot \mathbf{d}_2 \quad (2.3.15b)$$

$$M_3 = \frac{\mu\pi a^4}{2} \boldsymbol{\omega}' \cdot \mathbf{d}_3 \quad (2.3.15c)$$

We note that the equations for M_1 and M_2 , which represent the stress moment associated with bending motion, differ from that for M_3 , which represents the torque associated with twisting motion.

2.3.2 Stress balance

The stress balance on an infinitesimal slice V is obtained by means of the momentum-integral equation. In the chapters that follow, we include inertial terms only in the quasi-steady problems of a vertically falling thread in chapter 3, and of a steadily coiling thread in §6.4. The term $\int_V \rho \mathbf{u} \cdot \partial \mathbf{u} / \partial t$ is important only in the coiling problem in the laboratory frame, and its leading-order contribution in the frame rotating with the coil is through the centrifugal and Coriolis accelerations of the entire slice V which appear in the obvious way. For simplicity, we do not include such effects in the following description (though they are in the later calculations), and include only the inertial terms that represent advection. In the absence of explicit time-dependence, the momentum-integral equation is

$$\int_{\partial V} \rho \mathbf{u} (\mathbf{u} \cdot \mathbf{n}) dA = \int_V \rho \mathbf{g} dV + \int_{\partial V} \boldsymbol{\sigma} \cdot \mathbf{n} dA. \quad (2.3.16)$$

The final term comprises contributions from the viscous stresses that act on the cross-sections ∂V_0 and ∂V_+ , and from surface tension forces acting on ∂V_C . It is therefore given by

$$\begin{aligned} \int_{\partial V} \boldsymbol{\sigma} \cdot \mathbf{n} dA &= \int_{\partial V_{0,+}} \boldsymbol{\sigma} \cdot \mathbf{n} dA + \int_{\partial V_C} \gamma (\nabla \cdot \mathbf{n}) \mathbf{n} dA \\ &= \mathbf{N}(s + \delta s) - \mathbf{N}(s) + \int_{C_{0,+}} \gamma \mathbf{t} dl \\ &= \mathbf{N}(s + \delta s) - \mathbf{N}(s) + 2\pi\gamma \{a\mathbf{d}_3(s + \delta s) - a\mathbf{d}_3(s)\}, \end{aligned} \quad (2.3.17)$$

where we have made the leading-order approximation that the tangent vector \mathbf{t} on the free surface is equal to \mathbf{d}_3 .

The remaining integrals in (2.3.16) may readily be evaluated and combined with (2.3.17) to obtain

$$[\rho\pi a^2 U \mathbf{U}]_0^+ = \rho\pi a^2 \mathbf{g} \delta s + [\mathbf{N} + 2\pi\gamma a \mathbf{d}_3]_0^+, \quad (2.3.18)$$

where we have introduced the notation $[X]_0^\dagger = X(s + \delta s) - X(s)$. We divide through by δs to obtain

$$\rho\pi a^2 U \mathbf{U}' = \rho\pi a^2 \mathbf{g} + \mathbf{N}' + 2\pi\gamma(a\mathbf{d}_3)'. \quad (2.3.19)$$

The time-dependent motion of a slender thread is analysed only in chapter 5, where we omit the effects of inertia and surface tension. When the thread is steady, $\mathbf{U} = U\mathbf{d}_3$ and a^2U is constant, and we may rearrange (2.3.19) to obtain

$$\mathbf{N}' = \{(\rho\pi a^2 U^2 - 2\pi\gamma a)\mathbf{d}_3\}' - \rho\pi a^2 \mathbf{g}, \quad (2.3.20)$$

We note that (2.3.20) suggests the definition of an 'effective stress' by

$$\check{\mathbf{N}} = \mathbf{N} + (2\pi\gamma a - \rho\pi a^2 U^2)\mathbf{d}_3, \quad (2.3.21)$$

so that in the steady flow the constitutive equation (2.3.6) and force balance (2.3.20) may be re-expressed as

$$\check{N}_3 = 3\mu\pi a^2 U' + \pi\gamma a - \rho\pi a^2 U^2 \quad (2.3.22)$$

$$\check{\mathbf{N}}' = \rho\pi a^2 g\mathbf{e}_z, \quad (2.3.23)$$

with $\mathbf{g} = -g\mathbf{e}_z$.

2.3.3 Stress-moment balance

The stress-moment balance on an infinitesimal slice V is obtained by means of the angular-momentum integral equation, which again in the absence of explicit time-dependence is

$$\int_{\partial V} \rho \mathbf{y}^\dagger \times \mathbf{u}(\mathbf{u} \cdot \mathbf{n}) dA = \int_V \rho \mathbf{y}^\dagger \times \mathbf{g} dV + \int_{\partial V} \mathbf{y}^\dagger \times \boldsymbol{\sigma} \cdot \mathbf{n} dA, \quad (2.3.24)$$

where \mathbf{y}^\dagger is the displacement from the centreline position $\mathbf{x}(s)$. On the surface ∂V_0 , \mathbf{y}^\dagger is simply the displacement \mathbf{y} within the cross-section. On the surface ∂V_+ , \mathbf{y}^\dagger has a contribution $\delta s \mathbf{d}_3$ from the distance δs along the centreline in addition to the displacement $\mathbf{y}(s + \delta s)$ within the cross-section ∂V_+ .

The dominant contributions to (2.3.24) are from the torque exerted by the viscous stress on ∂V_0 and ∂V_+ , and we briefly describe the other (smaller) contributions. The stress on ∂V_C is due only to surface tension, and the resultant torque is non-zero only when the thread is both curved and of non-uniform radius. The term on the left-hand side of (2.3.24) is the small torque generated when momentum flux is diverted through a curved thread. The first term on the right-hand side of (2.3.24) is the resultant torque on a curved thread

that is due to the extra weight of fluid on the outside of a bend in the thread. We group these small contributions to (2.3.24) by defining the stress-moment vector \mathcal{M} to be

$$\mathcal{M}\delta s = \int_V \rho \mathbf{y}^\dagger \times \mathbf{g} dV + \int_{\partial V_C} \mathbf{y}^\dagger \times \boldsymbol{\sigma} \cdot \mathbf{n} dA - \int_{\partial V} \rho \mathbf{y}^\dagger \times \mathbf{u}(\mathbf{u} \cdot \mathbf{n}) dA. \quad (2.3.25)$$

Substitution of (2.3.25) into (2.3.24) yields

$$\int_{\partial V_{0,+}} \mathbf{y}^\dagger \times \boldsymbol{\sigma} \cdot \mathbf{n} dA + \mathcal{M} \delta s = \mathbf{0}, \quad (2.3.26)$$

from which it follows that

$$\delta s \mathbf{d}_3 \times \mathbf{N}(s + \delta s) + \mathbf{M}(s + \delta s) - \mathbf{M}(s) + \mathcal{M} \delta s = \mathbf{0}. \quad (2.3.27)$$

The stress-moment balance on an infinitesimal slice is therefore

$$\mathbf{M}' = \mathbf{d}_3 \times \mathbf{N} + \mathcal{M}. \quad (2.3.28)$$

The contributions to \mathcal{M} have been derived by Ribe *et al.* (2006a), and can be shown to have a dynamical effect that is an $O(a^{*2}/s^{*2})$ factor smaller than the corresponding contributions to $\mathbf{d}_3 \times \mathbf{N}$. For simplicity, we do not present them here. However, we do include them in the numerical calculations in chapters 4 and 6 when comparing asymptotic estimates for the motion of a steadily dragged thread and a steadily coiling thread.

2.4 Discussion

Equations (2.1.1), (2.1.2), (2.2.11), (2.3.15), (2.3.22), (2.3.23) and (2.3.28) form a complete system of ODEs that describes the motion of a slender thread. It is also necessary to impose boundary conditions to close the problem and fully determine the motion of the thread, and these are discussed separately for the problems analysed in chapters 4–6. Once the boundary conditions are known, the theory described in this chapter allows the behaviour of the thread to be predicted through solution of a two-point boundary-value problem. There are many methods available to solve such problems; we use a continuation method which we describe in more detail in the relevant chapters. Such an approach is advantageous as it allows the effects of varying experimental parameters, such as the fall height, to be readily determined.

The theory described in §2.3.1 has neglected terms that represent the coupling of bending and stretching motion through the curvature of the thread. The neglect of such terms

can also be shown to introduce only an $O(a^{*2}/s^{*2})$ error (Ribe, 2002). In chapters 4–6 such errors are asymptotically negligible compared to the leading-order effects of bending stresses in the thread, and so we do not pursue this coupling further.

We have assumed throughout that the cross-section of the thread is circular, as motivated by recent experiments in which a fluid thread is extruded from a circular nozzle. The work of Dewynne *et al.* (1994) analysed the extensional flow of threads with non-circular cross-section that are almost straight, and showed that at leading order in a^*/s^* , the shape of the cross-section is simply rescaled. Hence the assumption that the cross-section of the thread remains circular after extrusion from the nozzle is justified provided the thread is sufficiently slender.

CHAPTER 3

THE FALL OF A VISCOUS THREAD

We aim to analyse the buckling of a slender viscous thread as it lands onto a surface. In the problems we analyse in the later chapters, a thread is extruded from a nozzle and stretched by gravity before it lands, and bending occurs only near the bottom of the thread. The bending stress in the thread is implied by (2.3.15) to scale with its radius like a^4 . To use this scaling at the bottom of the thread, it is therefore necessary to determine the extent to which the thread is thinned by gravity before it lands. Before analysing this process, we comment on a few simplifications that can be made in the present context.

The slender-thread model derived in chapter 2 has implicitly assumed that, in the absence of bending, the axial velocity of the thread is constant across a cross-section. However, within the nozzle the no-slip condition on the inner walls results in a Poiseuille flow profile. Hence there must be a region near the exit from the nozzle where the velocity profile changes from Poiseuille flow to extensional flow. While this means that the assumption of extensional flow breaks down near the nozzle, the axial lengthscale of this region has been shown to be comparable to the diameter of the nozzle (Goren & Wronski, 1966; Batchelor *et al.*, 1973) and hence very much less than the height of fall. The $O(a^*/s^*)$ error introduced by neglecting this region is asymptotically negligible compared

to the leading-order effects of bending forces analysed in the later chapters, and we do not pursue it further.

The extension of a fluid thread arises in several industrial contexts, some of which introduce effects that complicate the theory derived in chapter 2. For example, during the heating and pulling of glass fibres, the viscosity of the fibre depends on temperature, and therefore varies significantly as the fibre is pulled (Huang *et al.*, 2003). The physical properties of the thread may also vary across the cross-section, for instance during the drawing of hollow or ‘holey’ glass fibres (Fitt *et al.*, 2001; Griffiths & Howell, 2008). However, we focus here on recent laboratory experiments (e.g. CWL; Maleki *et al.*, 2006; Morris *et al.*, 2007) in which the thread has a constant viscosity and circular cross-section, and the complications do not arise.

Under certain circumstances, an extruded fluid thread undergoes some sort of break-up instability before landing. If the extrusion speed is sufficiently slow that inertia is negligible, and the fall height is sufficiently large, then the drop stretches under its own weight until it breaks. This gravity-driven break-up of the thread gives rise to a periodic dripping motion (Wilson, 1988). Break-up can also be driven by surface tension in a wide range of regimes and has been observed, for example, both when inertia is dominant and when inertia is negligible (see review by Eggers, 1997). However, specific criteria for the length over which surface-tension-driven breakup might occur are not well understood. Another type of break-up instability occurs when the extrusion speed is very large, and the air drag on the thread causes it to undergo a buckling instability which can then lead to breakup. This effect was analysed using an early slender-thread model (Entov & Yarin, 1984). Although break-up can thus occur in a variety of situations, a vertically falling viscous thread has also been observed to be stable to break-up for very large fall heights (e.g. Senchenko & Bohr, 2005). In particular, for the experiments we analyse in chapters 4–6, no break-up is observed, and hence we do not consider such instabilities further.

The analysis in this chapter begins in §3.1 by considering the fall of an infinite thread under gravity. Scalings for the velocity, stress and stress moment are thereby obtained in §3.2 that describe the thread at a height H beneath the nozzle, and these scalings are used to nondimensionalise the system of equations derived in chapter 2. Several preliminary problems concerning a vertical or near vertical thread without bending stress are then analysed in §§3.3–3.6 that are of direct relevance to the analysis in later chapters.

3.1 Steady vertical fall of an infinitely long viscous thread

We begin by analysing the steady fall of an infinitely long vertical thread. This is a simpler problem than the fall of a thread through a finite height, and the results derived in this section will be used to estimate the velocity scales at a height H beneath the nozzle. We will see in later chapters that these scalings relate to the behaviour of a thread as it lands on a surface.

The vertical fall of a viscous thread under gravity is governed by extensional flow. The governing equations for steady fall may be obtained by substituting $\mathbf{e}_z = -\mathbf{d}_3$ and (2.3.22) into (2.3.23) and using $a^2 = Q/\pi U$ to obtain

$$\left(\frac{3\mu U'}{U} + \gamma\sqrt{\frac{\pi}{QU}} - \rho U\right)' + \frac{\rho g}{U} = 0. \quad (3.1.1)$$

The first boundary condition imposes the extrusion speed at the nozzle,

$$U = U_N \quad \text{at} \quad s = s_N, \quad (3.1.2a)$$

where s_N is the arclength position of the nozzle. The second boundary condition is imposed under the assumption that the thread falls under its own weight, so that there is no tension applied to the thread far beneath the nozzle. Hence

$$3\mu U'/U \rightarrow 0 \quad \text{as} \quad s \rightarrow \infty. \quad (3.1.2b)$$

Despite the simplifications made to the problem so far, the governing equation (3.1.1) is still a nonlinear ODE that can only be solved analytically if some of the terms are absent. We now describe some of these simplified problems.

3.1.1 Gravity-viscosity balance

In the absence of both inertia and surface tension, equation (3.1.1) for the fall speed simplifies to

$$\left(\frac{3\mu U'}{U}\right)' + \frac{\rho g}{U} = 0. \quad (3.1.3)$$

The solution that satisfies (3.1.2) is

$$U = \frac{\rho g}{6\mu}(s - d)^2, \quad (3.1.4)$$

where d is a constant that is chosen to satisfy (3.1.2a).

Rather fortuitously, the quadratic form of the solution (3.1.4) is unaffected by surface tension with inertia still negligible. It is easily shown (e.g. CWL; Senchenko & Bohr, 2005) that a fall speed $U = K^2(s - d)^2$ satisfies (3.1.1) provided inertia is negligible and K satisfies

$$6\mu K^2 + \gamma \sqrt{\frac{\pi}{Q}} K - \rho g = 0. \quad (3.1.5)$$

We note that if $\gamma = 0$ then $K^2 = \rho g / 6\mu$ which recovers (3.1.4). The boundary condition (3.1.2a) is readily satisfied by setting

$$d = s_N - \sqrt{U_N} / K. \quad (3.1.6)$$

In most of this thesis we consider a thread falling through a finite height, and the boundary condition at the bottom of the thread means that the fall speed no longer has the quadratic form (3.1.4). It is then no longer possible to obtain a closed-form solution for U with γ non-zero. For simplicity, we will typically omit the effects of surface tension for the remainder of this thesis, but they may readily be included in numerical calculations. Unless stated otherwise, the fall of the thread is henceforth assumed to be governed by

$$\left(\frac{3\mu U'}{U} - \rho U \right)' + \frac{\rho g}{U} = 0. \quad (3.1.7)$$

3.1.2 The relevance of inertia

We have so far omitted inertial effects. Substitution of (3.1.4) into (3.1.7) shows that this omission is justified provided

$$s - d \ll \left(\frac{\mu^2}{\rho^2 g} \right)^{1/3}. \quad (3.1.8)$$

While this assumption typically holds near the nozzle, it breaks down after the thread falls through a height given by the right-hand-side of (3.1.8). As the thread falls, inertial effects play a more important role in the thread, until they dominate viscous effects and the thread falls under an inertia-gravity balance. Under such a balance, (3.1.7) becomes

$$\rho U' = \frac{\rho g}{U}, \quad (3.1.9)$$

which has the solution

$$U \sim \sqrt{2g(s - d^*)}, \quad (3.1.10)$$

a form familiar from elementary mechanics. Here d^* is a constant that corresponds to a change in the effective origin due to the viscous-dominated region near the nozzle.

To analyse the transition between the viscous-dominated and inertia-dominated regions, we consider the scalings of the terms in (3.1.7). Viscous, gravitational and inertial forces are all in balance when

$$\frac{\mu}{s^2} \sim \frac{\rho U}{s} \sim \frac{\rho g}{U}, \quad (3.1.11)$$

which implies that the fall speed and distance beneath the nozzle scale like

$$U \sim \left(\frac{g\mu}{\rho}\right)^{1/3} \quad \text{and} \quad s \sim \left(\frac{\mu^2}{\rho^2 g}\right)^{1/3}. \quad (3.1.12)$$

A closed-form solution to (3.1.7) with both inertia and viscosity has been derived (Clarke, 1966; 1968). The general solution is

$$U = \left(\frac{3g\mu}{2\rho}\right)^{1/3} \frac{[\text{Ai}(r) + \mathcal{K} \text{Bi}(r)]^2}{[\text{Ai}'(r) + \mathcal{K} \text{Bi}'(r)]^2 - r[\text{Ai}(r) + \mathcal{K} \text{Bi}(r)]^2}, \quad (3.1.13)$$

where

$$r = (s - d^*) / \left(\frac{18\mu^2}{\rho^2 g}\right)^{1/3}, \quad (3.1.14)$$

and \mathcal{K} and d^* are constants. The value of d^* is determined by the condition (3.1.2a), while $\mathcal{K} = 0$ must be imposed to ensure that U remains positive for all $r > 0$. To see this, we note that if $\mathcal{K} \neq 0$, then $\mathcal{K} \text{Bi}(r) \gg \text{Ai}(r)$ when $r \gg 1$ and hence U approaches

$$U \sim \frac{\text{Bi}(r)^2}{\text{Bi}'(r)^2 - r \text{Bi}(r)^2} \sim -2r^{-1/2}. \quad (3.1.15)$$

The fall speed U remains positive for large r only if $\mathcal{K} = 0$, in which case

$$U = \left(\frac{3g\mu}{2\rho}\right)^{1/3} \frac{\text{Ai}(r)^2}{\text{Ai}'(r)^2 - r \text{Ai}(r)^2}. \quad (3.1.16)$$

This velocity profile is shown in figure 3.1. Since the thread accelerates as it stretches under its own weight, it is to be expected that U increases monotonically for $s > s_N$. Hence $d^* - s_N \approx 2.337(18\mu^2/\rho^2 g)^{1/3}$.

The asymptotic behaviour of $\text{Ai}(r)$ for $r \gg 1$ implies that in this limit the fall speed $U(r)$ approaches

$$U \sim \left(\frac{12g\mu}{\rho}\right)^{1/3} \left[\sqrt{r} + O\left(\frac{1}{r}\right) \right]. \quad (3.1.17)$$

Substitution of (3.1.14) into (3.1.17) yields

$$U \sim \sqrt{2g(s - d^*)}, \quad s \gg 1, \quad (3.1.18)$$

which confirms that inertia is dominant at large distances beneath the nozzle.

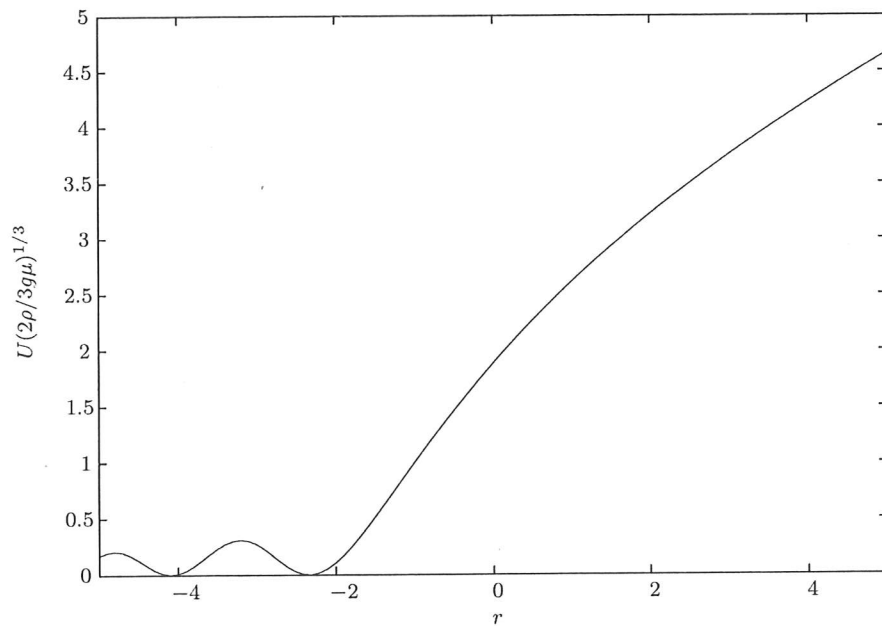


Figure 3.1: The solution (3.1.16) obtained by Clarke (1966). There are many values of $r < 0$ for which $U = 0$, but in order for U to increase monotonically for $r > -d$, the root $r = -2.337$ must be selected as the approximate origin for s .

If $U_N \ll 1$, it is possible to estimate d^* through expansion of (3.1.16) about $r = -2.337$. This expansion implies that

$$U = \frac{1}{2} \left(\frac{3g\mu}{2\rho} \right)^{1/3} \left[(r + 2.337)^2 + O((r + 2.337)^4) \right], \quad (3.1.19)$$

and substitution of (3.1.14) then implies

$$U \sim \frac{\rho g}{6\mu} \left(s - d^* + 2.337 \left(\frac{18\mu^2}{\rho^2 g} \right)^{1/3} \right)^2. \quad (3.1.20)$$

This is consistent with the fall speed (3.1.4) obtained in §3.1.1 using a viscous-gravity balance, with an offset $d = d^* - 6.126(\mu^2/\rho^2 g)^{1/3}$. Substitution of (3.1.6) with $K^2 = \rho g/6\mu$ gives

$$d^* = s_N - \sqrt{\frac{6\mu U_N}{\rho g}} + 6.126 \left(\frac{\mu^2}{\rho^2 g} \right)^{1/3}. \quad (3.1.21)$$

3.2 Nondimensionalisation

In the chapters that follow we analyse the effects of bending stress on a thread that falls a height H through air and then lands on a horizontal surface. Since bending stress is

typically significant only in a small boundary layer at the bottom of the thread, we seek scalings that are relevant to the motion of the thread there. Bending stress does not significantly affect the fall speed of the thread. We can therefore use the analysis of §3.1 to obtain a scaling estimate for the fall speed at a height H beneath the nozzle.

If H is sufficiently small that (3.1.8) holds, then viscous stresses dominate inertia at the bottom of the thread and the relevant velocity scale is $U \sim \rho g H^2 / \mu$. If H is sufficiently large that viscous stress is instead negligible compared to inertia at the bottom of the thread, then the relevant velocity scale is $U \sim \sqrt{gH}$. In the problems we analyse in chapters 4–6, H is typically small enough that inertia does not have a significant effect on the fall speed. This motivates us to nondimensionalise velocities with respect to the extensional velocity scale $U_E = \rho g H^2 / \mu$. The thread radius is nondimensionalised with the corresponding radial scale $a_E = \sqrt{Q / \pi U_E}$, axial lengths with H and angular velocities with U_E / H . The constitutive relation (2.3.22) suggests that the stress components \check{N}_i should be nondimensionalised with $\mu a_E^2 U_E / H$, while the torque balance (2.3.28) suggests that the stress-moment components M_i should be nondimensionalised with $\mu a_E^2 U_E$.

3.2.1 Dimensionless governing equations

The geometry of the centreline is determined by (2.1.1) and (2.1.2), which are

$$\mathbf{x}' = \mathbf{d}_3 \quad (3.2.1)$$

$$\mathbf{d}'_i = \boldsymbol{\kappa} \times \mathbf{d}_3, \quad (3.2.2)$$

where, for a steadily moving thread, the curvature $\boldsymbol{\kappa}$ of the rotating basis is selected so that it is related to the angular velocity $\boldsymbol{\omega}$ of the fluid by

$$\boldsymbol{\kappa} = U^{-1} (\boldsymbol{\omega} - \omega_0 \mathbf{d}_3). \quad (3.2.3)$$

The force and torque balances are given by (2.3.23) and (2.3.28), which after nondimensionalisation are

$$\check{\mathbf{N}}' = \pi a^2 \mathbf{e}_z \quad (3.2.4)$$

$$\mathbf{M}' = \mathbf{d}_3 \times \check{\mathbf{N}} + \mathcal{M}. \quad (3.2.5)$$

We will see that \mathcal{M} is asymptotically negligible when we include it in the analysis in later chapters. Finally, the dimensionless form of the constitutive relations (2.3.15) and (2.3.22)

for \mathbf{M} and \check{N}_3 are

$$\mathbf{M} = \frac{\pi a^4}{4} \epsilon^2 (\mathbf{3I} - \mathbf{d}_3 \mathbf{d}_3) \cdot \boldsymbol{\omega}', \quad (3.2.6)$$

$$\check{N}_3 = 3\pi a^2 U' + \pi \Gamma a - \pi \text{Fr} a^2 U^2, \quad (3.2.7)$$

where the dimensionless parameters

$$\epsilon = \frac{a_E}{H}, \quad \text{Fr} = \frac{U_E^2}{gH} \quad \text{and} \quad \Gamma = \frac{\gamma}{\rho g H a_E} \quad (3.2.8a-c)$$

represent respectively the slenderness of the thread, the relative importance of inertia and gravity at the bottom of the thread, and the relative importance of surface tension and gravity. In the problems we consider, there is a fourth dimensionless parameter,

$$U_n = \frac{U_N}{U_E}, \quad (3.2.8d)$$

that represents the extent by which a thread is stretched by gravity as it falls from the nozzle before landing.

In the experiments we analyse, extrusion is driven by gravity from a reservoir with a constant pressure head. In the simple case that the reservoir has depth D and a vertical outlet pipe of length L and radius a_N , the flow in the pipe is given by Poiseuille flow and the volume flux is $Q = \pi a_N^4 \rho g (D/L + 1) / 8\mu$. Hence $U_N = a_N^2 \rho g (D/L + 1) / 8\mu$, and substitution of $a_N^2 = a_E^2 U_E / U_N$ and $\rho g H^2 / \mu = U_E$ yields

$$\frac{U_N^2}{U_E^2} = \frac{a_E^2}{8H^2} \left(\frac{D}{L} + 1 \right)^2. \quad (3.2.9)$$

Hence $U_n \propto \epsilon$ for gravity-driven extrusion and $U_n \ll 1$ follows from $\epsilon \ll 1$.

3.2.2 Significance of parameters

After nondimensionalisation, the behaviour of a slender thread that is extruded from a nozzle depends on the four independent parameters U_n , ϵ , Γ and Fr . The analysis in chapters 4–6 concerns the fall of slender threads for which extensional stresses are important, and which therefore fall within the regime $0 < \epsilon \ll 1$ and $U_n \ll 1$.

The parameter Fr represents the relative importance of inertia and viscosity at the bottom of the thread. This is most easily seen by noting that

$$\text{Fr} = \frac{U_E^2}{gH} = \frac{\rho^2 g H^3}{\mu^2}. \quad (3.2.10)$$

Experiment	U_n	ϵ	Fr	Γ
CWL	9×10^{-5} – 1×10^{-3}	3×10^{-4} – 4×10^{-3}	0.5–30	0.79
Morris <i>et al.</i> (2007)	2×10^{-4} – 4×10^{-3}	8×10^{-4} – 1×10^{-2}	0.1–7.	0.45
Mahadevan <i>et al.</i> (1998)	2×10^{-4} – 4×10^{-3}	1×10^{-3} – 5×10^{-3}	8.–60	–
Maleki <i>et al.</i> (2006)	6×10^{-5} – 4×10^{-2}	4×10^{-5} – 2×10^{-2}	0.09–1000	0.24

Table 3.1: Parameter values representative of recent experiments for the range of fall heights used. In the papers for which several different fluids and extrusion conditions were used, the particular parameters used here are for Experiment 5 of CWL, Experiment 2 of Mahadevan *et al.* (1998) and Experiment 2 of Maleki *et al.* (2006). The experimental parameters for Mahadevan *et al.* (1998) are not fully reported, but here the estimates of R04 are used.

The condition (3.1.8) implies that inertia is negligible at the bottom of the thread if $Fr \ll 1$. Conversely, inertia is dominant at the bottom of the thread if $Fr \gg 1$. In §3.5 and chapter 6.4 we analyse threads for which $Fr \gg 1$, but otherwise we assume that the fall of the thread is dominated by a viscous–gravity balance and set $Fr = 0$ for simplicity. As mentioned in §3.1.1, we will typically also omit the effects of surface tension for simplicity, and set $\Gamma = 0$. We note that if $Fr = \Gamma = 0$ then from (2.3.21) the ‘effective axial stress’ \check{N} reduces to the viscous extensional stress N .

Table 3.1 shows parameter values that are representative of recent laboratory experiments. These values show the relevance of the regime $\epsilon \ll 1$ and $U_n \ll 1$. Depending on the particular experiment, inertial forces at the bottom of the thread are either negligible, dominant or about the same size as the gravitational forces there. The values of Fr shown in table 3.1 imply that a wide range of values of Fr may be reached experimentally. While the inclusion of surface tension affects the fall speed of the thread before it lands, it does not significantly change the dominant physical processes that govern the bending motion at the bottom of the thread (see R04).

3.3 Stress-free vertical fall of a viscous thread of finite height for $Fr \ll 1$

We have so far analysed an infinitely long thread that falls under its own weight. In the problems we analyse in the later chapters, the thread lands on a surface after falling through a finite height which we scale to unity. After landing, the weight of the thread is supported by the surface. Hence the vertical velocity variation of the finite thread differs from that in an infinitely long thread since the finite thread is not stretched by the weight of any fluid further than unit height beneath the nozzle. To derive the vertical velocity variation in the finite thread, we therefore consider a thread falling steadily under its own weight, with the boundary condition that the fluid ‘vanishes’ from the system as it falls

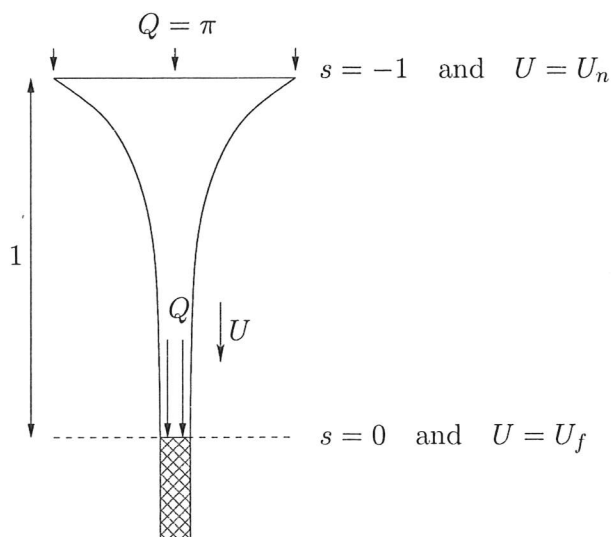


Figure 3.2: Schematic diagram of a falling vertical thread. Under the 'free-fall' condition, the thread is assumed to 'vanish' after falling through a unit dimensionless height from the nozzle, so that the weight below that plays no dynamical role.

through unit height below the nozzle. This has the consequence that the thread at this height is stress-free. This problem is depicted in figure 3.2.

After falling through unit height, the thread has a fall speed U_f ; we call this speed the 'free-fall' speed in the sense that in this problem there is no stress applied to the bottom of the thread. The free-fall speed, defined in this way, plays a major role in the theory described in the rest of the thesis. (This use of free-fall speed should not be confused with the idea of free-fall in mechanics for a pure inertia-gravity balance.)

If we assume that $Fr = \Gamma = 0$, then the dimensionless form of (3.1.3) is

$$\left(\frac{3U'}{U}\right)' + \frac{1}{U} = 0. \quad (3.3.1)$$

The boundary conditions for the free-fall problem are

$$U = U_n \quad \text{at} \quad s = -1 \quad \text{and} \quad U' = 0 \quad \text{at} \quad s = 0, \quad (3.3.2a,b)$$

where we have defined the origin $s = 0$ to be at the bottom of the thread. The first boundary condition imposes the extrusion velocity at the nozzle, and the second boundary condition imposes zero viscous stress at the bottom of the thread. The solution to this problem was found by R04 in another context; however in §3.4.1 and §3.5.2 we also analyse the case when $U' \neq 0$ at the bottom of the thread, and therefore we briefly describe the solution.

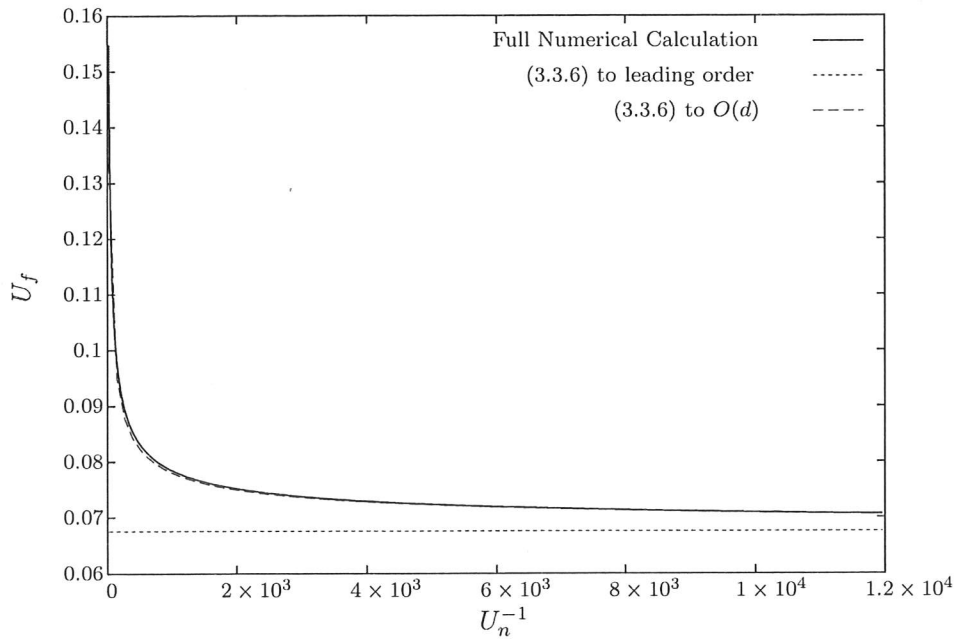


Figure 3.3: Comparison of the leading-order and $O(d)$ estimates (3.3.6) for U_f with the full numerical solution to (3.3.1) and (3.3.2), for a range of $U_n \ll 1$.

The general solution to (3.3.1) for which $U' = 0$ at some finite distance beneath the nozzle is given by

$$U(s) = \frac{1 - \cos[T_\infty(s + 1 + d)]}{3T_\infty^2}, \quad (3.3.3)$$

where T_∞ and d are constants of integration. These constants can be chosen so as to satisfy (3.3.2): the stress-free condition (3.3.2b) gives

$$T_\infty = \frac{\pi}{1 + d}; \quad (3.3.4)$$

since we assume that $U_n \ll 1$, expansion of (3.3.3) together with (3.3.4) and (3.3.2a) gives

$$d = \sqrt{6U_n} + O(U_n). \quad (3.3.5)$$

The dimensionless free-fall speed U_f is given by setting $s = 0$ in (3.3.3). For $d \ll 1$, we obtain

$$U_f = \frac{2}{3\pi^2} (1 + 2d) + O(d^2). \quad (3.3.6)$$

Figure 3.3 compares this estimate with the full numerical solution to (3.3.1) and (3.3.2) for values of U_n representative of experiments. There is good agreement, and the leading-order estimate $U_f = 2/3\pi^2$ is typically accurate to within 15%.

3.4 The effects of small forces exerted at the bottom of the thread for $Fr \ll 1$

Here we consider the effects of a small force exerted at the bottom of the thread as a perturbation to the free-fall problem. We will see in later chapters that bending forces at the bottom of the thread are small, but their effects will nonetheless result in a global perturbation to the thread. A vertical force will modify the vertical velocity variation in the thread, while a horizontal force will deflect the thread and thus modify its shape. We now describe these effects in more detail.

3.4.1 Deceleration due to a small vertical force

A small vertical force F_z exerted at the bottom of the thread will slow its fall and cause the fluid velocity U_b at the bottom to be slightly smaller than the free-fall value U_f . To determine the relationship between F_z and U_b , we solve (3.3.1) with the boundary condition (3.3.2b) replaced by

$$U = U_b \quad \text{at} \quad s = 0. \quad (3.4.1)$$

The force F_z is then given by

$$F_z = 3\pi a^2 U' \quad \text{at} \quad s = 0. \quad (3.4.2)$$

In general, the constants T_∞ and d in (3.3.3) must be found numerically in order to determine the velocity profile and the value of F_z . However, since F_z is small then $U_b \approx U_f$ and it is possible to estimate U_b by making an expansion in F_z . For simplicity we neglect the $O(d)$ corrections below, but they may readily be included in the expansion which follows.

We perturb T_∞ away from its free-fall value to

$$T_\infty = \pi + t, \quad (3.4.3)$$

where $t \ll 1$. This is substituted into (3.4.2) using (3.3.3) to obtain

$$F_z = \frac{\pi a_b^2}{T_\infty} \sin T_\infty = -a_b^2 t + O(t^2). \quad (3.4.4)$$

A similar expansion for U_b using (3.3.3) and (3.4.1) implies that

$$U_b - U_f = -\frac{4t}{3\pi^3} + O(t^2). \quad (3.4.5)$$

Combination of (3.4.4) with (3.4.5) together with $a_b^2 \approx 1/U_f$ gives

$$F_z = \frac{3\pi^3}{4U_f}(U_b - U_f) + O((U_f - U_b)^2). \quad (3.4.6)$$

In §4.5 and chapter 5, we demonstrate that the behaviour of a thread, dragged by a belt at speed U_b , is described by a parameter Φ_z , which is defined by

$$\Phi_z = \frac{F_z}{\pi a_b^2 \delta_g}, \quad (3.4.7)$$

where δ_g is the lengthscale of the bending boundary layer and is determined in §4.5. The value of Φ_z is therefore related to U_b by

$$\Phi_z = \frac{3\pi^2}{4\delta_g}(U_f - U_b) + O\left(\frac{(U_f - U_b)^2}{\delta_g}\right). \quad (3.4.8)$$

3.4.2 Deflection due to a small horizontal force

A horizontal force exerted at the bottom of the thread causes it to be deflected from vertical, and to hang in a catenary-like shape. Here, we aim to determine the position of the bottom of this catenary. We will see in §4.5 and §6.5 that the horizontal displacement of the bottom of the catenary from beneath the nozzle provides an estimate for the distance by which a thread is dragged as it falls onto a moving belt, and for the coiling radius of a thread as it falls onto a stationary surface. In the later chapters we estimate this displacement using the approximation that the variation of the thread's radius towards the nozzle can be neglected, which we justify here.

Consider a tail of unit length and radius a , hanging under its own weight and with a horizontal force F_x exerted on it in the x direction, so that it takes the shape of a half-catenary. In the absence of any force applied in the y direction, (3.2.1) and (3.2.4) simplify to

$$x' = \sin \theta \quad (3.4.9)$$

$$z' = -\cos \theta \quad (3.4.10)$$

$$(N_3 \sin \theta)' = 0 \quad (3.4.11)$$

$$(N_3 \cos \theta)' = -\pi a^2, \quad (3.4.12)$$

where $\cos \theta = -\mathbf{d}_3 \cdot \mathbf{e}_z$. Equation (3.4.11) has a first integral

$$N_3 \sin \theta = F_x, \quad (3.4.13)$$

which can be substituted back into (3.4.12) to obtain

$$\theta' = \frac{\pi a^2 \sin^2 \theta}{F_x}. \quad (3.4.14)$$

From (3.4.9) and (3.4.14) the horizontal deflection x_t of the tail is

$$x_t = \int_{\pi/2}^{\theta_n} \frac{F_x}{\pi a^2 \sin \theta} d\theta, \quad (3.4.15)$$

where θ_n is the deflection of the tail from vertical at $s = -1$.

The deflection of a catenary with uniform radius $a = 1$ is given by

$$x_t = \frac{F_x}{\pi} \ln \left(\tan \left(\frac{\theta_n}{2} \right) \right), \quad (3.4.16)$$

where θ_n is found by integration of (3.4.14) with $a = 1$ to be

$$\theta_n = \cot^{-1} \left(\frac{\pi}{F_x} \right). \quad (3.4.17)$$

Hence $x_t = O(F_x \ln F_x)$ as $F_x \rightarrow 0$. Equation (3.4.14) implies that $\theta = O(1)$ only near the bottom where $s = O(F_x)$. This region gives only an $O(F_x)$ contribution to x_t . From (3.4.17), $\theta_n = O(F_x)$ and hence (3.4.15) implies that the contribution of the region $\theta = O(\theta_n)$ is also only $O(F_x)$, despite the $O(1)$ arclength of this region. Hence the deflection is dominated by the region $\theta_n \ll \theta \ll \pi/2$, which corresponds to arclengths $0 \ll -s \ll 1$. Linearisation of θ in (3.4.15) and substitution of (3.4.17) implies that this region indeed gives an $O(F_x \ln F_x)$ contribution.

The variation of a within a non-uniform catenary is found by considering (3.2.7) together with (3.4.13) to obtain

$$a' = O \left(\frac{F_x}{\sin \theta} \right). \quad (3.4.18)$$

When $-s \ll 1$, it follows that $\theta \gg F_x$ and hence $a' \ll 1$ in this region. Thus the variation in thread radius has no effect on x_t to leading order since $a \approx a_b$ when $0 \ll -s \ll 1$. The dominant contribution to x_t from the region $0 \ll -s \ll 1$ may therefore be estimated to leading order by assuming that the thread has constant radius $a = a_b$.

3.5 Vertical fall of an inertia-dominated thread for $\text{Fr} \gg 1$

In §6.4 we analyse the steady coiling of a thread for the case where inertia plays an important role at the bottom of the thread. Here we derive the free-fall speed of an inertia-dominated thread and the deceleration at the bottom of the thread due to a vertical force

exerted there. In the presence of inertia, (3.3.1) is modified to

$$\left(\frac{3U'}{U}\right)' - \text{Fr} U' + \frac{1}{U} = 0. \quad (3.5.1)$$

3.5.1 The free-fall speed of an inertia-dominated thread

The dimensional free-fall speed U_F for an inertia-dominated thread is obtained by substituting (3.1.21), $s_N = -H$ and $s = 0$ into (3.1.18) to obtain

$$U_F = \sqrt{2gH + 6.126 \left(\frac{\mu^2 g^2}{\rho^2}\right)^{1/3} + \left(\frac{6\mu g U_N}{\rho}\right)^{1/2}}. \quad (3.5.2)$$

After nondimensionalising with respect to the scalings in §3.2, this estimate is

$$U_f = \sqrt{\frac{2}{\text{Fr}} + \frac{6.126}{\text{Fr}^{4/3}} + \frac{(6U_n)^{1/2}}{\text{Fr}}}, \quad (3.5.3)$$

where the second and third terms are correction terms to the leading-order estimate. Which of these terms is the larger correction term depends on the relative sizes of $\text{Fr}^{-1/3}$ and $U_n^{1/2}$.

3.5.2 Deceleration due to a vertical force

In §6.4 we will show that when inertial forces are important at the bottom of a coiling thread, the momentum flux at the bottom of the tail must be diverted so that the thread is horizontal at the contact point. This places the bottom of the thread under compression, and it buckles to form a coil. We show in §6.4 that the coil undergoes axial compression in addition to bending. Since bending motion decays towards the tail, we conclude that the coiling motion places the bottom of the tail under axial compression. To analyse this effect, we consider a falling thread for which the force exerted at the bottom of the thread is vertical and scales with the momentum flux. This imposes the boundary condition

$$\frac{3U'}{U} = -\alpha \text{Fr} U \quad \text{at } s = 0, \quad (3.5.4)$$

where α is a constant that we show in §6.4 to be determined by a balance of bending and inertial forces in the coil. We note that R04 considered a similar problem, but assumed that there is no axial compression at the bottom of the tail; this corresponds to setting $\alpha = 0$ in (3.5.4). However, since the coil places the bottom of the tail under compression, $\alpha > 0$.

The estimate (3.5.3) implies that the speed near the bottom of the thread scales like $\text{Fr}^{-1/2}$ at leading order. Substituting this scaling into (3.5.4) yields a lengthscale $\delta_b \sim \text{Fr}^{-1/2}$ on which viscous and inertial stresses are both $O(\text{Fr})$ and in balance at the bottom of the thread. In this region, the gravitational term in (3.1.7) is $O(\text{Fr}^{1/2})$ and hence negligible. The vertical velocity variation at the bottom of the thread is therefore given by

$$\left(\frac{3U'}{U}\right)' - \text{Fr} U' = O(\text{Fr}^{1/2}). \quad (3.5.5)$$

To leading order, (3.5.5) can be integrated once and the boundary condition (3.5.4) used to show that the vertical force is constant and given by

$$\frac{3U'}{U} - \text{Fr} U = -(\alpha + 1)\text{Fr} U_b, \quad (3.5.6)$$

where U_b is the fall speed at the bottom of the tail. The solution of (3.5.6) for which $U = U_b$ at $s = 0$ is

$$U = \frac{(1 + \alpha)U_b}{1 + \alpha e^{\beta s}}, \quad \text{where } \beta = \frac{(1 + \alpha)\text{Fr} U_b}{3}. \quad (3.5.7a,b)$$

Since $\text{Fr} U_b \gg 1$ and $\alpha > 0$, it follows that $\beta \gg 1$. This solution shows that the thread decelerates within a boundary layer where $\beta s = O(1)$, or $s = O(\text{Fr}^{-1/2})$. In the limit $\beta s \rightarrow -\infty$ the fall speed in the boundary-layer solution must match to the fall speed in the tail for $s \ll 1$, which is the free-fall speed U_f , as derived in §3.5.1. Hence the fall speed U_b at the bottom of the tail is related to U_f and to the value of α by

$$U_b = \frac{U_f}{1 + \alpha}. \quad (3.5.8)$$

We show in chapter 6 that the value of α is determined by the coil to be approximately $\alpha = 0.35$. The coiling speed is given by U_b to leading order, and hence may be estimated from (3.5.8) using (3.5.3).

3.6 The whirling of a viscous thread

In §6.6 we analyse the steady coiling of a thread for which Fr is small enough that the axial momentum flux is negligible compared with the viscous extensional stress as the thread falls, but large enough that the stress caused by centrifugal acceleration of the thread is comparable with the viscous hoop stress caused by deflection of the thread from vertical. Ribe *et al.* (2006b) (hereafter R06b) suggested that in this regime, the thread exhibits a resonant behaviour when the coiling frequency coincides with an eigenfrequency of an

unforced ‘whirling liquid string’. This string is modelled as a viscous thread whose radius is governed by extensional flow. The effects of bending stress in the thread as it is deflected are assumed to be negligible compared with those of hoop stress and are omitted. In the absence of any forcing applied at the bottom of the thread, steady rotational motion can occur only at discrete angular frequencies. Between these frequencies, the only possible steady behaviour of the thread is to hang vertically. In chapter 6 we show that bending stresses at the bottom of the thread exert a small force on the thread above, and that during fluid coiling the thread behaves like a (slightly) forced circular pendulum. Here we analyse the behaviour of such a pendulum.

We work in a reference frame that rotates about \mathbf{e}_z with the forced angular frequency Ω . In this frame, the thread is stationary but fictitious forces have been introduced which correspond to centrifugal and Coriolis accelerations. The motion of the thread in the absence of bending stress is governed by

$$\check{\mathbf{N}} = \check{N}_3 \mathbf{x}' \quad (3.6.1a)$$

$$\check{\mathbf{N}}' = \pi a^2 \text{Fr} [\boldsymbol{\Omega} \times (\boldsymbol{\Omega} \times \mathbf{x}) + 2U\boldsymbol{\Omega} \times \mathbf{x}'] + \pi a^2 \mathbf{e}_z, \quad (3.6.1b)$$

where $\boldsymbol{\Omega} = \Omega \mathbf{e}_z$ and we have made the substitution $\mathbf{d}_3 = \mathbf{x}'$.

3.6.1 Constant radius

The thread stretches as it falls, which causes its radius to vary along its length. For simplicity, we assume for the moment that the thread’s radius is instead constant so that $a = a_c$ and $U = U_c$ everywhere. We will discuss the effects of variation in the thread’s radius in §3.6.2.

Provided the forcing is small and the frequency Ω is not an eigenfrequency of an unforced thread, the resulting deflection of the thread is also small. We linearise in the deflection of the thread from vertical, so that at leading order the tangent vector is given by

$$\mathbf{x}' = x' \mathbf{e}_x + y' \mathbf{e}_y - \mathbf{e}_z, \quad (3.6.2)$$

Substitution of (3.6.2) into (3.6.1) and projection onto \mathbf{e}_z yields $\check{N}'_3 = -\pi a_c^2$. We make the leading-order approximation that $\check{N}_3 = 0$ at $s = 0$. Hence

$$\check{N}_3 = -\pi a_c^2 s. \quad (3.6.3)$$

Substitution of (3.6.2) and (3.6.3) into (3.6.1) and then projection onto \mathbf{e}_x and \mathbf{e}_y yields

$$(-sx')' = \text{Fr} [-\Omega^2 x - 2U_c \Omega y'] \quad (3.6.4a)$$

$$(-sy')' = \text{Fr} [-\Omega^2 y + 2U_c \Omega x']. \quad (3.6.4b)$$

We may treat both horizontal components of displacement together by using the complex variable $\mathcal{Z} = x + iy$. It is convenient also to define the parameters $\mathcal{W}^2 = \text{Fr} \Omega^2$ and $\mathcal{E} = \text{Fr} \Omega U_c$. We are interested in the regime where the dominant balance is between hoop stress and centrifugal acceleration, and we have nondimensionalised so that variation in the tail occurs over an $O(1)$ lengthscale. We therefore require $\mathcal{W} = O(1)$. It is known (e.g. R04) that the dimensionless coiling frequency Ω is large for a slender thread. We therefore consider the case where $\mathcal{E} \ll 1$ and hence where Coriolis acceleration is typically negligible compared with centrifugal acceleration.

After multiplying through by $-s$, (3.6.4) is given by

$$-s(-s\mathcal{Z}')' - 2i\mathcal{E}s\mathcal{Z}' - \mathcal{W}^2 s\mathcal{Z} = 0. \quad (3.6.5)$$

This equation has a closed-form solution which we now derive. We change variables using $\tau = 2\mathcal{W}\sqrt{-s}$. The differential operator $-s d/ds$ is equivalent to $\frac{1}{2}\tau d/d\tau$, and hence

$$\tau \frac{d}{d\tau} \left(\tau \frac{d\mathcal{Z}}{d\tau} \right) + 4i\mathcal{E}\tau \frac{d\mathcal{Z}}{d\tau} + \tau^2 \mathcal{Z} = 0. \quad (3.6.6)$$

After multiplying this equation through by $\tau^{2i\mathcal{E}}$, it is straightforward to show that it is equivalent to

$$\tau^2 (\tau^{2i\mathcal{E}} \mathcal{Z})'' + \tau (\tau^{2i\mathcal{E}} \mathcal{Z})' + (\tau^2 + 4\mathcal{E}^2) \tau^{2i\mathcal{E}} \mathcal{Z} = 0. \quad (3.6.7)$$

This is Bessel's equation for the unknown quantity $\tau^{2i\mathcal{E}} \mathcal{Z}$, and the general solution is

$$\mathcal{Z} = [AJ_{2i\mathcal{E}}(\tau) + BJ_{-2i\mathcal{E}}(\tau)] \tau^{-2i\mathcal{E}}, \quad (3.6.8)$$

where A and B are arbitrary complex-valued constants and $J_{\pm 2i\mathcal{E}}(\tau)$ are Bessel functions.

Using $\partial J_n(\tau)/\partial n|_{n=0} = \frac{1}{2}\pi Y_0(\tau)$ and the expansion $\tau^{-2i\mathcal{E}} \approx 1 - 2i\mathcal{E} \ln \tau + O(\mathcal{E}^2)$, the leading-order behaviour of (3.6.8) when $\mathcal{E} \ll 1$ is given by

$$\mathcal{Z} = (1 - 2i\mathcal{E} \ln \tau)[(A + B)J_0(\tau) + \pi i\mathcal{E}(A - B)Y_0(\tau)] + O(\mathcal{E}^2). \quad (3.6.9)$$

The thread is pinned at a nozzle so that $x = y = 0$ at $s = -1$. Hence $\mathcal{Z} = 0$ when $\tau = 2\mathcal{W}$ and the relevant solution is given by

$$\mathcal{Z} = \mathcal{A}(1 - 2i\mathcal{E} \ln \tau)\{J_0(2\mathcal{W})Y_0(\tau) - Y_0(2\mathcal{W})J_0(\tau)\} + O(\mathcal{E}^2), \quad (3.6.10)$$

where \mathcal{A} is a complex-valued constant.

In chapter 6 we model the forcing due to bending stress in the coil by prescribing a forcing at a small arclength $0 < -s_0 \ll 1$, whose value is derived from an estimate of the height below which bending stress is dominant and above which hoop stress is instead dominant. Since $|s_0| \ll 1$, it follows that $\tau_0 \ll 1$. From (3.6.1a) and (3.6.3), the horizontal force $\check{N}_x + i\check{N}_y$ is given by $\check{N}_h = -\pi a_c^2 s d\mathcal{Z}/ds$ at leading order, which implies that

$$\check{N}_h = \frac{\pi a_c^2 \tau_0 \mathcal{A}}{2} (1 - 2i\mathcal{E} \ln \tau_0) \{J_0(2\mathcal{W})Y_0'(\tau_0) - Y_0(2\mathcal{W})J_0'(\tau_0)\} - \pi a_c^2 i\mathcal{E}\mathcal{Z} + O(\mathcal{E}^2). \quad (3.6.11)$$

We may describe the response of the thread at a given frequency by using the ratio \mathcal{Z}/\check{N}_h . Since we have linearised the problem, we anticipate that $\mathcal{Z}/\check{N}_h = O(1)$ for all frequencies except those that are near the eigenfrequencies Ω_n of an unforced thread. When $\Omega \approx \Omega_n$, a small force results in a large displacement at the bottom of the thread and so we expect that \mathcal{Z}/\check{N}_h is large when $\Omega = \Omega_n$.

We expand \check{N}_h^{-1} for $\mathcal{E} \ll 1$ using (3.6.11), which gives

$$\check{N}_h^{-1} = \frac{2}{\pi a_c^2 \tau_0 \mathcal{A} \{J_0(2\mathcal{W})Y_0'(\tau_0) - Y_0(2\mathcal{W})J_0'(\tau_0)\}} \left(1 + O\left(\mathcal{E} \ln \tau_0, \frac{\mathcal{E}\mathcal{Z}}{\check{N}_h}\right) \right), \quad (3.6.12)$$

and combine this expansion with (3.6.10) to obtain

$$\frac{\pi a_c^2 \mathcal{Z}}{\check{N}_h} = \frac{2}{\tau_0} \frac{J_0(2\mathcal{W})Y_0(\tau_0) - Y_0(2\mathcal{W})J_0(\tau_0)}{J_0(2\mathcal{W})Y_0'(\tau_0) - Y_0(2\mathcal{W})J_0'(\tau_0)} + O\left(\mathcal{E}\mathcal{Z} \ln \tau_0, \frac{\mathcal{E}\mathcal{Z}^2}{\check{N}_h^2}\right). \quad (3.6.13)$$

We prescribe the forcing at $\tau_0 \ll 1$, and we may estimate the behaviour of (3.6.13) by substituting the leading-order expansions

$$\begin{aligned} J_0(\tau_0) &= 1 + O(\tau_0^2) & \text{and} & & J_0'(\tau_0) &= -\frac{\tau_0}{2} + O(\tau_0^3) \\ \pi Y_0(\tau_0) &= 2 \ln \tau_0 + O(1) & \text{and} & & \pi Y_0'(\tau_0) &= \frac{2}{\tau_0} + O(\tau_0 \ln \tau_0), \end{aligned}$$

for the Bessel functions near $\tau_0 = 0$. This yields

$$\frac{\pi a_c^2 \mathcal{Z}}{\check{N}_h} \approx \frac{8J_0(2\mathcal{W}) \ln \tau_0 - 4\pi Y_0(2\mathcal{W})}{4J_0(2\mathcal{W}) + \pi\tau_0^2 Y_0(2\mathcal{W})}. \quad (3.6.14)$$

At fixed $\tau_0 \ll 1$, the response scales like $\ln \tau_0$ when $J_0(2\mathcal{W}) \neq 0$. However, if $J_0(2\mathcal{W}) \approx 0$ then the response instead scales like τ_0^{-2} . The resonant frequencies Ω_n observed by R06b correspond to values of \mathcal{W}_n that satisfy $J_0(2\mathcal{W}_n) = 0$. This has the physical interpretation

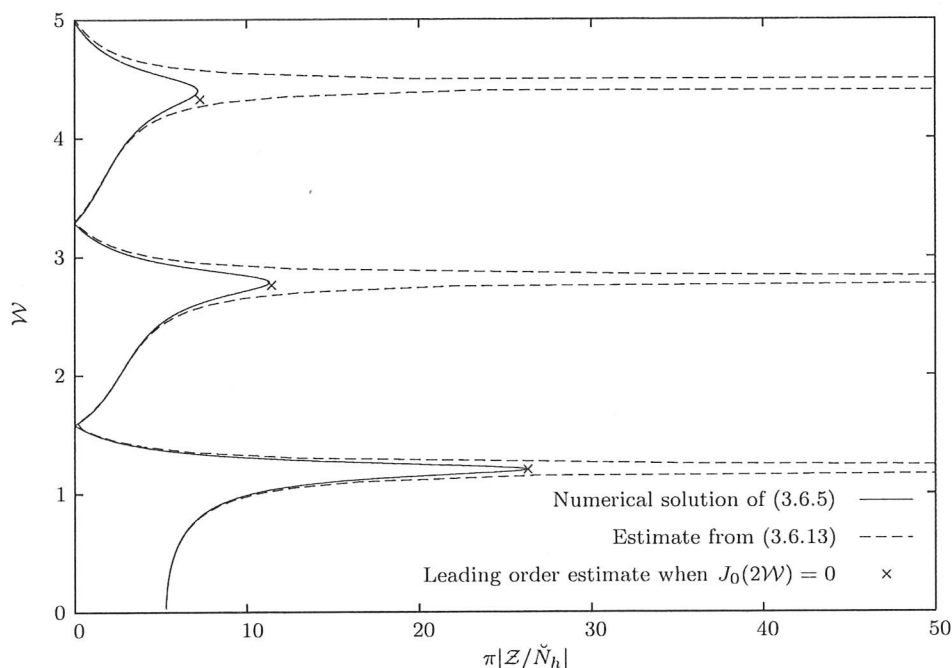


Figure 3.4: The response of a thread whose radius is constant ($U = a = 1$) and for which $\text{Fr} = 10^{-3}$ that is forced to rotate at rescaled frequency \mathcal{W} through a forcing prescribed at $s_0 = -5 \times 10^{-3}$. The estimate (3.6.13) gives good agreement with the numerical solution to (3.6.5) provided the forcing frequency is not too close to one of the resonant frequencies. At these frequencies, for which $J_0(2\mathcal{W}) = 0$, the estimate $\pi|\mathcal{Z}/\check{N}_h| \sim (\text{Fr} \Omega)^{-1}$ gives reasonable agreement.

that, while an $O(1)$ forcing results in an $O(\ln \tau_0)$ displacement when Ω is not close to one of the eigenfrequencies Ω_n , it results in a very large $O(\tau_0^2)$ displacement when $\Omega \approx \Omega_n$.

The estimate (3.6.14) has been derived under the assumption that Coriolis acceleration is negligible so that $\mathcal{E} \approx 0$. However, if $J_0(2\mathcal{W}) \approx 0$ then the omission of Coriolis acceleration is no longer valid. To see this, we note that if $J_0(2\mathcal{W}) = 0$ then the leading-order contribution to \check{N}_h in (3.6.11) is from the Coriolis acceleration. In this case we expect that $\pi a_c^2 |\mathcal{Z}/\check{N}_h| \approx 1/\mathcal{E} = (\text{Fr} \Omega)^{-1}$. This is shown in figure 3.4, which compares both the estimate (3.6.13) and $\pi a_c^2 |\mathcal{Z}/\check{N}_h| = 1/\mathcal{E}$ to the numerical solution of (3.6.5) subject to $\mathcal{Z} = 0$ at $s = -1$ and $\mathcal{Z}' = 1$ at $s = s_0$. The parameter values used are $s_0 = -5 \times 10^{-3}$ and $\text{Fr} = 10^{-3}$. While (3.6.13) gives good agreement away from the resonant frequencies, it breaks down close to them when the response is large since it has omitted the Coriolis acceleration.

3.6.2 Non-constant radius

We have so far assumed that the radius of the thread is constant. In the coiling problem we analyse in chapter 6, the thread is stretched by gravity as it falls and its radius therefore

varies. From (3.6.1*b*), this variation in radius changes the deflection of the thread by the force from the coil at the bottom.

If the deflection of the thread from vertical is small, then the equations that govern the variation of velocity and axial stress are obtained at leading order using (3.2.7) and the projection of (3.6.1*b*) onto \mathbf{d}_3 , which give

$$\check{N}_3 = 3\pi a^2 U' \quad \text{and} \quad \check{N}'_3 = -\pi a^2. \quad (3.6.15a,b)$$

The solution for $U(s)$ with $\check{N}_3 = 0$ at $s = 0$ was derived in §3.3, and is given by

$$U = \frac{1 - \cos[T_\infty(s + 1 + d)]}{3T_\infty^2} \quad \text{and} \quad T_\infty = \frac{\pi}{1 + d}, \quad (3.6.16a,b)$$

where d is a constant that is chosen to satisfy $U = U_n$ at $s = -1$. For simplicity we set $d = 0$ below, which corresponds to the limit of a very strongly stretched thread.

We substitute (3.6.1*a*) into (3.6.1*b*) to obtain $\check{\mathbf{N}}' = \check{N}'_3 \mathbf{x}' + \check{N}_3 \mathbf{x}''$. The velocity variation (3.6.16) together with (3.6.15) implies that $\check{N}_3 = a^2 \sin[\pi(1 + s)]$. We substitute this into (3.6.1*b*) and project (3.6.1*b*) onto \mathbf{e}_x and \mathbf{e}_y to obtain

$$\frac{1}{\pi} \sin[\pi(1 + s)] x'' = x' + \text{Fr}[-\Omega^2 x - 2U\Omega y'] \quad (3.6.17a)$$

$$\frac{1}{\pi} \sin[\pi(1 + s)] y'' = y' + \text{Fr}[-\Omega^2 y + 2U\Omega x']. \quad (3.6.17b)$$

Equation (3.6.17) is similar to the equation derived by R06b for a free strongly-stretched thread, though here we have additional terms that represent the Coriolis accelerations which are important near resonance.

As in §3.6.1, the thread exhibits resonant behaviour when the forcing frequency is close to one of the eigenfrequencies of an unforced thread. These eigenfrequencies were calculated numerically for threads of non-constant radius by R06b, and they differ from the eigenfrequencies of a thread of constant radius because of the different weight distribution in the thread. The qualitative behaviour of a forced thread of non-constant radius is the same as that of a forced thread of constant radius at leading order. Figure 3.5 shows the response of such a forced thread, and includes the effects of variation in the radius and of Coriolis acceleration. The response is calculated numerically by solving (3.6.1) and (3.6.16) with $\text{Fr} = 10^{-3}$ subject to $x = y = 0$ and $U = 10^{-3}$ at $s = -1$, and $\check{N}_3 = 0$ and $\mathcal{Z}' = 1$ at $s = -5 \times 10^{-3}$. The response of the thread between resonant frequencies is very similar to that of a thread whose radius is constant.

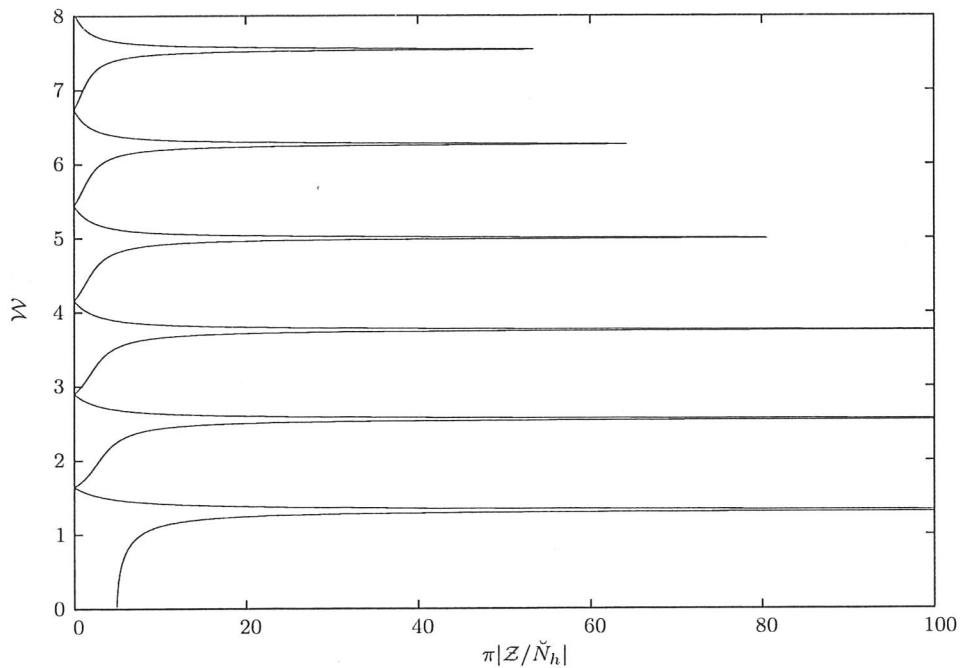


Figure 3.5: The response of a thread of non-constant radius for which $\text{Fr} = 10^{-3}$ and which is forced to rotate at rescaled frequency \mathcal{W} through a forcing prescribed at $s_0 = -5 \times 10^{-3}$. This was obtained through solution of (3.6.1) and (3.6.16), with $U = 10^{-3}$ at $s = -1$. The response is qualitatively the same as that of a thread whose radius is constant.

3.7 Discussion

The analysis of this chapter has concerned problems that are related to the behaviour of a slender viscous ‘tail’ as it falls under gravity. We have obtained quantitative estimates for the fall speed at the bottom, and in some regimes have determined the perturbations to the tail that result from a small force exerted there. We have shown that these perturbations modify both the vertical velocity profile and the shape of the tail. In later chapters we will see that bending forces at the bottom of the tail modify its behaviour, and the results derived in this chapter are relevant to the work that follows.

We have also derived appropriate scalings to describe the behaviour of the bottom of the thread. Nondimensionalisation with respect to these scalings reveals that the fall of a slender thread onto a surface may be characterised by four independent parameters. R06b performed experiments in which the height of fall was varied while the flux and nozzle diameter were held constant. They defined two dimensionless groups to describe the nozzle conditions, omitting surface tension, which are

$$\Pi_1 = \left(\frac{\nu^5}{gQ^3} \right)^{1/5} \quad \text{and} \quad \Pi_2 = \left(\frac{\nu Q}{gd^4} \right)^{1/4}, \quad (3.7.1)$$

where $\nu = \mu/\rho$ is the kinematic viscosity of the fluid and $d = 2a_N$ is the diameter of the nozzle. If surface tension is included, then there is a third dimensionless parameter (Ribe *et al.*, 2006a), given by

$$\Pi_3 = \frac{\gamma d^2}{\rho \nu Q}. \quad (3.7.2)$$

These three parameters do not depend on the height of the nozzle above the surface. There is therefore a fourth parameter, for example H/d or $H/(\nu^2/g)^{1/3}$, that represents the dimensionless height of fall.

The parameters Π_1 , Π_2 and Π_3 are derived using velocity and radius scales at the nozzle. We have instead used velocity and radius scales at the bottom of the thread, so that the corresponding dimensionless parameters derived directly relate to dynamical balances at the bottom of the thread and thus facilitate the analysis in later chapters. The parameters Π_i are related to the parameters used here by

$$\Pi_1 = \pi^{-3/5} \epsilon^{-6/5} \text{Fr}^{-4/5}, \quad \Pi_2 = \frac{\pi^{1/4}}{2} U_n^{1/2} \epsilon^{-1/2} \quad \text{and} \quad \Pi_3 = \frac{4 \Gamma \epsilon}{\pi U_n}. \quad (3.7.3)$$

CHAPTER 4

THE STEADY MOTION OF A DRAGGED VISCOUS THREAD

4.1 Introduction

The behaviour of a slender viscous thread as it falls onto a moving belt is a problem which has been the subject of recent attention (figure 4.1*a,b*; CWL; R06c; Morris *et al.*, 2007), and which we analyse in this chapter. Experiments have been performed in which a slender thread of a viscous fluid, such as golden syrup, is extruded from a stationary nozzle and then falls through air onto a moving belt. If the belt speed is large, then the thread is simply dragged out to form a catenary-like shape (figure 4.1*a*), but for smaller belt speeds the thread must slow down near the belt. The slowing down of the thread places it under axial compression, which may cause the thread to buckle. However, provided the belt speed is not too low (so that the compression is sufficiently small), the thread forms a steady ‘backward-facing heel’ (figure 4.1*b*), which is stable since the compressive force can be balanced by bending forces within the heel. If the belt speed is sufficiently slow, then the heel is itself unstable to buckling and the motion is unsteady. We analyse the onset of unsteady motion in chapter 5, and in this chapter focus on the steady motion of a dragged thread.

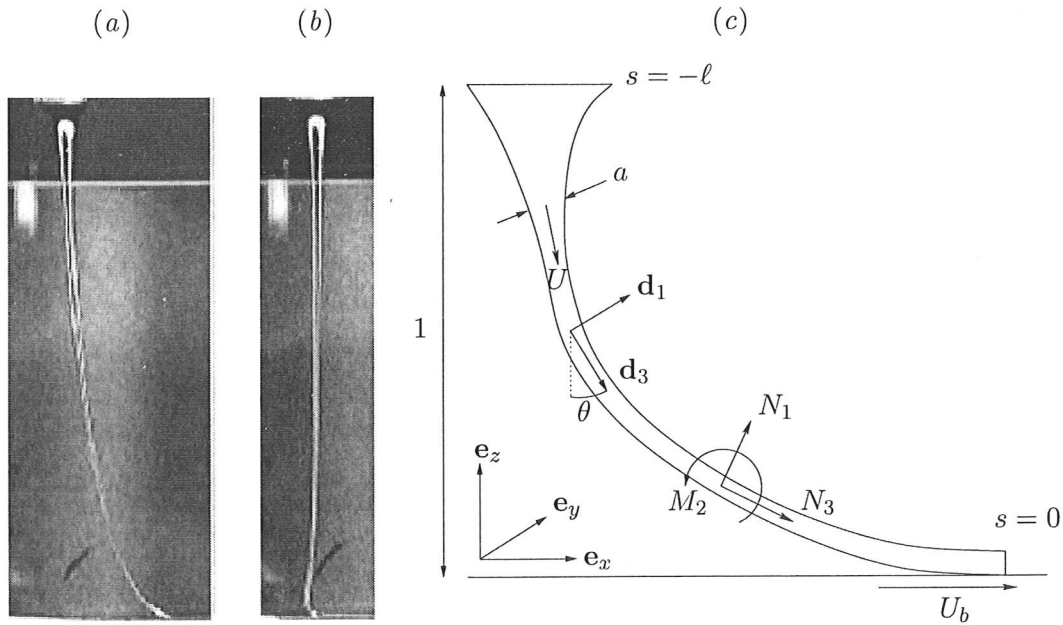


Figure 4.1: (a,b) Experiments performed by CWL, in which a thread of golden syrup falls under gravity onto a belt moving from left to right. (a) For fast belt speeds the thread is dragged out to form a catenary-like shape. (b) For slow belt speeds the thread can buckle and form a steady 'backward-facing heel'. (c) Theoretical definition of the problem (see text).

In order to predict the shape of a steadily dragged thread, a simple theory was derived by CWL. They made the approximation that bending forces are negligible throughout the thread. While a slender thread has only a small bending resistance, so that the bending forces are indeed typically small compared to stretching forces in most of the thread, the complete omission of bending forces neglects their important effects near the contact point with the belt. For example, if the motion is steady then the thread is predicted to turn in a tighter arc than if bending forces were present, which results in an underestimation of the dragout distance. The stretching-dominated solutions also do not allow the thread to undergo compression, and as a consequence do not allow the existence of a steady backward-facing heel.

The stretching-dominated theory was improved by R06c, whose model includes bending forces and which we described in chapter 2. The numerical solution of this model obtains steady shapes that agree very well with those observed experimentally. However, the mathematical model includes many dynamical effects and in the steady problem results in a complicated 9th order two-point boundary-value problem, which makes it a little difficult to extract a more physically based understanding of the solution structure.

The analysis of this chapter concerns the effects of bending stress on a thread where $U_n \ll 1$ and $\epsilon \ll 1$ (see equations 3.2.8a,d), corresponding to a strongly stretched, very slender thread. Particular attention is paid to the influence of bending stresses near

the belt. These bending stresses give rise to singular perturbations to the stretching-dominated theory of CWL and, in consequence, there are boundary layers near the belt and the nozzle within which the bending stresses are dynamically important. This chapter focuses on elucidating the boundary-layer structure and its effects.

In the absence of the belt, the thread would have some free-fall velocity U_f after falling under gravity through a unit height, which we determined in chapter 3. We will see that, as the belt speed U_b varies, the dynamics of the thread falls into one of three distinct regimes. The first, in which $U_b < U_f$, predicts the observed backward-facing heels that could not be explained by the theory of CWL. The regime $U_b > U_f$ gives small corrections to the theory of CWL. The third regime, $U_b \approx U_f$, is distinct and bridges the other two regimes. In each of the above cases, we determine the influence of bending stresses, derive scalings and physical balances within the boundary layer, and find asymptotic approximations that agree well with the full numerical model of R06c.

4.2 Problem description

We consider a viscous thread falling a unit height from a nozzle onto a belt moving horizontally with constant dimensionless speed U_b , as depicted in figure 4.1(c).

We select the Cartesian axes so that the thread lies in the plane $y = 0$, the belt is at $z = 0$ and the nozzle is at $(0, 0, 1)$. The belt moves with velocity $U_b \mathbf{e}_x$ and the gravitational acceleration is $-\mathbf{e}_z$. We select the basis vectors \mathbf{d}_1 and \mathbf{d}_2 so that they rotate with the fluid, which corresponds to setting $\omega_0 = 0$ in (3.2.3). Since the thread is steady, it remains in the $y = 0$ plane and does not twist. Hence we can choose the orientation of the rotating basis so that $\mathbf{d}_2 = -\mathbf{e}_y$ throughout the thread. Then, since \mathbf{d}_3 has been defined to be tangential to the centreline, the basis vector \mathbf{d}_1 is normal to and in the plane of the centreline.

Since the centreline lies in the plane $y = 0$, the orientation of the thread is given by $\theta(s)$, defined as the angle between the centreline and the downward vertical so that $\cos \theta = -\mathbf{d}_3 \cdot \mathbf{e}_z$. The equations that govern the geometry of the centreline may then be obtained by projecting (3.2.1) onto \mathbf{e}_x and \mathbf{e}_z , and (3.2.2) onto \mathbf{d}_2 to obtain

$$x' = \sin \theta \quad (4.2.1)$$

$$z' = -\cos \theta \quad (4.2.2)$$

$$\theta' = \kappa_2. \quad (4.2.3)$$

To simplify the analysis that follows, we initially omit the effects of inertia and surface tension by setting $\text{Fr} = \Gamma = 0$. As we will discuss in §4.8, this approximation does

not significantly change the behaviour of the thread. The nontrivial components of the constitutive relations (3.2.6) and (3.2.7) are then

$$N_3 = 3\pi a^2 U' \quad (4.2.4)$$

$$M_2 = \frac{3\pi a^4}{4} \epsilon^2 (U \kappa_2)', \quad (4.2.5)$$

while the nontrivial components of the force and torque balances (3.2.4) and (3.2.5) are

$$N_1' = -\kappa_2 N_3 + \pi a^2 \sin \theta \quad (4.2.6)$$

$$N_3' = \kappa_2 N_1 - \pi a^2 \cos \theta \quad (4.2.7)$$

$$M_2' = -N_1 - \epsilon^2 \frac{\pi a^4}{4} \kappa_2 \cos \theta. \quad (4.2.8)$$

The form of \mathcal{M} used to obtain the final term in (4.2.8) was derived by R06c.

Kinematic boundary conditions impose the positions of the nozzle and of the contact point, and dynamic boundary conditions impose continuity of flow orientation and of curvature between the thread and the belt or nozzle. These conditions are

$$\theta = \kappa_2 = x = 0, \quad z = 1 \quad \text{and} \quad U = U_n, \quad (4.2.9a-e)$$

at the nozzle, and

$$\theta = \frac{\pi}{2}, \quad \kappa_2 = 0, \quad z = 0 \quad \text{and} \quad U = U_b, \quad (4.2.9f-i)$$

at the belt. The arclength ℓ of the thread is to be determined and so (4.2.9a-e) are applied at an unknown position $s = -\ell$. We have assumed in (4.2.9h) that the thread is sufficiently slender that the distance of the centreline above the belt is negligible at the contact point.

The thread is described by the 8 independent variables $x, z, \theta, \kappa_2, U, N_1, N_3$ and M_2 , with a given by $U^{-1/2}$ by volume conservation. In addition, the length ℓ of the thread is unknown. Hence the 9 boundary conditions (4.2.9) fully determine the solution.

4.2.1 Numerical solution

As mentioned in §2.4, numerical solutions were determined using a continuation method, as implemented by the software package AUTO-07P (Doedel, 2007). We now describe the solution protocol in more detail.

A continuation method requires an initial starting solution. Since it is difficult to obtain a closed-form solution to (4.2.1)–(4.2.9), we initially omit the gravitational terms in (4.2.6)–(4.2.8) by introducing an adjustable parameter c_1 , according to

$$N_1' = -\kappa_2 N_3 + c_1 \pi a^2 \sin \theta \quad (4.2.10)$$

$$N_3' = \kappa_2 N_1 - c_1 \pi a^2 \cos \theta \quad (4.2.11)$$

$$M_2' = -N_1 - c_1 \epsilon^2 \frac{\pi a^4}{4} \kappa_2 \cos \theta, \quad (4.2.12)$$

and where c_1 is initially set to zero. We also relax the boundary conditions (4.2.9*b,g*) by replacing them with

$$\kappa_2 = 1 - c_2 \quad \text{at} \quad s = -\ell \quad \text{and} \quad \kappa_2 = 1 - c_3 \quad \text{at} \quad s = 0, \quad (4.2.13a,b)$$

where c_2 and c_3 are adjustable parameters that are also initially set to zero. After making these modifications, there is a closed-form ‘quarter-circle’ solution, given by

$$x = 1 - \cos \theta, \quad y = 1 - \sin \theta \quad (4.2.14)$$

$$\theta = s, \quad \kappa_2 = 1 \quad \text{and} \quad N_1 = N_3 = M_2 = 0, \quad (4.2.15)$$

with parameter values

$$\ell = \frac{\pi}{2}, \quad \epsilon = 1 \quad \text{and} \quad U_n = U_b = 1. \quad (4.2.16a-d)$$

To obtain a solution to (4.2.1)–(4.2.9), the boundary conditions (4.2.9*b,g*) are first reimposed by using continuation to adjust the parameter values so that $c_2 = 1$ and $c_3 = 1$. The gravitational terms are then reintroduced by adjusting $c_1 = 1$, and the resulting solution satisfies (4.2.1)–(4.2.9) with parameter values given by (4.2.16*b-d*). These parameters are then adjusted to the values desired.

4.3 Asymptotic behaviour of a slender thread

In the limiting case $\epsilon = 0$ of a very slender thread, (4.2.5) and (4.2.8) give $M_2 = N_1 = 0$, corresponding to the negligible resistance of such a thread to bending. In this case, equations (4.2.3)–(4.2.8) reduce to the stretching theory derived by CWL, which is described by

$$N_3 = 3\pi a^2 U' \quad (4.3.1)$$

$$N_3 \theta' = \pi a^2 \sin \theta \quad (4.3.2)$$

$$N_3' = -\pi a^2 \cos \theta, \quad (4.3.3)$$

together with the geometric equations (4.2.1) and (4.2.2). This system no longer involves the derivatives of κ_2 , M_2 and N_1 and so the order of the system has been reduced by three. Consequently the solution does not allow imposition of the boundary conditions that the thread is vertical at the nozzle, and that there is zero curvature at the belt and at the nozzle.

It follows that the finite bending resistance of the thread for $0 < \epsilon \ll 1$ gives rise to a singular perturbation to the stretching-dominated system (4.2.1), (4.2.2) and (4.3.1)–(4.3.3). Hence there are boundary layers at the belt and at the nozzle, across which the curvature and orientation of the thread are corrected to satisfy the relevant boundary conditions. Outside these boundary layers, in a region we have called the ‘tail’, bending stresses are unimportant.

A key parameter for the solution structure is the free-fall speed U_f , defined in chapter 3 as the speed the thread would have after falling in a viscous–buoyancy balance through unit height in the absence of the belt. We will demonstrate that, depending on the relative sizes of the belt speed U_b and U_f , the tail either falls vertically, or is deflected to form a catenary. In either case the tail is governed by (4.3.1)–(4.3.3), with $\theta = 0$ if the thread is vertical.

4.3.1 Boundary-layer structure

In the remainder of this chapter we determine the singular perturbations to the stretching theory arising from the finite bending resistance of a slender thread. A preliminary simplification is to note that the $O(\epsilon^2)$ gravitational contribution to the moment balance (4.2.8) is only a small regular perturbation as $\epsilon \rightarrow 0$, and can be omitted.

The bending stresses in the thread decrease as $\epsilon \rightarrow 0$, but not uniformly, and they remain dynamically important in boundary-layer regions of decreasing length near the belt and nozzle. We focus attention on the boundary layer near the belt. The tail is governed by (4.3.1)–(4.3.3), and is therefore independent of ϵ at leading order. Hence the axial stress, velocity and dimensionless radius at the base of the thread are independent of ϵ , and therefore remain $O(1)$ as $\epsilon \rightarrow 0$. The constitutive relation (4.2.4) then implies that U cannot vary significantly over the short lengthscale of the boundary layer. The necessary adjustment of the thread velocity from its free-fall speed U_f to the belt speed U_b must therefore take place within the tail. Hence we can assume that $U = U_b$ at leading order throughout the boundary layer at the belt.

Since the velocity is constant throughout the boundary layer at leading order, the constitutive relation (4.2.5) may be simplified using $a^2U = 1$ to obtain

$$M_2 = \frac{3\pi a_b^2}{4} \epsilon^2 \kappa_2'. \quad (4.3.4)$$

We combine (4.3.4) with (4.2.6)–(4.2.8) to obtain the simplified dynamic equations

$$N_1 = -\frac{3\pi a_b^2}{4}\epsilon^2\theta''' \quad (4.3.5)$$

$$N_1' = -\kappa_2 N_3 + \pi a_b^2 \sin \theta \quad (4.3.6)$$

$$N_3' = \kappa_2 N_1 - \pi a_b^2 \cos \theta, \quad (4.3.7)$$

where $a_b^2 = 1/U_b$. This is a fifth-order system, but we note that the force balances (4.3.6) and (4.3.7) have first integrals F_x and F_z , which are the horizontal and vertical forces exerted by the belt, given by

$$F_x = N_3 \sin \theta + N_1 \cos \theta \quad \text{and} \quad F_z = N_1 \sin \theta - N_3 \cos \theta - \pi a_b^2 s. \quad (4.3.8a,b)$$

Hence (4.3.5)–(4.3.8) may be recast as a third-order system,

$$\epsilon^2\theta''' = -\frac{4}{3\pi a_b^2} N_1 \quad (4.3.9)$$

$$N_1 = F_x \cos \theta + F_z \sin \theta + \pi a_b^2 s \sin \theta, \quad (4.3.10)$$

where F_z and F_x are as yet unknown but are determined by matching towards the behaviour of the tail. The axial stress N_3 is

$$N_3 = F_x \sin \theta - F_z \cos \theta - \pi a_b^2 s \cos \theta. \quad (4.3.11)$$

The qualitative nature of the boundary-layer corrections depends on the relative sizes of the free-fall speed U_f and the belt speed U_b . The variation of the velocity in the tail requires a force to be exerted through the boundary layer. If $U_b < U_f$, the boundary layer exerts a vertical force F_z on the thread which reduces the stretching and slows down the tail above it. The thread remains nearly vertical outside the boundary layer, and the axial velocity profile within this vertical tail has been derived in chapter 3. If $U_b > U_f$, the boundary layer exerts a horizontal force F_x on the tail, which increases the stretching and hence also the thread speed. The thread is deflected sideways and the axial velocity variation within the tail is given approximately by the theory of CWL. There is also an intermediate regime, where $U_b \approx U_f$, in which the force exerted through the boundary layer has components of similar size in the x and z directions.

Within each regime, there are distinct dynamical balances in the boundary layer. We will introduce scaled variables

$$\eta = \frac{s}{\delta_*} \quad \text{and} \quad n_i = \frac{N_i}{F_*}, \quad (4.3.12a,b)$$

where δ_* and F_* are the length and force scales relevant to the regime under consideration.

4.4 Compressional heel: $U_b < U_f$

We first deal with the case in which the belt speed U_b is slower than the free-fall velocity U_f . The necessary deceleration within the tail places the lower part of it under compression. The role of bending stresses within the boundary layer at the belt is to support this compression, and to divert the thread from $\theta \approx 0$ in the tail to $\theta = \pi/2$ at the belt.

The analysis of §3.4.1 implies that the compressive force F_z required to decelerate the tail is independent of ϵ , and hence $O(1)$ as $\epsilon \rightarrow 0$. The force balance (4.3.8b) implies that the contribution of the gravitational stress to F_z within the boundary layer is $O(\delta_z)$, where δ_z is the lengthscale of the boundary layer, and thus negligible as $\epsilon \rightarrow 0$. Further, we anticipate that both $N_1 \rightarrow 0$ and $\theta \rightarrow 0$ in the tail and so (4.3.8a) motivates the further assumption that $F_z \gg F_x$. Hence $N_1 \sim N_3 \sim F_z$ within the boundary layer. The change in θ from 0 to $\pi/2$ across the boundary layer implies that the curvature $\kappa_2 = \theta' \sim \delta_z^{-1}$. We substitute these scalings into the stress-moment equation (4.3.9) to obtain

$$\delta_z = \left(\frac{3\pi a_b^2 \epsilon^2}{4F_z} \right)^{1/3}. \quad (4.4.1)$$

We note that δ_z is $O(\epsilon^{2/3})$, and hence the neglect in (4.2.9h) of the $O(\epsilon)$ correction from the radius of the thread at the contact point is justified in the asymptotic limit $\epsilon \ll 1$.

Using F_z and δ_z to define the rescaling (4.3.12), we find that the bending stress (4.3.10) is given at leading order by

$$n_1 = \sin \theta. \quad (4.4.2)$$

The rescaled shape $\theta(\eta)$ of the thread is then obtained by substitution into (4.3.9) to obtain

$$\theta''' + \sin \theta = 0. \quad (4.4.3)$$

The boundary conditions at the belt are

$$\theta = \frac{\pi}{2} \quad \text{and} \quad \theta' = 0 \quad \text{at} \quad \eta = 0. \quad (4.4.4)$$

A third condition is required to match to a vertical tail and enforce the decay of bending stress. We anticipate that $\theta \approx 0$, and linearisation about this value implies that

$$\theta \sim \sum_{i=1,2,3} A_i \exp(\lambda_i \eta) \quad \text{as} \quad \eta \rightarrow -\infty, \quad (4.4.5)$$

where $\lambda_i^3 = -1$ and A_i are complex amplitudes of the three modes. Two of these modes decay exponentially as $\eta \rightarrow -\infty$ as desired, but the mode with $\lambda_i = -1$ diverges. Thus

suppression of this divergent mode by imposing

$$\theta \rightarrow 0 \quad \text{as} \quad \eta \rightarrow -\infty \quad (4.4.6)$$

gives the third condition. The exponential decay of θ as $\eta \rightarrow -\infty$ means that the tail has both a negligible deflection from the vertical and negligible bending stress.

Equation (4.3.11) implies that $n_3 = -\cos\theta$ at leading order, and so (4.4.6) implies $n_3 \rightarrow -1$ as $\eta \rightarrow -\infty$, which is consistent with matching onto a vertical tail with a vertical compression F_z .

There is a unique solution to (4.4.3), (4.4.4) and (4.4.6). The scaled shape at the base of a slender dragged thread is therefore universal as $\epsilon \rightarrow 0$ when $U_b < U_f$. A variation of experimental parameters results in a simple rescaling of the size of the boundary layer according to the definition of δ_z in (4.4.1).

Figure 4.2 shows the shape of the universal solution, which we call the 'compressional' heel. We note that it has a backward-facing heel, which matches the observed behaviour of steadily dragged threads for slower belt speeds (cf figure 4.1*b*). Above the backward-facing heel there are exponentially damped oscillations about the vertical in agreement with (4.4.5), though these oscillations would be too small to be seen experimentally. Figure 4.3 shows that as $\epsilon \rightarrow 0$, the solutions to the full set of bending equations (4.2.3)–(4.2.8) converge towards the asymptotic solution given by (4.4.3), (4.4.4) and (4.4.6). Values of ϵ representative of experiment are shown in table 3.1, and range between 4×10^{-5} and 4×10^{-2} . There is very close agreement between the full and asymptotic solutions in this range. The full solutions are known to agree well with experiment (R06c), and hence the asymptotic solutions give good quantitative predictions for the observed heel shapes.

The gravitational term that was omitted from the force balance (4.3.10) is $O(\pi a_b^2 \delta_z / F_z)$ relative to the bending terms. Equation (4.4.1) implies that this omission is consistent provided

$$\left(\frac{3\pi a_b^2 \epsilon^2}{4F_z} \right)^{1/3} \ll \frac{F_z}{\pi a_b^2}. \quad (4.4.7)$$

If U_b is fixed then a_b and F_z are $O(1)$ as $\epsilon \rightarrow 0$ and (4.4.7) holds when $U_b < U_f$ and ϵ is sufficiently small.

4.5 Gravitational heels: $U_b \approx U_f$

If $U_b \approx U_f$ then the thread undergoes only a small amount of compression relative to free-fall and F_z is small. Hence (4.4.7) breaks down when $U_b \rightarrow U_f$ with ϵ fixed, however small. This limit leads to a new regime in which gravity is also important near the belt.

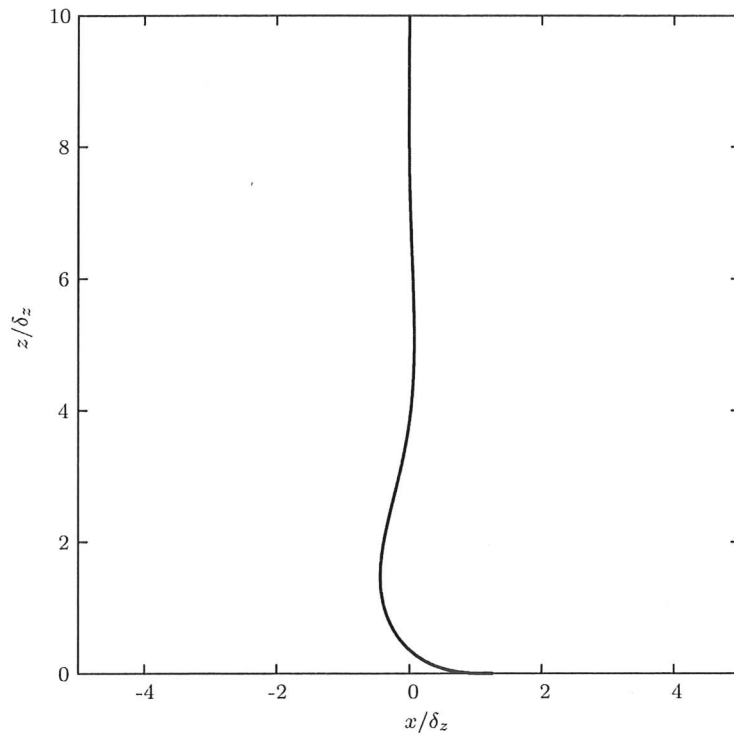


Figure 4.2: The shape of the compressional-heel solution to (4.4.3), (4.4.4) and (4.4.6).

We consider a distinguished double limit $\epsilon \rightarrow 0$ and $U_b \rightarrow U_f$ in which gravitational stresses are in balance with compressional and bending stresses throughout the boundary layer. The force balance (4.3.10) implies that the relevant force scale is $F_g \sim \pi a_b^2 \delta_g$, where δ_g is the corresponding lengthscale. The small stresses within the boundary layer cause only a small deflection of the tail from vertical. Hence the boundary layer must again deflect the thread from $\theta \approx 0$ in the tail to $\theta = \pi/2$ at the belt, and the curvature κ_2 within the boundary layer again scales like $\theta' \sim \delta_g^{-1}$. We substitute these scalings into the stress-moment balance (4.3.9) to obtain

$$\delta_g = \left(\frac{3\epsilon^2}{4} \right)^{1/4}. \quad (4.5.1)$$

(We note that this scaling coincides with that found by R04 in the ‘gravitational regime’ of the related problem of steady fluid coiling on a stationary surface.)

Using F_g and δ_g to define the rescaling (4.3.12), we rewrite (4.3.9) and (4.3.10) as

$$\theta''' = -\phi_z \sin \theta - \phi_x \cos \theta - \eta \sin \theta, \quad (4.5.2)$$

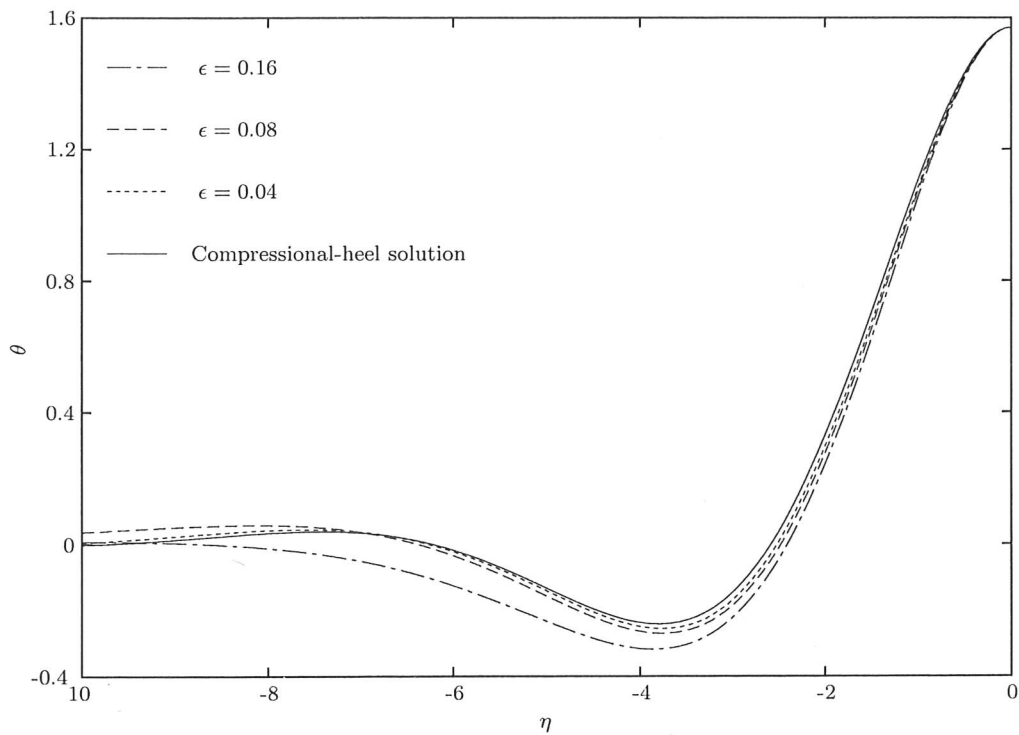


Figure 4.3: The numerical solution to the full system (4.2.3)–(4.2.8) of bending equations approaches the compressional heel as ϵ decreases. Here $U_b = 0.25U_f$, and $\epsilon \leq 0.04$ is representative of experimental values.

where ϕ_x and ϕ_z are constants given by

$$\phi_x = \frac{F_x}{F_g} \quad \text{and} \quad \phi_z = \frac{F_z}{F_g}. \quad (4.5.3a,b)$$

The boundary conditions $\theta = \pi/2$, $\theta' = 0$ again apply at the belt. Equation (4.5.2) links the values of ϕ_x and ϕ_z to the shape $\theta(\eta)$ of the thread near the belt. Hence, in contrast to the compressional heel, the values of ϕ_x and ϕ_z depend on the behaviour of the heel, and cannot be directly determined from consideration of the tail alone. As before, matching conditions are required to enforce the decay of θ and of bending stress into the tail. We again anticipate that $\theta \rightarrow 0$ as $\eta \rightarrow -\infty$, and linearise (4.5.2) about this value to obtain

$$\theta''' \sim -\phi_z \theta - \phi_x - \eta \theta. \quad (4.5.4)$$

The solution approaches

$$\theta \sim -\frac{\phi_x}{\eta} + \sum_{i=1,2,3} A_i \exp\left(-\frac{3}{4}\lambda_i \eta^{4/3}\right) \quad \text{as} \quad \eta \rightarrow -\infty, \quad (4.5.5)$$

where $\lambda_i^3 = -1$, the first term on the right hand side is a leading-order particular integral and the exponential modes are WKBJ approximations to the complementary function (neglecting an algebraic factor in the amplitude for simplicity). The third-order equation (4.5.2) contains two free constants and is subject to two boundary conditions (4.4.4) at the belt and two matching conditions to suppress the two divergent exponential modes in (4.5.5). Hence there is a one-parameter family of solutions, which we call 'gravitational heels'.

The value of the remaining parameter is determined by matching the vertical force between the heel and the tail. After rescaling, the vertical force balance (4.3.8b) is

$$n_1 \sin \theta - n_3 \cos \theta = \phi_z + \eta. \quad (4.5.6)$$

Since the deflection of the tail from vertical is very small, the rescaled vertical coordinate $Z = z/\delta_g$ approaches $-\eta - \Delta\eta$ as $\eta \rightarrow -\infty$, where the offset $\Delta\eta$ is the extra arclength due to the curvature of the heel. Hence, as $\eta \rightarrow -\infty$ and $\theta \rightarrow 0$, the force balance (4.5.6) approaches

$$n_3 = Z - \Phi_z, \quad (4.5.7)$$

where the parameter

$$\Phi_z = \phi_z - \Delta\eta \quad (4.5.8)$$

is the effective vertical force exerted by the heel on the tail, given by the upward force from the belt less the extra weight in the heel. By matching to a vertical tail and substituting

(4.3.1) and $F_g = \pi a_b^2 \delta_g$ into (4.5.3b), we can determine Φ_z from the condition

$$\Phi_z = \frac{3}{\delta_g} \frac{dU}{dz} \quad \text{at } z = 0, \quad (4.5.9)$$

where $U(z)$ is the extensional velocity profile in the tail. This profile has been determined, for small values of F_z , in chapter 3 where we also found that (4.5.9) gives

$$\Phi_z = \frac{3\pi^2}{4\delta_g} (U_f - U_b) + O\left(\frac{(U_f - U_b)^2}{\delta_g}\right), \quad (4.5.10)$$

thus relating the force Φ_z to the velocity difference $U_f - U_b$ that it must produce.

Since Φ_z is determined by the tail, we use it to parametrise the family of heels, with the value of ϕ_x then being a consequence of the solution. Equation (4.5.5) implies that the growing exponential modes can be suppressed by imposing

$$\theta \sim -\frac{\phi_x}{\eta} \quad \text{and} \quad \kappa_2 \sim \frac{\phi_x}{\eta^2} \quad \text{as } \eta \rightarrow -\infty. \quad (4.5.11)$$

We remark that (4.5.11) is also satisfied by a tail that is governed by rescaled versions of (4.3.1)–(4.3.3) and deflected by a horizontal force ϕ_x . Hence (4.5.11) matches the horizontal force and deflection between the heel and the tail.

Figure 4.4 shows some thread shapes for various values of Φ_z , and figure 4.5 shows the dependence of ϕ_x on Φ_z . As Φ_z increases, the horizontal force ϕ_x tends to zero and the deflection of the tail from vertical thus also becomes small. For large values of Φ_z the thread shapes are similar to that of the compressional heel. This is because large values of Φ_z correspond to strong compression of the boundary layer, so that gravitational forces are negligible in comparison, $\Delta\eta \ll \phi_z$ and $\Phi_z \approx \phi_z$. A comparison of the lengthscales (4.4.1) and (4.5.1), together with (4.5.3b), shows that when $\Phi_z \gg 1$ the lengthscale of the gravitational heel is given by

$$\delta_g = \Phi_z^{1/3} \delta_z. \quad (4.5.12)$$

Figure 4.6 shows the convergence of the rescaled gravitational-heel solutions towards the compressional-heel solution in the limit $\Phi_z \rightarrow \infty$.

In the opposite limit, $\Phi_z \rightarrow -\infty$, figure 4.5 shows that bending stresses within the gravitational heel exert a large horizontal force ϕ_x on the tail. The deflection of the tail is therefore large and the shape of the thread (figure 4.4) increasingly resembles the stretched catenaries found by CWL. This suggests that there is a third boundary-layer regime that we have not yet considered, which we anticipate applies when $U_b > U_f$.

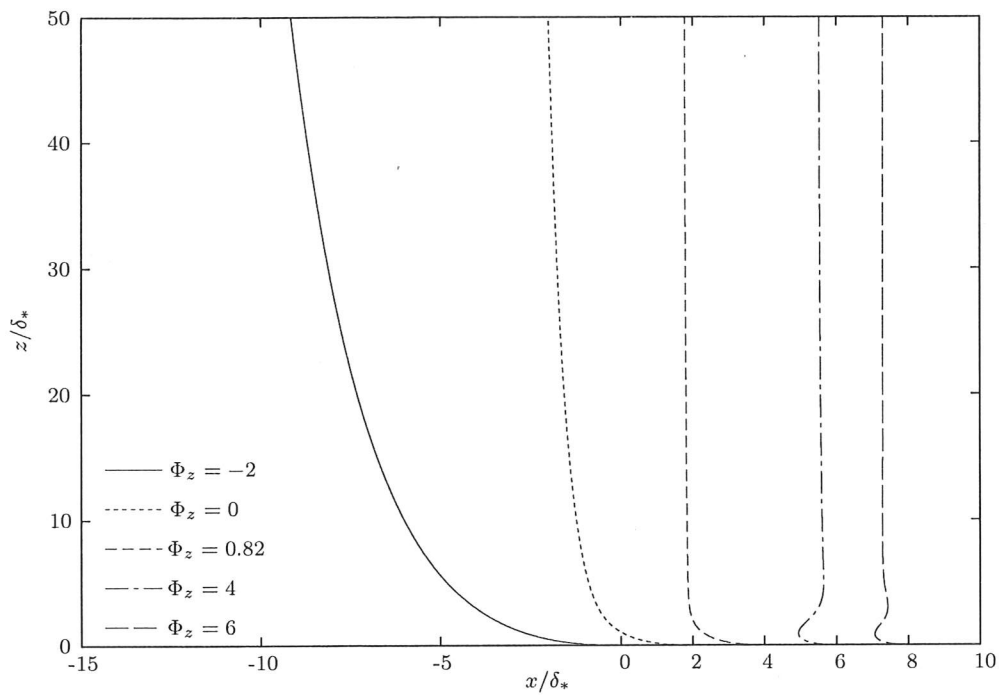


Figure 4.4: A plot of heels within the gravitational regime, for various values of the effective vertical force Φ_z on the tail. The contact points are offset at multiples of 2 on the x axis.

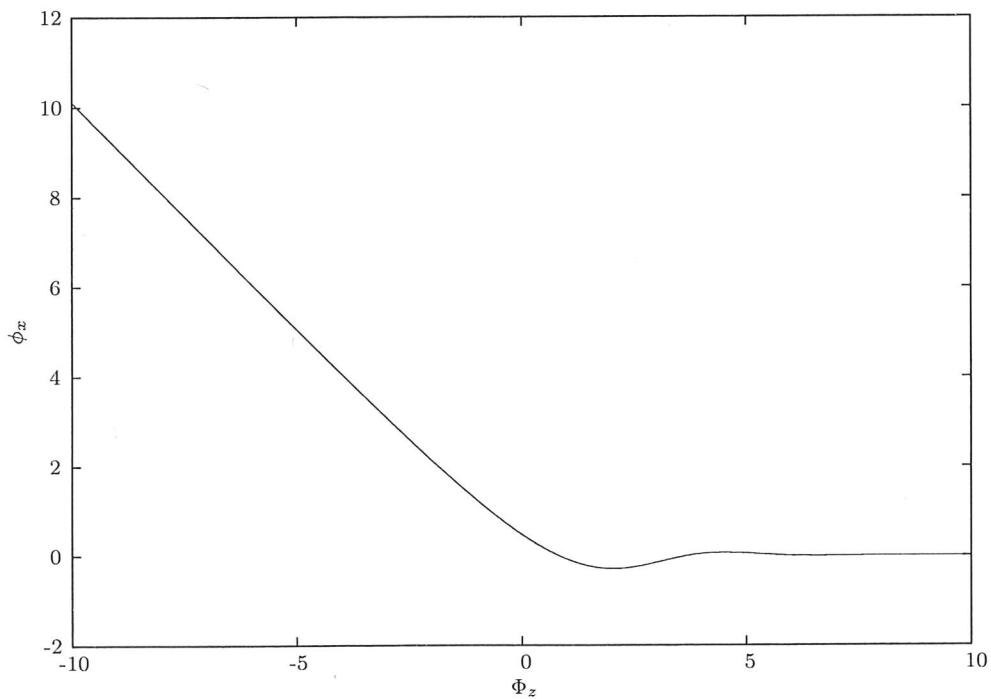


Figure 4.5: The dependence of the rescaled horizontal force ϕ_x on Φ_z .

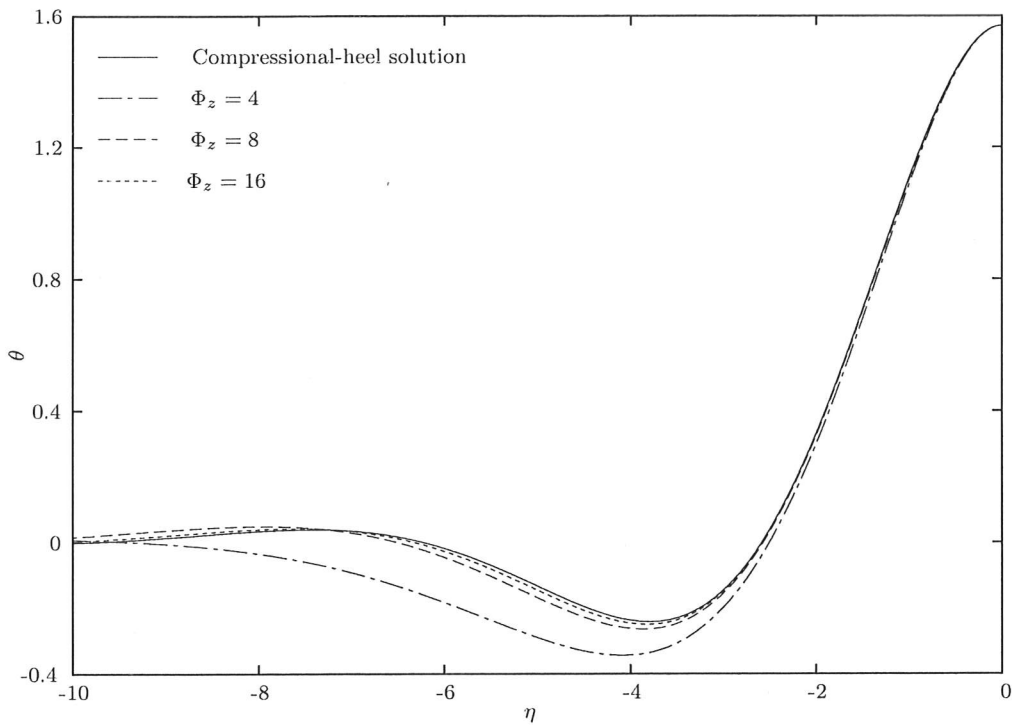


Figure 4.6: The rescaled solutions in the gravitational regime approach the compressional-heel solution as $\Phi_z \rightarrow \infty$.

4.6 Curvature-adjustment layer: $U_b > U_f$

CWL developed a theory for $U_b > U_f$ that neglects bending stresses. While their equations allow the thread to be horizontal at the belt, they also imply that the curvature at the belt κ_b is non-zero. The role of bending stresses when $U_b > U_f$ is to adjust the curvature from κ_b to zero across the boundary layer, thus allowing all the dynamic boundary conditions to be satisfied. Outside this boundary layer, bending stresses are unimportant and the tail behaves like the stretching-dominated solution of CWL. At the base of the tail, where $\theta \approx \pi/2$, the horizontal force balance (4.3.8a) implies that $N_3 \approx F_x$. Hence (4.3.2) implies that the curvature κ_b at the base of the tail is

$$\kappa_b = \frac{\pi a_b^2}{F_x}. \quad (4.6.1)$$

In contrast to the previous two regimes, the tail is nearly horizontal near the base, and θ does not vary significantly across the boundary layer. Hence the curvature scaling is not given by an $O(1)$ variation in θ over an $O(\delta_*)$ lengthscale, but by κ_b .

We aim to find the curvature κ_2 within the boundary layer. We combine (4.3.6) and

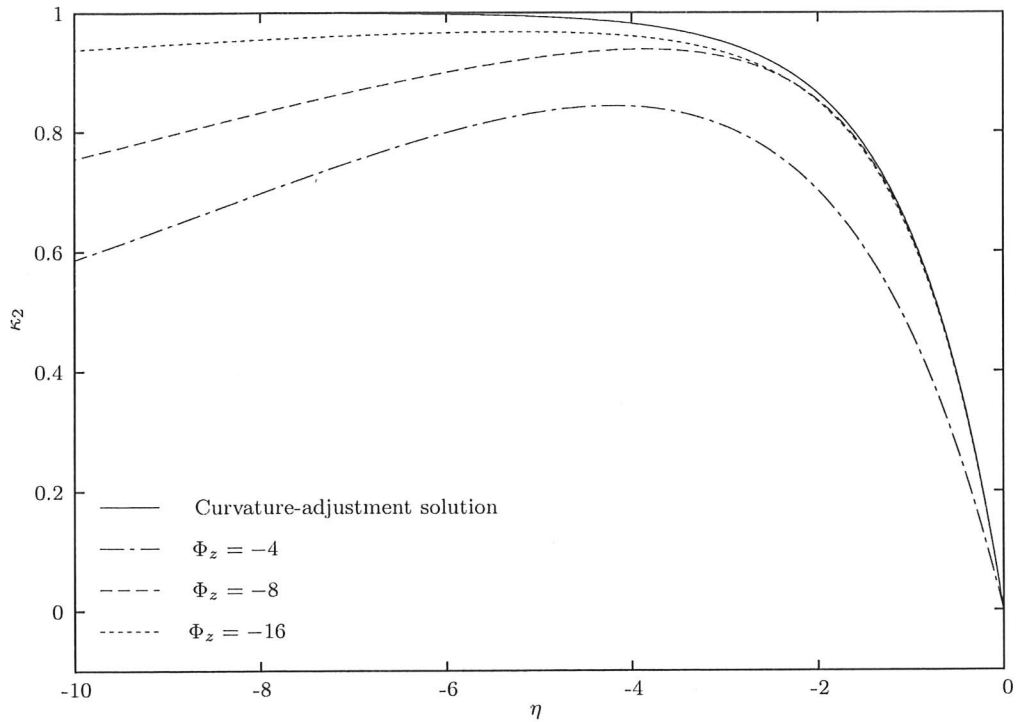


Figure 4.7: The rescaled solutions in the gravitational regime approach the curvature-adjustment solution as $\Phi_z \rightarrow -\infty$.

(4.3.9) with $N_3 = F_x$ and $\theta' = \kappa_2$ to obtain

$$\kappa_2 - \frac{3\pi a_b^2 \epsilon^2}{4F_x} \kappa_2''' = \kappa_b. \quad (4.6.2)$$

Thus the arclength of the boundary layer scales like

$$\delta_x \sim \left(\frac{3\pi a_b^2 \epsilon^2}{4F_x} \right)^{1/3} \quad (4.6.3)$$

and, using this to define the rescaling (4.3.12a), we rewrite (4.6.2) as

$$\kappa_2 - \kappa_2''' = \kappa_b. \quad (4.6.4)$$

The general solution of (4.6.4) is

$$\kappa_2 \sim \kappa_b + \sum_{i=1,2,3} A_i \exp(-\lambda_i \eta), \quad (4.6.5)$$

where $\lambda_i^3 = -1$. The matching condition $\kappa_2 \rightarrow \kappa_b$ as $\eta \rightarrow -\infty$ suppresses the two divergent modes in (4.6.5) and, together with the boundary condition $\kappa_2 = 0$ at $\eta = 0$, defines a

unique solution

$$\kappa_2 = \kappa_b (1 - e^\eta), \quad (4.6.6)$$

which we call a 'curvature-adjustment layer'. This solution, like the compressional heel, is universal and qualitatively unchanged by variation of experimental parameters.

The variation of θ across the boundary layer is $O(\kappa_b \delta_x)$. From (4.6.1) and (4.6.3), the assumption that $\theta \approx \pi/2$ throughout the boundary layer is consistent with this variation provided that

$$\left(\frac{3\pi a_b^2 \epsilon^2}{4F_x} \right)^{1/3} \ll \frac{F_x}{\pi a_b^2}. \quad (4.6.7)$$

Hence if $U_b > U_f$ is fixed then F_x and a_b are fixed and (4.6.7) holds when ϵ is sufficiently small.

If U_b is close to U_f then there is only a small amount of stretching in the tail and F_x is small. Hence (4.6.7) breaks down when $U_b \rightarrow U_f$ with ϵ fixed, however small. The gravitational heels, which do not make the approximation $\theta \approx \pi/2$ throughout the boundary layer near the belt, are applicable in this limit.

The thread shapes for $\Phi_z < 0$ in figure 4.4 suggest that the gravitational heels converge towards a curvature-adjustment layer with a dragged tail as $\Phi_z \rightarrow -\infty$, and hence as $\phi_x \rightarrow \infty$. This convergence may be seen quantitatively by rescaling (4.6.6) with respect to the gravitational scales F_g and δ_g , to obtain

$$\delta_g \kappa_2 = \phi_x^{-1} (1 - e^{K\eta_g}), \quad (4.6.8)$$

where

$$\delta_g = \phi_x^{1/3} \delta_x \quad \text{and} \quad K = \phi_x^{1/3}. \quad (4.6.9)$$

The convergence of gravitational heels towards this solution is shown in figure 4.7.

We conclude that the gravitational heels match smoothly between the compressional heel, valid for fixed $U_b < U_f$ as $\epsilon \rightarrow 0$, and the curvature-adjustment solution, valid for fixed $U_b > U_f$ as $\epsilon \rightarrow 0$.

4.6.1 Perturbation to the tail

The shape of the thread near the belt is found by integrating $z'' = \kappa_2$ using (4.6.6) subject to $z = z' = 0$ at the contact point. We obtain

$$z = \kappa_b \left(\frac{1}{2}(\eta + 1)^2 + \frac{1}{2} - e^\eta \right), \quad (4.6.10)$$

which approaches

$$z \sim \frac{\kappa_b}{2}(\eta + 1)^2 \quad \text{as } \eta \rightarrow -\infty. \quad (4.6.11)$$

If the existence of the boundary layer is neglected then extrapolation of (4.6.11) to $z = 0$ gives contact at $\eta = -1$ rather than $\eta = 0$; hence the boundary layer provides an additional arclength of δ_x . Since the thread continues stretching at a rate $U' = F_x/3\pi a_b^2$ between $\eta = -1$ and $\eta = 0$, it follows that the effective boundary condition on the catenary solution in the tail is not $U = U_b$ at $z = 0$, but instead $U = U_b - \Delta U$ where

$$\Delta U = \frac{F_x \delta_x}{3\pi a_b^2}. \quad (4.6.12)$$

Together with (4.6.3), this implies that bending-stress corrections at the belt cause an $O(\epsilon^{2/3})$ global perturbation to the tail which dominates the $O(\epsilon^2)$ perturbations caused by the local bending stresses. This global perturbation makes a significant contribution to the dragout distance as described in §4.7.

4.6.2 Boundary layer at the nozzle

Bending stresses are important near the nozzle in addition to near the belt. At the nozzle, bending stresses modify the shape of the thread so that the thread is both vertical and free of curvature at the nozzle. However, since the horizontal deflection and curvature in the tail are small for both the compressional and gravitational heels, the boundary layer at the nozzle has no effect on the thread at leading order. If the horizontal force F_x is $O(1)$, then the stretching-dominated tail approaches the nozzle at a non-zero angle θ_n that is also $O(1)$ as $\epsilon \rightarrow 0$.

In contrast to the $O(1)$ horizontal force near the nozzle, the gravitational stresses in the boundary layer at the nozzle are $O(\delta_*)$ and thus negligible as $\epsilon \rightarrow 0$. Hence the analysis proceeds similarly to that of the compressional heel in §4.4, except with δ_* given by

$$\delta_n = \left(\frac{3\pi a_n^2 \epsilon^2}{4F_n} \right)^{1/3}, \quad (4.6.13)$$

where F_n is the axial tension at the nozzle. The shape of the thread near the nozzle is governed (without rescaling) by

$$\delta_n^3 \theta''' - \sin(\theta - \theta_n) = 0, \quad (4.6.14)$$

with boundary conditions

$$\theta = \theta' = 0 \quad \text{at } s = -\ell \quad \text{and} \quad \theta \rightarrow \theta_n \quad \text{as} \quad \frac{s + \ell}{\delta_n} \rightarrow \infty. \quad (4.6.15a-c)$$

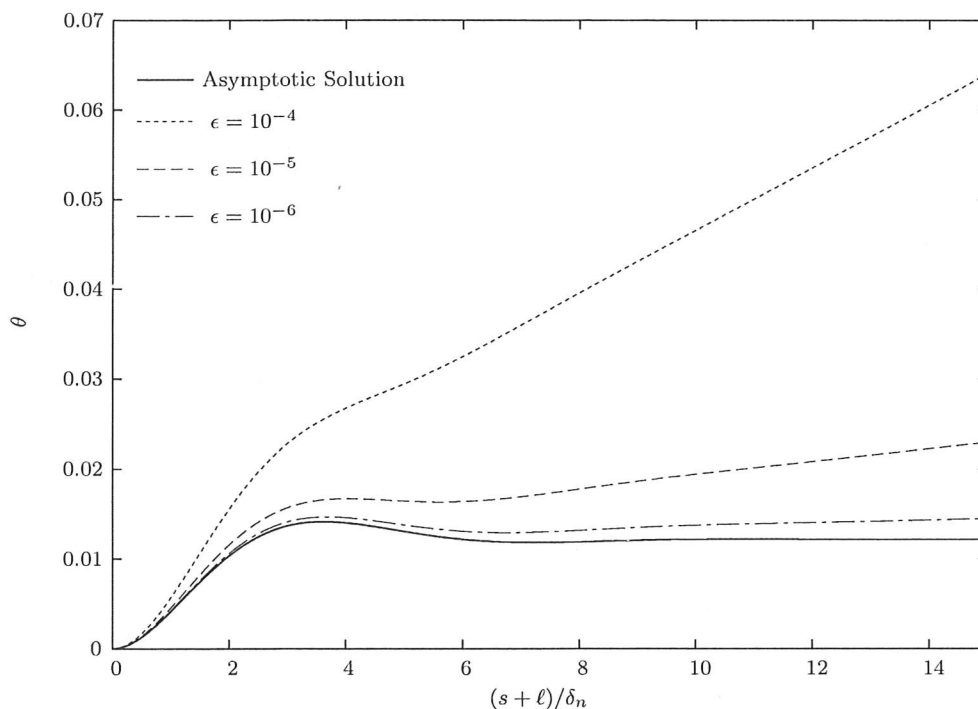


Figure 4.8: The solution to the full system (4.2.3)–(4.2.8) of bending equations approaches the asymptotic boundary-layer solution at the nozzle as ϵ decreases. Here $U_n = 10^{-4}$ and $U_b = 0.15 \approx 2U_f$.

Linearisation of (4.6.14) about $\theta = \theta_n$ shows that the matching condition $\theta \rightarrow \theta_n$ as $(s + \ell)/\delta_n \rightarrow \infty$ suppresses one exponential mode and, together with (4.6.15a,b), gives rise to a unique solution for each θ_n . We note that there is one more boundary condition and one less matching condition than for the curvature-adjustment layer. This is due to the difference in direction between $(s + \ell)/\delta_n \rightarrow \infty$ and $s/\delta_x \rightarrow -\infty$ which requires different modes to be suppressed in order to match to the tail.

Figure 4.8 shows that the solutions to the full set of bending equations (4.2.3)–(4.2.8) converge towards the asymptotic solution given by (4.6.14) and (4.6.15). We note that the convergence as ϵ decreases is far slower than for the boundary layer at the belt. The reason for this is that, since $U_n \ll 1$, the thread radius at the nozzle satisfies $a_n \gg 1$. It follows that while it is asymptotically correct to neglect the gravitational terms as $\epsilon \rightarrow 0$, they are numerically significant at the nozzle for the parameter values used.

In a similar way to the boundary layer at the belt, the bending-stress corrections at the nozzle cause an $O(\epsilon^{2/3})$ global perturbation to the tail in addition to a local $O(\epsilon^{2/3})$ perturbation to the shape of the thread at the nozzle. The size of the bending-stress correction at the nozzle is formally of the same order as that at the belt as $\epsilon \rightarrow 0$. However, when we estimate the dragout distance of the thread in §4.7, the numerical value of the

correction at the nozzle is numerically much smaller than the correction at the belt. This might be anticipated on the grounds that the deflection of the stretching-dominated thread from vertical is small ($\theta \lesssim 10^{-2}$ for $U_b \leq 2U_f$) at the nozzle since the horizontal stress exerted by the belt is much smaller than the gravitational stress there. From (4.3.2), it follows that the curvature θ' near the nozzle is also small. The bending-stress corrections required to satisfy (4.2.9*a,b*) at the nozzle are therefore much smaller than those at the belt, and for simplicity we will omit the bending-stress corrections at the nozzle when estimating the dragout distance of the thread in the following section.

4.7 Dragout distance of asymptotic solutions and full numerical solutions

We now use the asymptotic solutions found in the preceding sections to estimate the dimensionless dragout distance x_b , defined as the horizontal displacement from the nozzle to the contact point with the belt. We consider separately the contributions to x_b that arise from the deflection of the tail from vertical and from the shape of the boundary layer at the belt. The boundary layer exerts a horizontal force F_x on the tail that deflects it from vertical. Due to this force, the tail forms a catenary that hangs from the nozzle under gravity. We define x_t to be the horizontal displacement between the nozzle and the minimum of this catenary extrapolated as if the boundary layer were not there. The curvature of the boundary layer modifies the shape of the thread near the belt from that of the tail. We define x_ℓ to be the distance between the minimum of the extrapolated catenary and the contact point with the belt. The contributions x_t and x_ℓ to x_b are illustrated in figure 4.9(*a*). Clearly $x_b = x_t + x_\ell$.

The compressional heel matches to a tail that has negligible deflection from vertical and hence has $x_t \approx 0$. The contribution x_ℓ to the dragout distance of the compressional heel is found by numerical integration of (4.4.3) together with (4.2.1) to be $1.26\delta_z$.

The gravitational heel matches to a tail with a deflection that is governed by the horizontal force $F_x = O(\epsilon^{1/2})$ exerted by the boundary layer near the belt. As described in §3.4.2, we may approximate the tail as a uniform catenary of weight πa_b^2 per unit length. This gives the leading-order estimate

$$x_t = \frac{F_x}{\pi a_b^2} \ln \left(\frac{\ell}{F_x} \right) + O(F_x), \quad (4.7.1)$$

where the arclength of the thread is $\ell = 1 + O(\epsilon^{1/2})$. The variation of thread radius towards the nozzle gives only an $O(F_x)$ contribution to x_t and so has no effect at leading

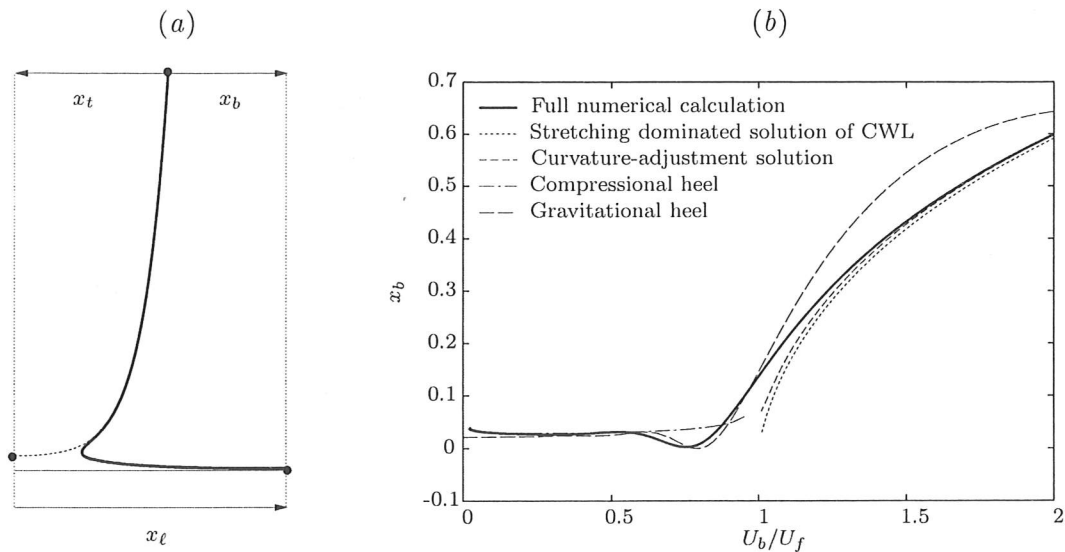


Figure 4.9: (a) The contributions to dragout distance from the heel and from the stretching-dominated tail. The contribution x_t from the tail is measured horizontally from the base of the extrapolated catenary (dashed) to the height of the nozzle, and x_ℓ is the offset from the catenary arising from the curvature of the heel (solid). (b) Asymptotic estimates of the dragout distance for various belt speeds compared to the values calculated using the full system of bending equations (4.2.3)–(4.2.8), for parameter values $\epsilon = 4 \times 10^{-2}$, $U_n = 7 \times 10^{-3}$.

order. The additional offset x_ℓ is found by numerical integration of (4.5.2) and depends only on Φ_z and δ_g .

The curvature-adjustment layer matches towards a tail with a displacement x_t that is governed by the estimate of CWL, but with the velocity condition at the base modified to $U_b - \Delta U$ as described by (4.6.12). Since $\theta \approx \pi/2$ throughout the curvature-adjustment layer, its contribution x_ℓ is the additional arclength within the bending boundary layer, which was shown in §4.6.1 to be δ_x .

Figure 4.9(b) plots the various asymptotic estimates of x_b and compares them to the full numerical solution. The parameter values used are $\epsilon = 4 \times 10^{-2}$ and $U_n = 7 \times 10^{-3}$, which are typical of the experiments performed by CWL and Morris *et al.* (2007).

4.8 Discussion

In this chapter we have demonstrated the importance of the bending resistance of a steadily dragged viscous thread to its motion. An asymptotic analysis for a very slender thread has determined the leading-order dynamic effects of bending stress. We have shown that there are three distinct regimes for the shape of the thread, corresponding to the belt speed being less than, greater than or close to the ‘free-fall’ speed of the thread. The smooth transition between regimes shows that the solutions cover the full range of steady shapes.

The estimates for the dragout distance x_b of the thread, derived from the compressional heel and the curvature-adjustment layer, give good agreement for small and large belt speeds respectively. As anticipated, both estimates break down when U_b is close to U_f . The estimate for x_b derived from the gravitational heels give good agreement for $U_b \approx U_f$. It is perhaps surprising that the estimate also works well for values of U_b somewhat smaller than U_f , despite the $O((U_b - U_f)^2/\delta_g)$ error that is introduced when (4.5.10) is used to estimate Φ_z . The reason is that x_t is negligible for $U_b < U_f$ and x_ℓ is approximately the offset of a compressional heel, which can be written as $1.26\Phi_z^{-1/3}\delta_g$ using (4.5.12). This depends only weakly on Φ_z .

The estimates of x_b improve those of CWL for $U_b > U_f$, by including the leading-order $O(\epsilon^{2/3})$ corrections arising both from the local modifications to the shape in the boundary layer at the belt and from the global modification to the shape of the tail caused by the increased length for stretching near the belt. Moreover, the theory presented here provides solutions where the theory of CWL could not, as the bending stresses within the gravitational and compressional heels are able to support a small amount of compression.

Throughout this chapter the effects of surface tension and inertia have been neglected for simplicity. We now state that, while the vertical velocity profile within the tail is modified as discussed in chapter 3, the structure of the steady boundary-layer solutions found in this paper remains unchanged at leading order. This follows from inspection of (3.2.1)–(3.2.7), which show that the effects of surface tension and inertia are only to modify the constitutive relation (3.2.7) and to give an $O(\epsilon^2)$ contribution to the torque balance (4.2.8) through \mathcal{M} . The contribution to \mathcal{M} is negligible compared to the corresponding terms in $\mathbf{d}_3 \times \mathbf{N}$ when $\epsilon \ll 1$. Since the thread speed U is approximately constant in the boundary layer near the belt, the inclusion of surface tension and inertia simply changes the axial stress at the bottom of the thread by a constant amount. This effect may be accounted for by a simple rescaling of variables.

CHAPTER 5

THE STABILITY OF A STEADILY DRAGGED VISCOUS THREAD

5.1 Introduction

We now extend the analysis of chapter 4 by considering the stability of a dragged viscous thread to unsteady motion. Although bending stresses are able to support a small amount of compression by forming a backward-facing heel, for sufficiently slow belt speeds this heel is itself unstable to buckling and the motion is unsteady.

During unsteady motion, the buckling of the heel and the motion of the belt combine to give rise a rich variety of possible patterns laid down by the thread as it falls onto the belt (CWL, figure 5.1). Provided the fall height is not too large, the behaviour of the thread is very repeatable, and is characterised by a clearly delineated regime diagram (CWL; Morris *et al.*, 2007, figure 5.2). The primary instability of a dragged thread as the belt speed is slowed is a transverse oscillation of the thread (CWL), hereafter referred to as 'meandering'. Detailed measurements of the unsteady thread motion were made by Morris *et al.* (2007), which included the motion of the contact point. During meandering the

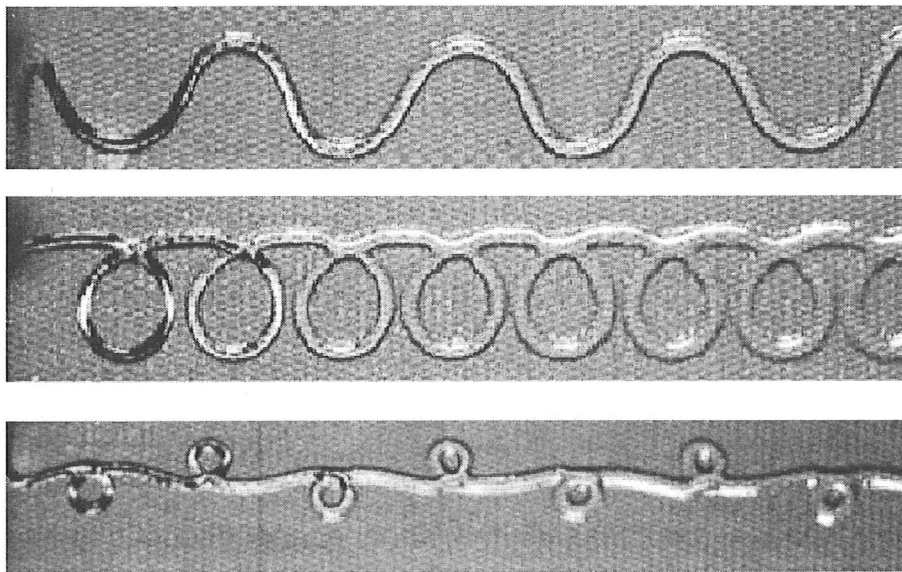


Figure 5.1: Top views of the experiments of CWL showing some of the patterns made by the thread after it has fallen onto the belt.

contact point moves primarily in a transverse direction to the belt motion, with only a very small motion of the contact point in the direction of belt motion. Further, measurement of the meandering amplitude as the belt speed is varied indicates that the onset of meandering is well described as an out-of-plane Hopf bifurcation from the steady state.

A theoretical analysis of the meandering instability was performed by R06c. They noted that since the steady state lies completely in the x - z plane, small unsteady perturbations to the steady motion decouple into two systems, which correspond respectively to ‘out-of-plane’ perturbations in the y direction, and to ‘in-plane’ perturbations in the x - z plane. They used a slender-thread model to perform a linear stability analysis of the steady state, and obtained very good agreement with experiment for both the onset and the frequency of meandering at onset. However, the mathematical model includes many dynamical effects and results in a complicated 17th order two-point boundary-value problem, which makes it a little difficult to extract a more physically based understanding of the solution structure and instability.

In order to determine the key physical processes that govern the onset of meandering, we re-examine the model of R06c in the asymptotic limit of a very slender thread. We will show that during meandering, bending forces in the heel cause it to move sideways and away from beneath the nozzle. As the heel moves further away from the nozzle, the consequent deflection of the tail from vertical causes the nozzle to exert an increasing restoring force on the thread. When this force is sufficiently large, the heel starts to be pulled back towards $y = 0$. As the heel returns, its deformation introduces bending and

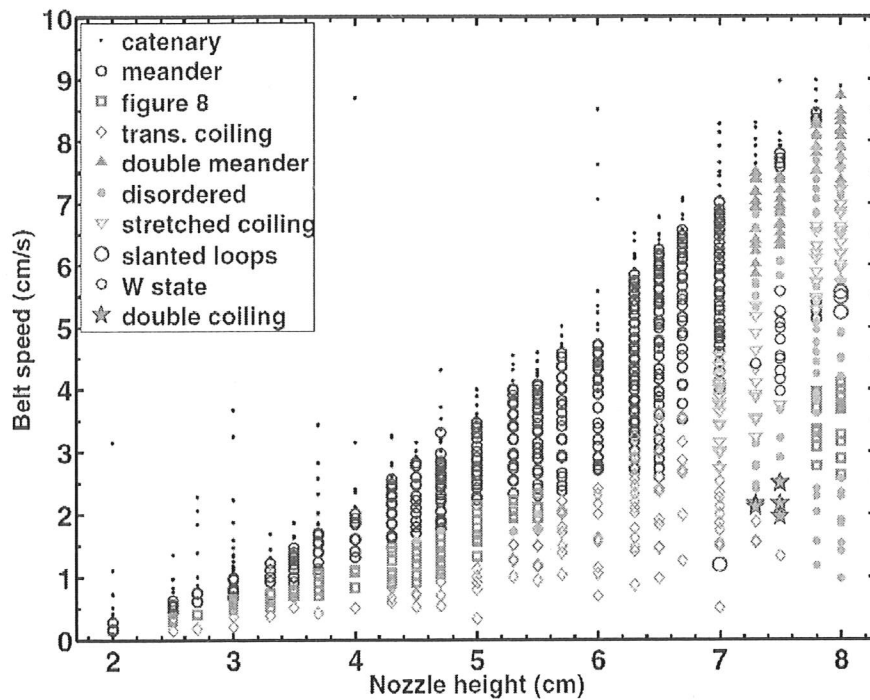


Figure 5.2: Regime diagram (from Morris et al., 2007) showing the observed ‘stitching’ patterns made by a slender viscous thread of silicon oil as it falls onto a moving belt.

twisting, which provide the disturbance that causes the heel to buckle again during the next half-oscillation. The interaction between the bending and twisting forces in the heel and the restoring tension in the tail determines the frequency of meandering oscillations. By matching both force and displacement between the heel and the tail, we will obtain an asymptotic estimate for the meandering frequency and the linearised growth rate near onset, and thence deduce an asymptotic estimate for the boundary between stable steady states and meandering threads. The analysis builds on many of the ideas developed in chapters 3 and 4. In particular, we find that the onset of meandering occurs within the gravitational-heel regime. This might be anticipated on the grounds that the onset of instability is likely to occur when some, but not much, of the thread is under compression.

5.2 Perturbation equations

In order to analyse the stability of a gravitational heel, we rescale the variables in the same way as in §4.5. The effect is that velocities are nondimensionalised with the belt speed U_B , radii with the radius a_B of the thread at the belt, axial lengths with

$$\delta_G = \delta_g H = \left(\frac{3a_B^2 H^2}{4} \right)^{1/4}, \quad (5.2.1)$$

angular velocities and growth rate with U_B/δ_G , stresses with $\mu\pi a_B^2 U_E \delta_G/H^2$ and stress moments with $\mu\pi a_B^2 U_E \delta_G^2/H^2$. The rescaled arclength of the heel is now $O(1)$, while the rescaled length of the tail is now $L_\delta = L/\delta_G$, which is $O(\epsilon^{-1/2})$ as $\epsilon \rightarrow 0$.

We analyse the unsteady motion of the thread by seeking eigenmodes of the linearised equations for unsteady perturbations to a steadily dragged thread. The relevant perturbation variables, which concern only out-of-plane motion, are y , d_{1y} , d_{3y} , κ_1 , κ_3 , M_1 , M_3 and N_2 , where $d_{1y} = \mathbf{d}_1 \cdot \mathbf{e}_y$ and $\kappa_1 = \boldsymbol{\kappa} \cdot \mathbf{d}_1$ etc. We denote the structure of the eigenmodes by, for example, $y = \hat{y}(s)e^{\sigma t}$, where a hat denotes the complex amplitude and σ is the complex growth rate of the perturbation. We also now denote the steady variables by overbars.

The governing equations for unsteady motion of a slender dragged thread are obtained by linearising (3.2.1)–(3.2.7) about the steady state. We continue to omit the effects of surface tension, inertia and the $O(\epsilon^2)$ terms that represent unimportant regular perturbations to the stretching-dominated theory of CWL. The omission of inertial effects means that the only time dependent terms are due to the kinematic effect of rotation of the basis vectors \mathbf{d}_i as the thread moves.

The equations that govern the shape and orientation of the thread are obtained by linearisation of (3.2.1) and (3.2.2), and are

$$\hat{y}' = \hat{d}_{3y} \quad (5.2.2)$$

$$\hat{d}'_{1y} = -\bar{\kappa}_2 \hat{d}_{3y} + \hat{\kappa}_3 \bar{d}_{2y} \quad (5.2.3)$$

$$\hat{d}'_{3y} = \bar{\kappa}_2 \hat{d}_{1y} - \hat{\kappa}_1 \bar{d}_{2y}, \quad (5.2.4)$$

We define the orientation of the Lagrangian basis so that $\mathbf{d}_1 = \mathbf{e}_z$ at the contact point with the belt, and choose the rotation rate of the basis to follow that of the fluid thread, so that $\omega_0 = 0$ in (3.2.3). Then linearisation of (3.2.3) yields

$$\hat{\omega}_1 = \bar{U} \hat{\kappa}_1 + \sigma \hat{d}_{3y}$$

$$\hat{\omega}_3 = \bar{U} \hat{\kappa}_3 - \sigma \hat{d}_{1y}.$$

The projections of the constitutive relation (3.2.6) onto \mathbf{d}_1 and \mathbf{d}_3 are

$$\hat{\omega}'_1 = \frac{\hat{M}_1}{\bar{a}^4} + \sigma \bar{\kappa}_2 \hat{d}_{1y} \quad (5.2.5)$$

$$\hat{\omega}'_3 = \frac{3\hat{M}_3}{2\bar{a}^4} + \sigma \bar{\kappa}_2 \hat{d}_{3y}, \quad (5.2.6)$$

and the corresponding force and torque balances are obtained by linearising (3.2.4) and (3.2.5), which gives

$$\hat{N}'_2 = \bar{N}_3 \hat{\kappa}_1 - \bar{N}_1 \hat{\kappa}_3 + \bar{a}^2 \hat{d}_{2z} \quad (5.2.7)$$

$$\hat{M}'_1 = \bar{M}_2 \hat{\kappa}_3 - \bar{\kappa}_2 \hat{M}_3 + \hat{N}_2 \quad (5.2.8)$$

$$\hat{M}'_3 = \bar{\kappa}_2 \hat{M}_1 - \bar{M}_2 \hat{\kappa}_1. \quad (5.2.9)$$

As in the steady problem, kinematic boundary conditions prescribe the position and velocity at the nozzle and at the contact point, and dynamic conditions prescribe the orientation and curvature. The conditions at the contact point with the belt are

$$\hat{\omega}_1 = \hat{\omega}_3 = 0 \quad \text{and} \quad \bar{U} \mathbf{d}_3 + \partial y / \partial t \mathbf{e}_y = U_b \mathbf{e}_x \quad \text{at} \quad s = 0. \quad (5.2.10a-c)$$

We also impose the choice that $\mathbf{d}_1 = \mathbf{e}_z$ at the contact point. By eliminating $\hat{\omega}_i$ in favour of $\hat{\kappa}_i$ and projecting (5.2.10c) onto \mathbf{e}_y , we obtain the boundary conditions

$$\bar{U} \hat{\kappa}_1 = -\sigma \hat{d}_{3y}, \quad \hat{\kappa}_3 = 0, \quad \sigma \hat{y} = -\bar{U} \hat{d}_{3y} \quad \text{and} \quad \hat{d}_{1y} = 0 \quad \text{at} \quad s = 0. \quad (5.2.11a-d)$$

The boundary conditions imposed at the nozzle are

$$\hat{y} = 0, \quad \hat{d}_{3y} = \hat{\omega}_1 = 0 \quad \text{and} \quad \hat{\omega}_3 = 0 \quad \text{at} \quad s = -L_\delta. \quad (5.2.12a-d)$$

5.2.1 Numerical solution

The differential equations (5.2.2)–(5.2.9) and the eight boundary conditions (5.2.11) and (5.2.12) together constitute an eigenvalue problem, which is linear in the perturbation variables and has non-trivial solutions only for discrete values of the growth rate σ . We use the same ‘push–pull’ procedure to determine these eigenmodes as R06c. This procedure begins with a steady solution, obtained as described in §4.2.1, with all perturbation variables set to zero and an initial guess made for the growth rate. A non-trivial eigenmode is then computed by ‘pushing’ $\hat{\omega}_1$ to some non-zero value at the belt, while σ is held fixed. The resulting solution satisfies all boundary conditions except (5.2.11c). In the next step, $\hat{\omega}_1$ is ‘pulled’ back to zero at the belt so that (5.2.11c) is reimposed, while the value of \hat{M}_1 at the belt is held fixed at its non-zero value and the growth rate is allowed to vary. The result is a non-trivial eigenmode, with associated growth rate σ , which satisfies all boundary conditions. Since the perturbation system was obtained by linearisation, the eigenmode is determined only up to a multiplicative constant.

The onset of meandering instability is determined by beginning from a steady solution that is expected to be unstable but close to onset. The perturbation eigenmode with largest positive growth rate is determined by computing eigenmodes for a series of initial guesses for σ . Once the most unstable eigenmode is obtained, the onset of meandering instability is then found by adjusting the growth rate of this eigenmode to zero while allowing the meandering frequency and the belt speed to vary. The resulting eigenmode is neutrally stable and has an associated meandering frequency $\text{Im}(\sigma)$.

5.3 Asymptotic solution for the perturbation eigenmode as $\epsilon \rightarrow 0$

By analogy with a steadily dragged thread, we anticipate that the bending and twisting stresses in a meandering thread are negligible as $\epsilon \rightarrow 0$, except within a small boundary layer near the belt. Thus the eigenmode also divides asymptotically into heel and tail regions.

As the heel meanders, the bending stresses in the heel exert a force $\hat{\phi}_y = \bar{N}_1 \hat{d}_{1y} + \hat{N}_2 \bar{d}_{2y} + \bar{N}_3 \hat{d}_{3y}$ on the base of the tail and the motion of the heel requires a deflection \hat{y}_t of the base of the tail. The relationship between this out-of-plane force and deflection is analogous to the relationship (4.7.1) between the in-plane variables $\bar{\phi}_x$ and \bar{x}_t in the steady state. Hence

$$\hat{y}_t = \hat{\phi}_y \ln L_\delta. \quad (5.3.1)$$

Since $\hat{y} = 0$ where the thread is pinned at the nozzle, (5.3.1) implies the constraint

$$\hat{y}_b = \hat{\phi}_y \ln L_\delta + \hat{y}_\ell, \quad (5.3.2)$$

where \hat{y}_b represents the out-of-plane displacement of the contact point with the belt, and \hat{y}_ℓ represents the contribution from the out-of-plane curvature in the heel. As for the steady gravitational heels discussed in §4.5, the system of differential equations in the heel admits bending and twisting modes that do not decay towards the tail. These modes must be suppressed in the asymptotic solution by imposing matching conditions which we now determine.

5.3.1 Matching conditions towards the tail, $1 \ll |\eta| \ll L_\delta$

The matching conditions (4.5.11) imply that the steady-state variables $\bar{\kappa}_2$, \bar{M}_2 and \bar{N}_1 all decay away from the heel. It follows that (5.2.5), (5.2.7) and (5.2.8) reduce to equations for the out-of-plane bending variables $\hat{\omega}_1$, \hat{M}_1 and \hat{N}_2 that are equivalent to the in-plane bending equations that gave (4.5.2). There are therefore two out-of-plane bending modes, analogous to those in (4.5.5), that do not decay away from the heel and must be suppressed by imposing

$$\hat{d}_{3y} = -\frac{\hat{\phi}_y}{\eta} + o\left(\frac{1}{\eta}\right) \quad \text{and} \quad \hat{d}'_{3y} = \frac{\hat{\phi}_y}{\eta^2} + o\left(\frac{1}{\eta^2}\right), \quad 1 \ll -\eta \ll L_\delta. \quad (5.3.3a, b)$$

These matching conditions are analogous to the steady in-plane conditions (4.5.11). We also need a condition on the twisting mode. We will see that a heel that meanders with amplitude \hat{A} has an $O(\hat{A}\sigma^2)$ twisting rate. In order to satisfy $\hat{\omega}_3 = 0$ at the nozzle, this twisting rate must be modified across the $O(L_\delta)$ length of the tail, and hence it follows that

$$\hat{M}_3 = O(\hat{A}\sigma^2/L_\delta), \quad 1 \ll -\eta \ll L_\delta. \quad (5.3.3c)$$

The matching conditions (5.3.3) replace (5.2.12b–d) in the tail, while (5.3.2) replaces the displacement condition (5.2.12a). The eigenmode is again determined up to a multiplicative constant, which we now set by imposing a fixed amplitude \hat{A} . This amplitude is independent of σ , and hence the only contribution to the out-of-plane displacement at the belt appears at leading order, with no contributions at $O(\hat{A}\sigma)$ or higher.

We consider the out-of-plane motion of the heel near onset of meandering, so that $\text{Re}(\sigma) \ll 1$. We define the amplitude \hat{A} of the oscillations by $\hat{A} = \hat{y}_b$. Then integration of (5.3.2) implies that $\hat{\phi}_y = O(\hat{A}/\ln L_\delta)$. Hence, as $\epsilon \rightarrow 0$ so that $L_\delta \rightarrow \infty$, a fixed meandering amplitude requires an asymptotically small restoring force. We therefore expect $\text{Im}(\sigma) \ll 1$ for a very slender thread. This motivates expansion of the eigenmode

in powers of σ for $|\sigma| \ll 1$. Since formally setting $\sigma = 0$ represents a steady solution, the leading-order behaviour of the eigenmode at $O(\hat{A}\sigma^0)$ is steady. The steady solution that satisfies (5.2.2)–(5.2.9) and the conditions (5.3.2), (5.2.11) and (5.3.3) is simply a uniform displacement of the entire heel with $\hat{y} = \hat{A}$ and with all other perturbation variables vanishing.

The $O(\hat{A}\sigma)$ contribution to the eigenmode is forced only through the condition (5.2.11c) that $\sigma\hat{y} = -\bar{U}\hat{d}_{3y}$ at the belt, which corresponds to a quasi-steady translation of the contact point with velocity $\hat{A}\sigma$. This forced problem is equivalent to a small change to the direction of belt motion, for which the solution is simply a rotation of the steady heel about the vertical axis through an angle $\hat{A}\sigma$. We therefore pose the solution

$$\hat{y} = \hat{A} - \hat{A}\sigma(\bar{x} - \bar{x}_b) + O(\hat{A}\sigma^2) \quad (5.3.4)$$

$$\hat{d}_{3y} = -\hat{A}\sigma\bar{d}_{3x} + O(\hat{A}\sigma^2) \quad (5.3.5)$$

$$\hat{d}_{1y} = -\hat{A}\sigma\bar{d}_{1x} + O(\hat{A}\sigma^2) \quad (5.3.6)$$

$$\hat{\kappa}_1, \hat{M}_1, \hat{N}_2, \hat{\kappa}_3, \hat{M}_3 \sim O(\hat{A}\sigma^2). \quad (5.3.7)$$

It is easy to verify that this solution satisfies the perturbation equations (5.2.2)–(5.2.9) and all boundary and matching conditions to $O(\hat{A}\sigma)$. The uniform translation $\hat{A}\sigma\bar{x}_b$ is included in (5.3.4) so that \hat{y}_b remains equal to \hat{A} .

The $O(\hat{A}\sigma^2)$ terms in the eigenmode are forced only through the condition (5.2.11a) that $\bar{U}\hat{\kappa}_1 = -\sigma\hat{d}_{3y}$ at the belt. The $O(\hat{A}\sigma^2)$ contribution can not be expressed as a simple geometrical operation and must be determined numerically. The $O(\hat{A}\sigma^3)$ terms in the eigenmode are forced both at the belt through (5.2.11a) and internally through (5.2.5) and (5.2.6).

5.4 Estimation of onset and frequency of instability

Equation (5.3.4) and the definitions of \hat{y}_t and \bar{x}_t give

$$\hat{y}_t = \hat{A} - \hat{A}\sigma\bar{x}_t + O(\hat{A}\sigma^2). \quad (5.4.1)$$

Equations (5.3.5)–(5.3.7) and the definition of $\hat{\phi}_y$ imply that

$$\hat{\phi}_y = -\hat{A}\sigma\bar{\phi}_x - \hat{A}\sigma^2 G_0 + O(\hat{A}\sigma^3), \quad (5.4.2)$$

where the $O(1)$ constant G_0 depends only on the shape of the steady heel and can be determined numerically from the $O(\hat{A}\sigma^2)$ contribution to the eigenmode. If we select the

phase of the oscillation so that \hat{A} is real, then the expansion of the eigenmode in powers of σ yields systems of equations that have real coefficients. Hence the solution at each power of σ is real, and G_0 is also real.

Substitution of (5.4.1) and (5.4.2) into (5.3.2) yields

$$\hat{A} = -\hat{A}\sigma\bar{\phi}_x \ln L_\delta - \hat{A}\sigma^2 G_0 \ln L_\delta + O(\hat{A}\sigma, \hat{A}\sigma^3 \ln L_\delta). \quad (5.4.3)$$

If $\bar{\phi}_x \neq 0$ then a leading-order balance would imply that $\sigma = -1/(\bar{\phi}_x \ln L_\delta)$. If $\bar{\phi}_x$ is held constant as $L_\delta \rightarrow \infty$, then solution at successive powers of σ would further imply that the meandering frequency $\text{Im}(\sigma)$ is $O(1/\ln L_\delta^3)$. Hence the eigenmode would grow or decay far faster than it would oscillate as $L_\delta \rightarrow \infty$, which is not what is observed experimentally near onset.

Since we wish to determine the behaviour near onset, we require $\text{Re}(\sigma) \ll \text{Im}(\sigma) \ll 1$. To this end, we consider a distinguished limit with $\bar{\phi}_x = F_0/\sqrt{\ln L_\delta} + O(1/\ln L_\delta)$ as $L_\delta \rightarrow \infty$. Substitution into (5.4.3) yields

$$1 = -\sigma F_0 \sqrt{\ln L_\delta} - \sigma^2 G_0 \ln L_\delta + O(\sigma, \sigma^3 \ln L_\delta), \quad (5.4.4)$$

and hence

$$\sigma = \frac{-F_0 \pm i\sqrt{4G_0 - F_0^2}}{2G_0 \sqrt{\ln L_\delta}} + O\left(\frac{1}{\ln L_\delta}\right). \quad (5.4.5)$$

We see from (5.4.5) that the onset of meandering ($\text{Re}(\sigma) = 0$) corresponds to $F_0 = 0$, and hence the marginally stable steady shape has $\bar{\phi}_x = \bar{\phi}_x^*$, where $\bar{\phi}_x^* = O(1/\ln L_\delta)$ as $L_\delta \rightarrow \infty$. The meandering frequency at onset is given by

$$\sigma^* = \pm \frac{i}{\sqrt{G_0 \ln L_\delta}} + O\left(\frac{1}{\ln L_\delta}\right). \quad (5.4.6)$$

5.5 Quantitative estimates

The value of G_0 depends on the steady shape of the heel, and therefore on $\bar{\phi}_x$. For the moment, we make the approximation that $\bar{\phi}_x^* = 0$ rather than $O(1/\ln L_\delta)$. Under this approximation, (5.4.3) remains accurate at the order given.

Figure 4.5 shows that there are many heel solutions for which $\bar{\phi}_x = 0$. However, we expect that the initial onset of meandering, as \bar{U}_b is reduced, corresponds to the first of these heels, and hence to the heel that is under the smallest amount of vertical compression. This heel has $\bar{\Phi}_z = 0.82$, and is shown in figure 4.4. If the belt speed is reduced

slightly further, so that $\bar{\Phi}_z$ has a slightly larger value, then figure 4.5 shows that $\bar{\phi}_x < 0$. The parameter $F_0 < 0$ is then negative and (5.4.5) implies that the heel is unstable to meandering at the reduced speed, which is in agreement with the experimentally observed direction of instability.

Substitution of the leading-order estimate $\bar{\Phi}_z^* = 0.82$ into (4.5.10) implies that the onset of meandering occurs at a critical belt speed

$$\bar{U}_b^* = \bar{U}_f \left(1 - 0.82 \frac{4\delta_g}{3\pi^2} + O\left(\frac{\delta_g}{\ln \delta_g}\right) \right). \quad (5.5.1)$$

The dimensional estimate U_B^* for the critical belt speed is obtained by multiplying both sides by the extensional velocity scale $U_E = \rho g H^2 / \mu$. Substitution of $\delta_g = (3a_E^2/4H^2)^{1/4}$ (from 5.2.1) together with $a_E^2 = Q/\pi U_E$ then yields

$$\bar{U}_B^* = \bar{U}_F \left(1 - 0.82 \frac{4}{3\pi^2} \left(\frac{3\mu Q}{4\pi \rho g H^4} \right)^{1/4} + O\left(\frac{a_E^{1/2}}{H^{1/2} \ln(a_E/H)}\right) \right). \quad (5.5.2)$$

As described earlier, we calculate that $G_0 = 0.198$ for the heel with $\bar{\Phi}_z = 0.82$. Substitution into (5.4.6) gives the dimensional meandering frequency at onset as

$$\text{Im}(\sigma^*) = \pm \frac{\bar{U}_F}{H\delta_g} \left(\frac{2.25}{\sqrt{\ln \delta_g}} + O\left(\frac{1}{\ln \delta_g}\right) \right). \quad (5.5.3)$$

Figures 5.3 and 5.4 compare the values of \bar{U}_B^* and $\text{Im}(\sigma^*)$ calculated from the full numerical solution to the asymptotic estimates (5.5.2) and (5.5.3), for the parameter values corresponding to Experiment 5 of CWL. The estimate of \bar{U}_B^* improves on the corresponding estimate of CWL. The agreement is particularly good for large values of H since $\epsilon = a_E/H \propto H^{-2}$. The estimate (5.5.3) predicts the qualitative dependence of σ^* on H and is accurate to within 25%. The accuracy of the asymptotic estimates is reasonable given that the corrections to (5.5.2) and (5.5.3) are logarithmic in δ_g and hence decay slowly as $\epsilon \rightarrow 0$.

Equation (5.4.5) implies that the onset of meandering occurs when $\bar{\phi}_x^* = O(1/\ln L_\delta)$. In order to derive a quantitative estimate for $\bar{\phi}_x^*$ when $L_\delta \gg 1$, we pose the expansion

$$\bar{\phi}_x^* = \frac{F_1}{\ln L_\delta} + O\left(\frac{1}{(\ln L_\delta)^{3/2}}\right), \quad (5.5.4a)$$

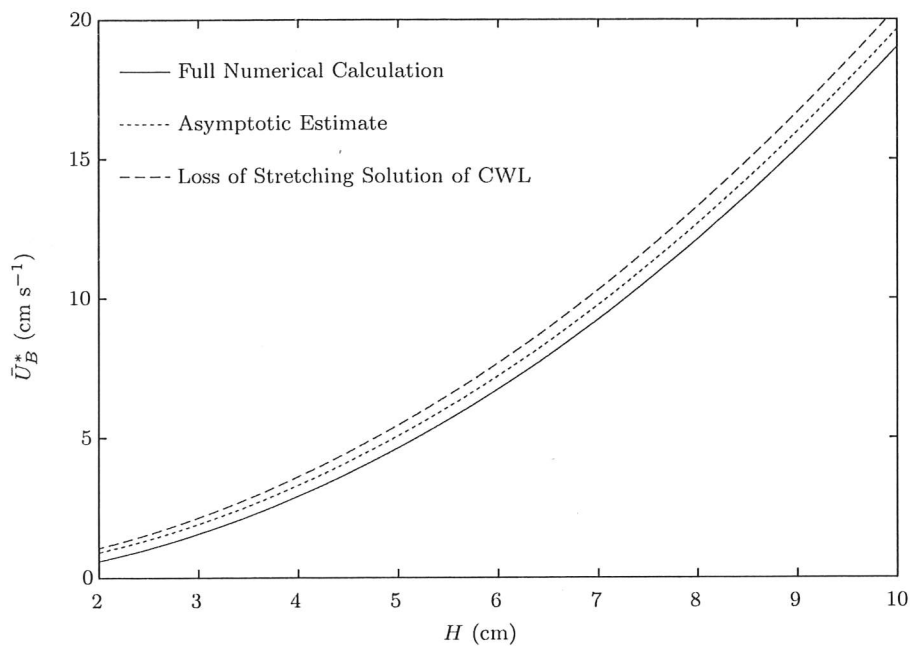


Figure 5.3: Asymptotic estimate of the neutrally stable belt speed \bar{U}_B^* compared to the full numerical solution of (5.2.2)–(5.2.9), (5.2.11) and (5.2.12), for parameter values corresponding to Experiment 5 of CWL.

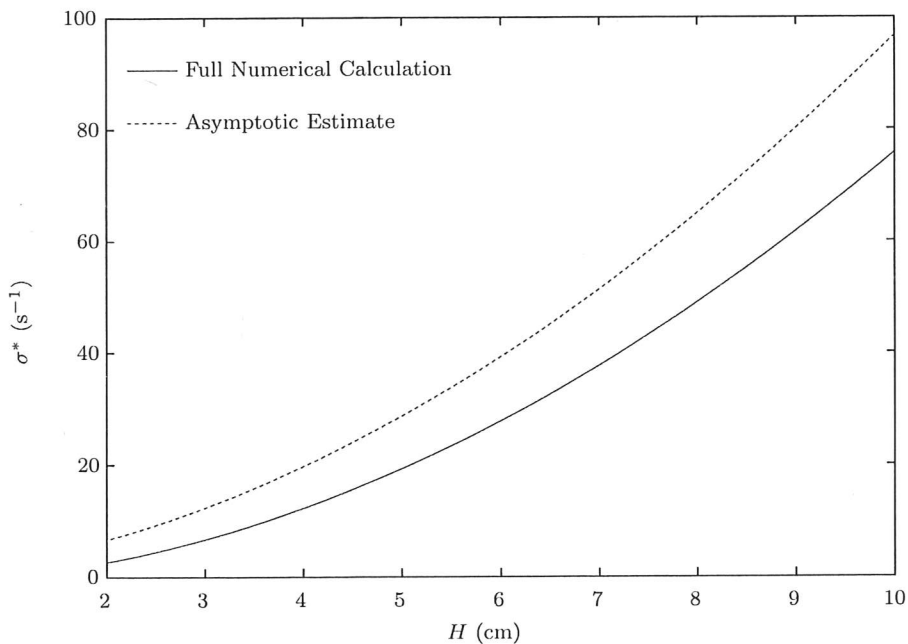


Figure 5.4: Asymptotic estimate of the meandering frequency σ^* at onset, compared to the full numerical solution of (5.2.2)–(5.2.9), (5.2.11) and (5.2.12), for parameter values corresponding to Experiment 5 of CWL.

for the steady state at onset, and extend the expansions

$$\hat{y}_\ell = -\hat{A}\sigma\bar{x}_\ell + O(\hat{A}\sigma^2) \quad (5.5.4b)$$

$$\hat{\phi}_y = -\hat{A}\sigma\bar{\phi}_x + \hat{A}G_0\sigma^2 + \hat{A}G_1\sigma^3 + O(\hat{A}\sigma^4) \quad (5.5.4c)$$

$$\sigma = \frac{i}{G_0\sqrt{\ln L_\delta}} + \frac{\sigma_1}{\ln L_\delta} + O\left(\frac{1}{(\ln L_\delta)^{3/2}}\right), \quad (5.5.4d)$$

for the relevant parts of the eigenmode and σ . Substitution of (5.5.4) into (5.3.2) yields

$$F_1 + \bar{x}_\ell + 2\sigma_1 G_0 - \frac{G_1}{G_0} = 0. \quad (5.5.5)$$

The parameters G_0 and G_1 again depend on $\bar{\phi}_x$, and hence on F_1 . However, calculation of G_0 , G_1 and \bar{x}_ℓ with $F_1 = 0$ introduces only an $O(\hat{A}\sigma^3)$ error in (5.5.4b) and an $O(\hat{A}\sigma^4)$ error in (5.5.4c), which does not affect the calculation of σ_1 . We therefore make this approximation and calculate $\bar{x}_\ell = 2.08$ and $G_1 = 0.220$ for the heel with $\bar{\Phi}_z = 0.82$. The leading-order estimate for $\bar{\phi}_x^*$ at onset of meandering is then obtained by setting $\sigma_1 = 0$ to give

$$\bar{\phi}_x^* = -\frac{0.969}{\ln L_\delta} + O(\ln L_\delta^{-3/2}). \quad (5.5.6)$$

Since $\bar{\phi}_x^*$ is negative, it corresponds to a steady shape with a backward-facing heel in agreement with experimental observations near the onset of meandering.

5.6 Discussion

The above analysis of unsteady motion has provided a better understanding of the meandering instability observed experimentally, and yields simple asymptotic estimates (5.5.2) and (5.5.3) of the onset and frequency of meandering. The pinning of the thread at the nozzle, the physical effects of which had not previously been considered, plays a crucial role, since the scaling of the meandering frequency is determined from the restoring force generated by deflection of the tail.

At leading order, the asymptotic model predicts that neutral stability occurs when the horizontal force $\bar{\phi}_x \approx 0$ and the vertical force $\bar{\Phi}_z \approx 0.82$. This estimate differs from the estimate of CWL, which is equivalent to $\bar{\Phi}_z = 0$ here. Our estimate $\bar{\phi}_x \approx 0$ has the simple physical interpretation that the thread is stable to meandering if bending forces in the heel pull the tail in the same direction as the belt motion, and unstable if the tail is instead pushed against the belt motion. Calculation of the next term (5.5.6) in the asymptotic expansion shows that instability occurs only if the push exceeds a small positive value.

While the aim of the above analysis was to determine the behaviour of the thread at neutral stability, we note that the asymptotic expansion also holds for oscillations with an $O(1/\sqrt{\ln \delta_g})$ growth rate and may thus be used to determine the growth rate of meandering oscillations close to onset.

For unsteady motion at large fall heights, inertial effects are important since there are centrifugal and Coriolis accelerations that have not been considered here. These accelerations are likely to be dynamically important when the thread undergoes some of the more exotic ‘stitching’ motions observed by CWL and Morris *et al.* (2007) for larger fall heights. This effect falls outside the scope of this thesis, but chapter 6 analyses the effects of inertia in the closely related problem of a steady coiling thread.

We have analysed the behaviour of the thread near onset of unsteady motion, but we have not considered the development of the instability into the nonlinear regime. Morris *et al.* (2007) present a phenomenological fit that gives an estimate of the amplitude of the meanders near onset of meandering. Their analysis suggests that unsteady in-plane motion is a quadratic perturbation to the steady state and forced by the meandering state. Hence the simple model of meandering presented in this chapter opens up a potential avenue for analysis of in-plane perturbations and more complicated patterns.

CHAPTER 6

THE STEADY COILING OF A FLUID THREAD

6.1 Introduction

We now turn to the phenomenon of steady coiling of a fluid thread, as is commonly observed when pouring honey onto a slice of toast. Early investigations of this phenomenon (Barnes & Woodcock, 1958; Barnes & MacKenzie, 1959) observed that a fluid thread falling steadily from a nozzle onto a stationary surface forms regular coils. These experiments measured the dependence of coiling radius and frequency on fall height, but no explanation was given for the underlying physical processes that govern the coiling of the thread.

Cruickshank & Munson (1982) analysed the behaviour of the thread during coiling, and noted that for larger fall heights, the thread falls almost vertically from the nozzle under gravity, forming a 'tail', until it reaches a small region near the surface. Within this region, the thread slows down and buckles to form coils. We will refer to this region as the 'coil' (figure 6.1*a*). Cruickshank & Munson (1982) also demonstrated that the flow within the tail is well described by extensional flow. This motivates the use of the results in chapter 3 to aid the analysis of this chapter. While the physical processes that govern the tail are

well understood, progress towards understanding the physical processes that take place in the coil has been made only recently.

Early theoretical progress towards understanding the motion in the coil was made by Mahadevan *et al.* (1998; 2000), who considered the role of bending stress during fluid coiling for the case of large fall heights. They demonstrated that for this case the motion within the coil is governed by a balance between bending stress and centrifugal acceleration. Scalings for the coiling frequency and radius were thereby obtained, which apparently agreed well with experiment. However, we will show in §6.4 that a quantitative prediction of the coiling radius and frequency requires, in addition, an understanding of the dynamical influence of the tail.

Steady fluid coiling was analysed more extensively by R04 using a slender-thread model, which we present in §6.2.1. The predicted coiling frequency has been shown (Maleki *et al.*, 2006) to agree very well with experiment over a wide range of fall heights. Further, the model revealed that a steadily coiling thread may fall into one of four distinct dynamical regimes, each of which corresponds to a distinct force balance in the coil. These force balances involve the viscous forces in the coil, which either are dominant or are in balance with gravity, with inertia or with both. In each regime, the force balance yields scaling estimates for the coiling frequency and radius that agree with experiment and numerical simulation (R04, R06b).

The ‘viscous’ regime occurs for heights of fall that are small enough that gravity and inertia both have a negligible effect. In this regime the dominant balance is between viscous bending and compressional forces (R04), and the coiling radius and frequency are determined kinematically by the extrusion speed and the height of the nozzle above the surface. By contrast, as in the analysis of chapters 4 and 5, we focus on regimes in which gravity strongly stretches the thread before reaching the surface, since bending stress is then important only in a coil at the bottom of the thread.

In this chapter we aim to determine the asymptotic structure of the thread within the coil, and thereby to derive simple quantitative estimates for the coiling frequency and radius. We focus in particular on the dynamic interaction between the coil and the tail, and we will show that the tail has an important influence on the coiling motion. The effect of the tail has to date been considered only in the ‘inertio-gravitational’ regime in which bending stresses are balanced by gravity in the coil, but inertia plays an important dynamical role in the tail (e.g. R06b). Within this regime, steady fluid coiling can occur with several distinct coiling frequencies for fixed experimental parameters (figure 6.1*b,c*). R06b postulated that the multiplicity of stable coiling frequencies is caused by a resonance phenomenon, in which motion of the tail is forced by bending stress in the coil. The resonant coiling frequencies were demonstrated to correspond to the eigenfrequencies of ‘whirling pendulum modes’ of the tail. We discuss this phenomenon in more detail in §6.6.

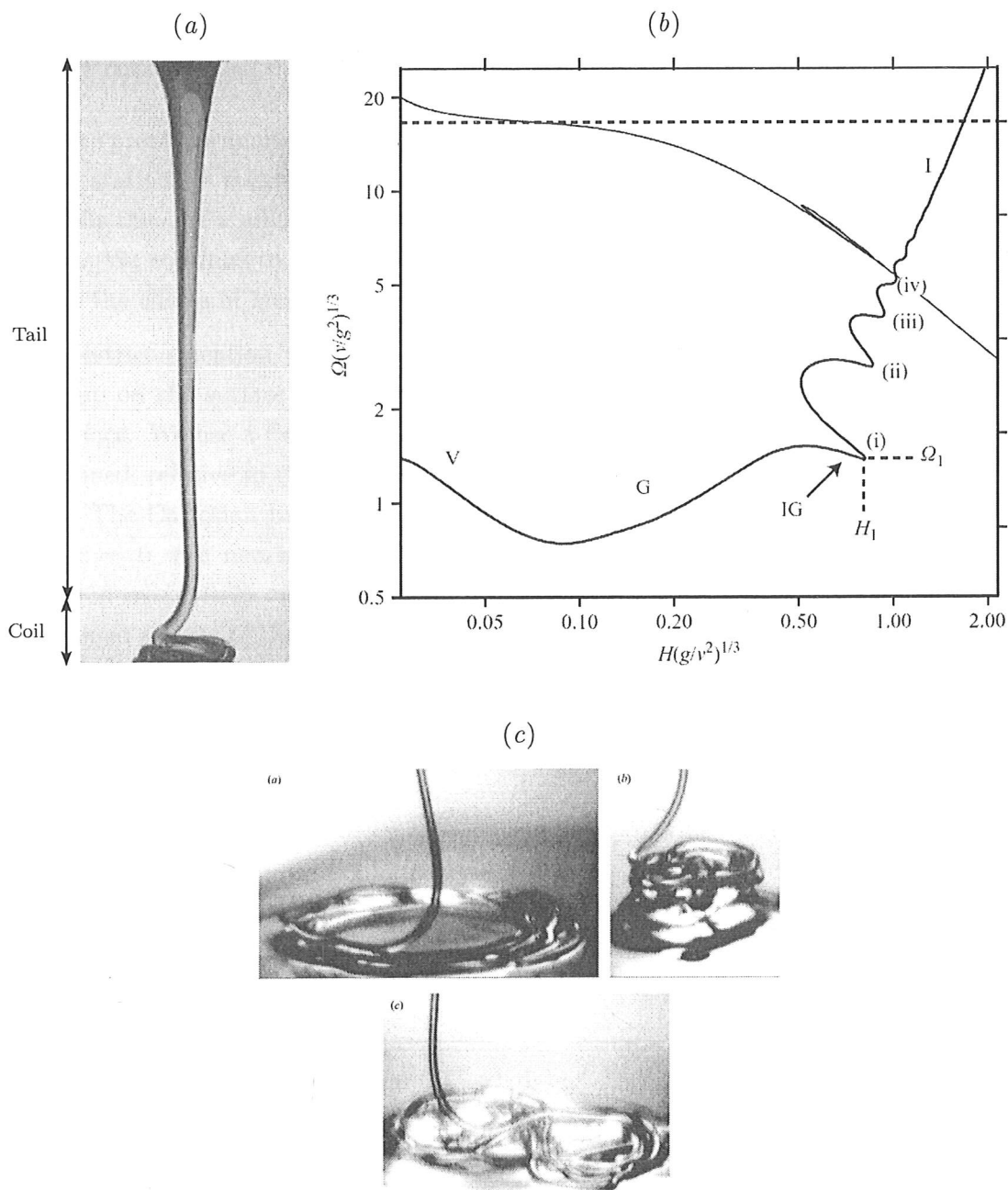


Figure 6.1: Figures taken from R06b, illustrating some of the phenomenology of coiling. (a) Photograph of a thread of viscous corn syrup coiling as it lands on a rigid surface. The thread forms a long 'tail' that is stretched by gravity, with a 'coil' at the base where bending effects are important. (b) The dependence of coiling frequency on height of fall. There are four distinct regimes which are labelled V ('viscous' coiling), G ('gravitational' coiling), IG ('inertio-gravitational' coiling) and I ('inertial' coiling). In the inertio-gravitational regime, several steady coiling frequencies may coexist. (c) Coexisting coiling states, and the 'figure-of-eight' pattern made by the thread during transition between states. All three pictures were taken under identical experimental conditions.

6.2 Steady fluid coiling

6.2.1 Problem description

As in the problems analysed in chapters 4 and 5, we consider a fluid thread that is extruded from a stationary nozzle at a constant dimensionless volume flux $Q = \pi$. The thread then falls through a unit dimensionless height before landing onto a stationary horizontal surface. We continue to omit the effects of surface tension by setting $\Gamma = 0$, but we will include the effects of inertia in the analysis that follows.

We restrict attention to steady coiling, and we omit the secondary effect of the fluid piling up on the surface by assuming that the fluid vanishes after making contact with the surface. We use a frame of reference that rotates with the coiling frequency Ω , to be determined, relative to the laboratory frame, so that the coil is stationary in the rotating frame. The Cartesian basis $(\mathbf{e}_x, \mathbf{e}_y, \mathbf{e}_z)$ of this frame is chosen so that the surface is the plane $z = 0$, the nozzle is located at $(0, 0, 1)$ and the contact point with the surface is located at $(R, 0, 0)$, where R is the dimensionless coiling radius, which is also to be determined as part of the solution. The arclength is again chosen so that the origin $s = 0$ is at the contact point with the surface, and the nozzle is at arclength $s = -\ell$, where ℓ is also to be determined as part of the solution.

In the rotating frame, the form of the governing equations (3.2.1)–(3.2.7) for the coiling thread is given by

$$\mathbf{x}' = \mathbf{d}_3 \quad (6.2.1a)$$

$$\mathbf{d}'_3 = U^{-1}(\boldsymbol{\omega} - \Omega \mathbf{d}_3) \times \mathbf{d}_3, \quad (6.2.1b)$$

$$\check{\mathbf{N}}' = \pi a^2 \mathbf{e}_z + \pi a^2 \text{Fr} [\boldsymbol{\Omega} \times (\boldsymbol{\Omega} \times \mathbf{x}) + 2\boldsymbol{\Omega} \times \mathbf{U}] \quad (6.2.1c)$$

$$\mathbf{M}' = \mathbf{d}_3 \times \check{\mathbf{N}} + \epsilon^2 \mathcal{M} \quad (6.2.1d)$$

$$\mathbf{M} = \frac{\pi a^4}{4} \epsilon^2 (3\mathbf{I} - \mathbf{d}_3 \mathbf{d}_3) \cdot \boldsymbol{\omega}', \quad (6.2.1e)$$

$$\check{N}_3 = 3\pi a^2 U' - \pi \text{Fr} a^2 U^2, \quad (6.2.1f)$$

where (6.2.1c) now includes the inertial ‘fictitious forces’ associated with acceleration in a rotating reference frame. The spin rate ω_0 of the basis vectors \mathbf{d}_1 and \mathbf{d}_2 relative to the twist rate of the fluid in (6.2.1b) is defined to be constant and equal to Ω ; this ensures that the Lagrangian basis is stationary in the rotating frame. Further discussion is given in §6.2.3.

The stress-moment vector \mathcal{M} is given by

$$\mathcal{M} = \frac{\pi a^4}{4} \mathbf{e}_z \times (\boldsymbol{\kappa} \times \mathbf{d}_3) - \frac{\pi a^4}{4} \text{Fr} \mathbf{K}, \quad (6.2.2)$$

where $\boldsymbol{\kappa} = U^{-1}(\boldsymbol{\omega} - \Omega \mathbf{d}_3)$, and the components of \mathbf{K} are given by (R04)

$$\begin{aligned}\mathbf{K} \cdot \mathbf{d}_1 &= U(U\kappa_1)' - \Omega U' d_{1z} - \Omega^2 \kappa_1 \mathbf{x}_H \cdot \mathbf{d}_3 \\ &\quad + \Omega d_{2z}(\Omega d_{3z} + 2\omega_3) + U\kappa_2(\Omega + \omega_3) \\ \mathbf{K} \cdot \mathbf{d}_2 &= U(U\kappa_2)' - \Omega U' d_{2z} - \Omega^2 \kappa_2 \mathbf{x}_H \cdot \mathbf{d}_3 \\ &\quad - \Omega d_{1z}(\Omega d_{3z} + 2\omega_3) - U\kappa_1(\Omega + \omega_3) \\ \mathbf{K} \cdot \mathbf{d}_3 &= 2U\omega_3' - 2(\Omega d_{3z} + \omega_3)U' + \Omega^2 \boldsymbol{\kappa}_H \cdot \mathbf{x}_H + 4\boldsymbol{\Omega} \cdot (\mathbf{U} \times \mathbf{d}_3).\end{aligned}$$

Here \mathbf{x}_H and $\boldsymbol{\kappa}_H$ are the horizontal components of \mathbf{x} and $\boldsymbol{\kappa}$ respectively. The first term in (6.2.2) is the gravitational couple and the second term is the local moment of acceleration.

6.2.2 Boundary conditions

As in the problems analysed in chapters 4 and 5, kinematic conditions impose the position and velocity of the thread at the nozzle and at the contact point, and dynamic boundary conditions impose continuity of flow orientation and of angular velocity between the thread and the nozzle or surface. The nozzle is located at $(0, 0, 1)$, is vertical and has angular velocity $-\Omega \mathbf{e}_z$ in the rotating frame, and the dimensionless extrusion speed is U_n . Hence

$$x = y = 0 \quad \text{and} \quad z = 1 \quad (6.2.3a-c)$$

$$d_{3x} = d_{3y} = 0 \quad \text{and} \quad d_{3z} = -1 \quad (6.2.3d-f)$$

$$\omega_x = \omega_y = 0 \quad \text{and} \quad \omega_z = -\Omega \quad (6.2.3g-i)$$

$$U = U_n, \quad (6.2.3j)$$

at $s = -\ell$.

The contact point at $s = 0$ is assumed, without loss of generality, to lie on the x axis at $\mathbf{x} = (R, 0, 0)$ for some radius R . The orientation of the thread must be continuous at the contact point. For simplicity, we assume that the thread is horizontal at the contact point, thereby omitting the secondary effects of the fluid piling up after it lands on the surface. In steady coiling the contact point traces out a circle in the laboratory frame, and thus the tangent vector satisfies $\mathbf{d}_3 = -\mathbf{e}_y$ at the contact point in the rotating frame. Hence

$$x = R \quad \text{and} \quad y = z = 0 \quad (6.2.4a-c)$$

$$d_{3x} = d_{3z} = 0 \quad \text{and} \quad d_{3y} = -1, \quad (6.2.4d-f)$$

at $s = 0$.

In order for steady coiling to occur, rolling conditions must be applied at the contact point. This means that both the angular velocity of the thread and the curvature of the centreline are continuous there. The no-slip condition on the surface means that the angular velocity of the thread in the rotating frame is $-\Omega\mathbf{e}_z$ at the contact point. Hence

$$\omega_x = \omega_y = 0 \quad \text{and} \quad \omega_z = -\Omega, \quad \text{at} \quad s = 0. \quad (6.2.4g-i)$$

In the laboratory frame, the contact point traces out a circle of radius R on the surface $z = 0$. The curvature \mathbf{d}'_3 of the centreline at the contact point is therefore $-\mathbf{e}_x/R$. Since $\mathbf{d}_3 = -\mathbf{e}_y$ at the contact point, we may project (6.2.1b) onto \mathbf{e}_x to obtain $-1/R = \omega_z/U_c$, where U_c is the coiling speed. Hence from (6.2.4i),

$$\Omega = \frac{U_c}{R}. \quad (6.2.4j)$$

The system (6.2.1) of coiling equations is a 16th order system of differential equations, with three unknown parameters Ω , R and ℓ . Although the boundary conditions (6.2.3) and (6.2.4) comprise 20 boundary conditions, only 19 of them are independent since the tangent vector \mathbf{d}_3 has constant unit magnitude. We therefore dispense with (6.2.3f) and the remaining 19 boundary conditions complete the system.

6.2.3 Numerical solution

Later in this chapter we compare asymptotic estimates of the coiling speed and frequency to full numerical solutions of (6.2.1)–(6.2.4). These solutions are calculated using the method described by R04. The procedure is first to re-express (6.2.1)–(6.2.4) with respect to the Lagrangian axes \mathbf{d}_1 , \mathbf{d}_2 and \mathbf{d}_3 . Since $\omega_3 = \Omega$ at the nozzle in the rotating frame, \mathbf{d}_1 and \mathbf{d}_2 do not rotate there and thus are stationary. Since the offset between the twist rate of \mathbf{d}_1 and \mathbf{d}_2 and the actual twist rate of the fluid thread is defined to be constant, it follows that in the rotating frame the Lagrangian axes remain stationary everywhere in the thread.

It is convenient to use Euler parameters, denoted q_0, q_1, q_2, q_3 , to describe the orientation of the Lagrangian basis along the thread. These parameters are related to the more familiar Euler angles by (Goldstein, 1980)

$$\begin{aligned} q_0 &= \cos \left[\frac{1}{2}(\phi + \psi) \right] \cos \left(\frac{1}{2}\theta \right) & q_1 &= \cos \left[\frac{1}{2}(\phi - \psi) \right] \sin \left(\frac{1}{2}\theta \right) \\ q_2 &= \sin \left[\frac{1}{2}(\phi - \psi) \right] \sin \left(\frac{1}{2}\theta \right) & q_3 &= \sin \left[\frac{1}{2}(\phi + \psi) \right] \cos \left(\frac{1}{2}\theta \right), \end{aligned}$$

from which it follows that $q_0^2 + q_1^2 + q_2^2 + q_3^2 = 1$. Although it is more conventional to use Euler angles to describe a general rotation of coordinate axes, their use in this problem would introduce polar singularities in the tail where the thread is almost vertical. Hence we use the Euler parameters instead. These parameters can be shown to satisfy (Whittaker, 1944)

$$\mathbf{d}_i \cdot \mathbf{e}_j = \begin{bmatrix} q_0^2 + q_1^2 - q_2^2 - q_3^2 & 2(q_1q_2 + q_0q_3) & 2(q_1q_3 - q_0q_2) \\ 2(q_1q_2 - q_0q_3) & q_0^2 - q_1^2 + q_2^2 - q_3^2 & 2(q_2q_3 + q_0q_1) \\ 2(q_1q_3 + q_0q_2) & 2(q_2q_3 + q_0q_1) & q_0^2 - q_1^2 - q_2^2 + q_3^2 \end{bmatrix}, \quad (6.2.5)$$

and the variation of the Lagrangian basis (6.2.1*b*) along the thread can be expressed in terms of the Euler parameters by

$$q'_0 = -\frac{1}{2}[\kappa_1q_1 + \kappa_2q_2 + \kappa_3q_3] \quad (6.2.6)$$

$$q'_1 = \frac{1}{2}[\kappa_1q_0 - \kappa_2q_3 + \kappa_3q_2] \quad (6.2.7)$$

$$q'_2 = \frac{1}{2}[\kappa_1q_3 + \kappa_2q_0 - \kappa_3q_1] \quad (6.2.8)$$

$$q'_3 = \frac{1}{2}[-\kappa_1q_2 + \kappa_2q_1 + \kappa_3q_0]. \quad (6.2.9)$$

We now fix the orientation of \mathbf{d}_1 and \mathbf{d}_2 throughout the thread by setting \mathbf{d}_1 to be the principal normal $-\mathbf{e}_x$ at the contact point, from which it follows that \mathbf{d}_2 is the binormal $-\mathbf{e}_z$ to the thread at the contact point. Then the 5 boundary conditions (6.2.3*d,e*) and (6.2.4*d-f*) are replaced by the 6 conditions

$$q_0 = q_3 = 0 \quad \text{at} \quad s = -\ell \quad (6.2.10)$$

$$q_0 = q_1 = 0 \quad \text{and} \quad q_2 = -q_3 = \frac{1}{\sqrt{2}} \quad \text{at} \quad s = 0. \quad (6.2.11)$$

We note that we have replaced with the three variables d_{3i} with four variables q_i , thus increasing the order of the differential system by one. However, we have also imposed an additional boundary condition and the problem therefore remains well-posed.

The software package AUTO is again used to solve this problem. A similar method to that described in §4.2.1 is used, in which some of the boundary conditions are initially relaxed, the gravitational terms are omitted, and an initial 'quarter-circle' solution is used as a starting solution. Using continuation, the boundary conditions that were relaxed are then reimposed, and the gravitational terms are reintroduced. The parameters ϵ , Fr and U_n are then adjusted to the values required. A detailed description of a similar solution method is given by R04.

6.3 Boundary-layer structure

The small bending resistance of a slender thread means that during steady coiling, bending stress is dynamically important only in thin boundary layers at the nozzle and at the bottom of the thread. This is analogous to the dragged-thread problem that was analysed in chapters 4 and 5. We will again see that bending stress at the bottom of the thread does not deflect the thread very much from vertical, and an argument can be made, as in §4.7, that the boundary layer at the nozzle is negligible at leading order. We therefore omit its effects in the analysis that follows.

The role of bending stress in the boundary layer at the bottom of the thread is to modify the shape so that the boundary conditions (6.2.4) at the contact point are satisfied. We follow the terminology of R04 and refer to this boundary layer as the ‘coil’, and the remainder of the thread above as the ‘tail’. We will see that the ‘coil’ is closely analogous to the ‘heels’ analysed in chapter 4.

In the remainder of this chapter we analyse the leading-order effects of bending stress in the regime $\epsilon \ll 1$ and $U_n \ll 1$, so that the thread is both slender and strongly stretched by gravity. As in chapters 4 and 5, we make a preliminary simplification by omitting the $O(\epsilon^2)$ term in (6.2.1d), which represents only a regular perturbation and has a negligible effect in the asymptotic limit of a very slender thread.

We will use arguments similar to those for the heel at the bottom of a dragged thread in chapter 4 to show that the lengthscale of the coil decreases as $\epsilon \rightarrow 0$. Since U' scales with the axial stress at the bottom of the tail, it remains $O(1)$ (or smaller) and hence there is no significant variation of U in the coil to leading order. We will therefore make the leading-order approximation that U is equal to the coiling speed U_c throughout the coil.

In the sections that follow we analyse the behaviour of the coil in three regimes, namely $\text{Fr} \gg \epsilon^{1/2}$, $\text{Fr} \ll \epsilon \ln \epsilon$ and $\text{Fr} \sim \epsilon \ln \epsilon$, which fall respectively into the inertial, gravitational and inertio-gravitational regimes of R04. (The regime $\epsilon \ln \epsilon \lesssim \text{Fr} \lesssim \epsilon^{1/2}$ also falls into the inertio-gravitational regime, and we briefly discuss this regime in §6.7.) In each regime, the force balance in the coil defines a characteristic lengthscale δ_* . It is convenient to define the rescaled variables

$$\{\eta, \tilde{\mathbf{x}}, \tilde{R}\} = \frac{1}{\delta_*} \{s, \mathbf{x}, R\} \qquad \{\tilde{\Omega}, \tilde{\omega}\} = \frac{\delta_*}{U_c} \{\Omega, \omega\} \qquad (6.3.1a, b)$$

$$\tilde{\mathbf{M}} = \frac{4\delta_*^2}{3\pi a_c^2 \epsilon^2} \mathbf{M} \qquad \tilde{\phi} = \frac{4\delta_*^3}{3\pi a_c^2 \epsilon^2} \mathbf{N}, \qquad (6.3.1c, d)$$

where the rescalings (6.3.1*b-d*) are implied by (6.2.1*b,e,d*) respectively. After making the substitution $\mathbf{U} = U_c \mathbf{d}_3$, the rescaled equations governing the thread in the coil are given by

$$\tilde{\mathbf{x}}' = \mathbf{d}_3 \quad (6.3.2a)$$

$$\mathbf{d}_3' = (\tilde{\omega} - \tilde{\Omega} \mathbf{d}_3) \times \mathbf{d}_3, \quad (6.3.2b)$$

$$\frac{3\epsilon^2}{4\delta_*^4} \tilde{\phi}' = \mathbf{e}_z + \frac{U_c^2 \text{Fr}}{\delta_*} [\tilde{\Omega} \times (\tilde{\Omega} \times \tilde{\mathbf{x}}) + 2\tilde{\Omega} \times \mathbf{d}_3] \quad (6.3.2c)$$

$$\tilde{\mathbf{M}}' = \mathbf{d}_3 \times \tilde{\phi} \quad (6.3.2d)$$

$$\tilde{\mathbf{M}} = \left(\mathbf{I} - \frac{1}{3} \mathbf{d}_3 \mathbf{d}_3\right) \cdot \tilde{\omega}', \quad (6.3.2e)$$

where primes now denote differentiation with respect to η .

We anticipate that $\delta_* \ll 1$ when $\epsilon \ll 1$, and therefore that the asymptotic structure of the coil in the limit of a very slender thread may be derived by replacing (6.2.3) with matching conditions to be imposed towards the tail. As in chapters 4 and 5, these matching conditions must be consistent with the decay of bending and twisting motion in the tail and also with the pinning of the thread at the nozzle where $x = y = 0$. Since U does not appear in (6.3.2), the order of that differential system is one fewer than (6.2.1). While the nozzle is located at rescaled arclength $-\ell/\delta_*$, the matching conditions between the coil and the tail may be applied at any arclength such that $1 \ll -\eta \ll \ell/\delta_*$. The system (6.3.2) is therefore a 15th order system of differential equations, with two unknown parameters $\tilde{\Omega}$ and \tilde{R} . The boundary conditions (6.2.4) are once more imposed at the contact point, and the remaining 7 conditions required to complete the system are obtained by matching.

6.3.1 Twisting motion in the tail

The argument for the neglect of twisting in the tail is similar when we derive matching conditions in §§6.4 and 6.5, and so we briefly discuss it here. In the tail, bending and twisting are dynamically coupled only through (6.2.1*d*), where they are linked through the curvature of the centreline. We assume for the moment that the tail is almost vertical, and hence that its curvature is very small. Twisting motion is then decoupled from bending motion in the tail at leading order. Further, the stress-moment balance (6.2.1*d*) implies that the vertical stress-moment \tilde{M}_z is constant at leading order in the tail since $\mathbf{d}_3 \approx -\mathbf{e}_z$ there. It follows from (6.2.3*i*) that $\tilde{\omega}_z$ varies in the tail between $-\tilde{\Omega}$ at the nozzle (from 6.2.3*i*) and its value $\tilde{\omega}_p$ at the matching point η_p . Hence $\tilde{M}_z = O\left((\tilde{\Omega} - \tilde{\omega}_p)\delta_*/\ell\right)$ in the tail. In contrast, the no-slip boundary condition at the contact point requires that $\tilde{\omega}_3 = 0$ there and hence that there must be an $O(\tilde{\omega}_p)$ change to the rate of twisting across

the coil, which has been rescaled so that its lengthscale is $O(1)$. Hence the twisting-stress moment is $O(\tilde{\omega}_p)$ in the coil, which is far larger than in the tail.

When computing asymptotic solutions numerically we approximate the twisting matching condition by imposing

$$\tilde{M}_z = 0, \quad 1 \ll -\eta \ll \ell/\delta_G, \quad (6.3.3)$$

rather than the actual $O(\tilde{\omega}_p \delta_*/\ell)$ value of \tilde{M}_z . This approximation modifies the amount of twisting that takes place in the tail, but does not affect the coil at leading order.

6.4 Inertia-dominated coiling for $\text{Fr} \gg \epsilon^{1/2}$

We first consider coiling in the regime where bending stress in the coil is balanced by inertial stress. We will show, after rescaling with respect to appropriate stress and length scales in the coil, that there is a unique ‘inertial-coil solution’. This solution is analogous to the unique ‘viscous heel’ in §4.4, and to the inertia-dominated heel formed by a viscous sheet when it falls at high speed onto a moving belt (Dyson, 2007). Bending stress in the coil causes an upward force to be exerted on the tail, which slightly decreases the speed of the thread from its free-fall value before it enters the coil. R04 estimated the radius a_c of the thread in the coil without including the compression at the bottom of the tail. We demonstrate that the compression at the bottom of the tail gives rise to a leading-order correction to this estimate of the coiling speed.

6.4.1 Stress and length scalings

In this regime the stress balance (6.3.2c) is dominated by viscous stress and the centrifugal and Coriolis accelerations. By comparing the appropriate terms in (6.3.2c) and substituting $a_c^2 U_c = 1$ we obtain the stress balance

$$\frac{3\epsilon^2}{4\delta_*^4} \sim \frac{\text{Fr} U_c^2}{\delta_*}, \quad (6.4.1)$$

which implies that the lengthscale of the coil in this regime is

$$\delta_* \sim \delta_i = \left(\frac{3\epsilon^2}{4\text{Fr} U_c^2} \right)^{1/3}. \quad (6.4.2)$$

We note that the $O(\epsilon^{2/3})$ lengthscale of the coil arose previously in §§4.4 and 4.6, where the role of bending stresses was also to support an $O(1)$ stress at the bottom of the tail.

From (6.3.2c), the gravitational stress in the coil is an $O(\delta_i/\text{Fr} U_c^2)$ factor smaller than inertial and viscous stresses. Substitution for δ_i using (6.4.2) implies that gravitational stresses are negligible provided $\epsilon^2 \ll \text{Fr}^4 U_c^8$. We will show in §6.4.3 that the coiling speed U_c is proportional to the free-fall speed U_f . In §3.3 we showed that if $\text{Fr} \ll 1$ then $U_f = O(1)$. The effect of inertia in the tail is to impede the acceleration of the thread, and hence $U_c \lesssim O(1)$ for all values of Fr . Hence inertial stress dominates gravitational stress in the coil only if $\text{Fr} \gg \epsilon^{1/2}$. Provided this holds, we may replace (6.3.2c) by

$$\tilde{\phi}' = \tilde{\Omega} \times (\tilde{\Omega} \times \tilde{\mathbf{x}}) + 2\tilde{\Omega} \times \mathbf{d}_3. \quad (6.4.3)$$

Since $\tilde{\Omega} = \tilde{\Omega} \mathbf{e}_z$ it follows that $\tilde{\phi}'_z = \tilde{\phi}' \cdot \mathbf{e}_z = 0$ and hence that the vertical stress component $\tilde{\phi}_z$ is constant throughout the coil. This simplifies the analysis that follows.

6.4.2 Matching the bending stresses towards the tail

We now turn to the conditions that must be prescribed to the bending motion to allow a smooth matching from the coil towards the tail. As discussed in §6.3, twisting and bending motions are dynamically decoupled in the tail and so we omit the terms that represent twisting in the analysis that follows. We will see that the deflection of the thread from vertical decays exponentially towards the tail (in a similar way as for the compressional heel in §4.4), and hence assume for the moment that $d_{3z} \approx -1$. It follows that the Coriolis acceleration of the tail is negligible compared with the centrifugal acceleration, and hence that the motions in the x and y directions are decoupled at leading order. We will derive matching conditions that enforce the decay of bending motion in the x direction. Similar matching conditions for bending motion in the y direction may also be derived using the same argument. The nozzle is located at $\tilde{x} = \tilde{y} = 0$, and we derive matching conditions by linearising about $\tilde{x} = 0$.

Projection of (6.3.2a,b) onto \mathbf{e}_x and substitution of $d_{3z} \approx -1$ yields

$$\tilde{x}' = d_{3x} \quad (6.4.4a)$$

$$d'_{3x} = -\tilde{\omega}_y. \quad (6.4.4b)$$

Then projection of (6.3.2d,e) onto \mathbf{e}_y and (6.4.3) onto \mathbf{e}_x yields

$$\tilde{M}'_y = \tilde{\phi}_x \quad (6.4.4c)$$

$$\tilde{\omega}'_y = \tilde{M}_y \quad (6.4.4d)$$

$$\tilde{\phi}'_x = -\tilde{\Omega}^2 \tilde{x}. \quad (6.4.4e)$$

Equations (6.4.4) may be combined into a fifth-order ODE for \tilde{x} ,

$$\tilde{x}^{(v)} = -\tilde{\Omega}^2 \tilde{x}, \quad (6.4.5)$$

which represents a balance between bending stress and centrifugal acceleration. Since (6.4.5) is linear in \tilde{x} , the behaviour of the solution as it approaches the tail can be expressed as a superposition of modes, given by

$$\tilde{x} \sim \sum_{i=1..5} A_i \exp(\lambda_i \eta) \quad \text{as } \eta \rightarrow -\infty, \quad (6.4.6)$$

where $\lambda_i^5 = -\tilde{\Omega}^2$ and the A_i are the complex amplitudes of the five modes. Three of these modes diverge as $\eta \rightarrow -\infty$, and must be suppressed in order to allow matching to the tail. Similarly, there are three modes that correspond to bending motion in the y direction that must also be suppressed. Hence the matching conditions from the coil to the tail are

$$\{\tilde{x}, \tilde{y}, d_{3x}, d_{3y}, \tilde{\kappa}_x, \tilde{\kappa}_y\} = O\left(\exp\left(-|\eta| \tilde{\Omega}^{2/5} \cos(\pi/5)\right)\right), \quad |\eta| \gg 1, \quad (6.4.7)$$

neglecting a sinusoidal factor in the right-hand-side for simplicity.

When computing the asymptotic solution for the coil, we approximate these matching conditions by setting the variables in (6.4.7) to zero at some large value of $|\eta|$. The $O(\exp(-|\eta| \tilde{\Omega}^{2/5}))$ error introduced by this approximation is very small. As discussed in §6.3.1, we approximate the matching condition for twisting motion towards the tail by imposing $\tilde{M}_z = 0$.

These 7 matching conditions together with the 10 boundary conditions (6.2.4) at the contact point fully determine the asymptotic solution to (6.3.2) when $\text{Fr} \gg \epsilon^{1/2}$. This solution, which we refer to as an ‘inertial coil’, is unique since all the parameters have been scaled out. Figure 6.2 shows the shape of the inertial coil. Figure 6.3 plots the stress-moment components \tilde{M}_1 , \tilde{M}_2 and \tilde{M}_3 of the inertial coil and compares them to the full numerical solution to (6.2.1)–(6.2.4) for parameter values that are representative of the experiments of Mahadevan *et al.* (1998). There is good agreement.

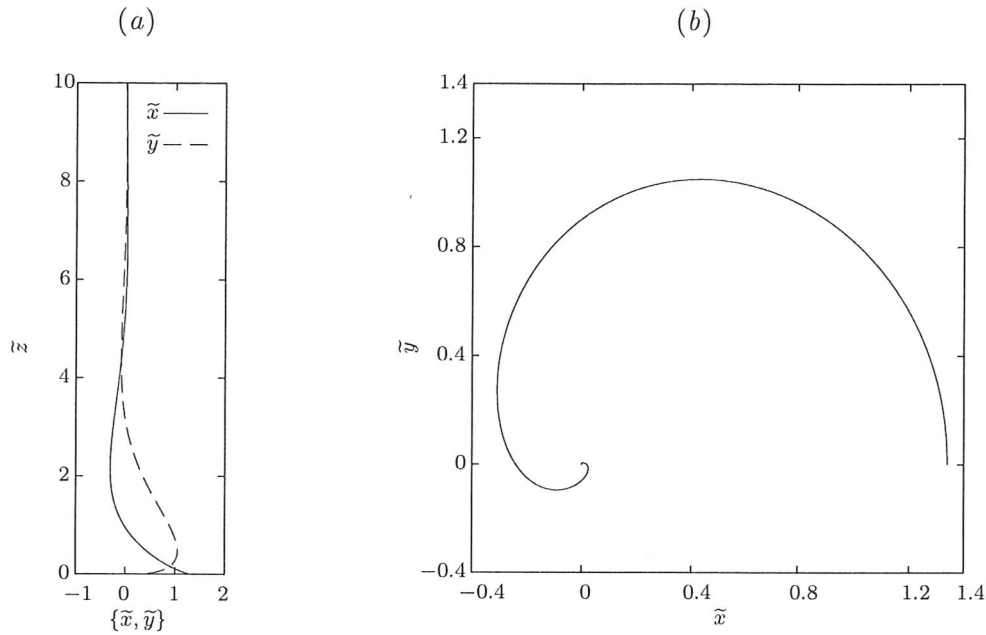


Figure 6.2: The inertial coil, in (a) side and (b) plan views. In the asymptotic limit of a very slender thread, this is the shape taken by a coil when $\text{Fr} \gg \epsilon^{1/2}$.

6.4.3 Estimates of the coiling speed and frequency

The coil exerts a vertical stress on the tail. Using the numerical solution for the unique inertial coil, we find that the vertical force is given by $\tilde{\phi}_z = 1.35$ in rescaled variables, or

$$N_z = 1.35\pi\text{Fr} U_c \quad (6.4.8)$$

in the original dimensionless variables. This value is greater than the momentum flux $F_z = \pi\text{Fr} U_c$ in the tail owing to an axial viscous compression that is generated by bending stress in the coil. The velocity variation in the tail can be derived by solving (3.5.1) subject to $U = U_n$ at the nozzle and the stress condition (6.4.8) at the bottom. The coiling speed U_c can then be estimated by the fall speed at the bottom of the tail.

The numerical solution for the inertial coil yields $\tilde{\Omega} = 0.741$, or

$$\Omega = \frac{0.741 U_c}{\delta_i} = 0.816 \left(\frac{\text{Fr} U_c^5}{\epsilon^2} \right)^{1/3} \quad (6.4.9)$$

in the original dimensionless variables, where (6.4.2) has been substituted for δ_i . The corresponding asymptotic estimate for the coiling radius is then implied by (6.2.4j) to be

$$R = \frac{\delta_i}{0.741} = 1.226 \left(\frac{\epsilon^2}{\text{Fr} U_c^2} \right)^{1/3}. \quad (6.4.10)$$

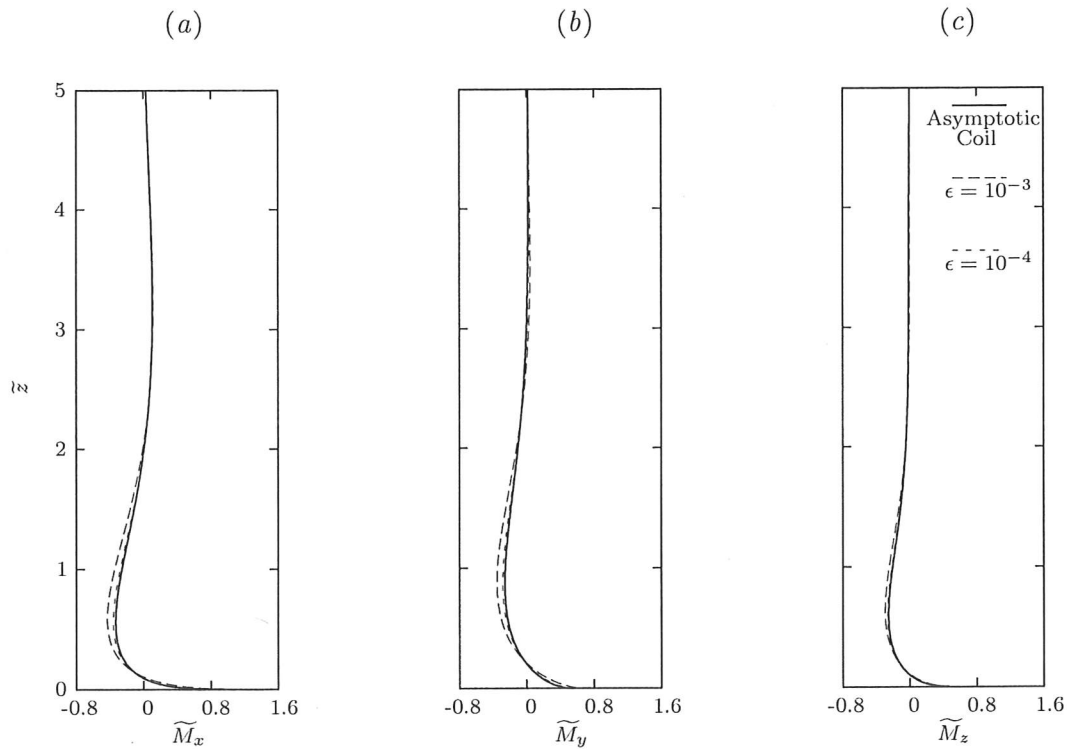


Figure 6.3: The rescaled numerical solution to the full system (6.2.1)–(6.2.4) of coiling equations approaches the inertial-coil solution as ϵ decreases. The variables are scaled according to (6.3.1a,c) with $\delta_i^* = (3\epsilon^2/4\text{Fr} U_c^2)^{1/3}$. The parameter values $\epsilon = 4 \times 10^{-4}$, $\text{Fr} = 26$ and $U_n = 2 \times 10^{-3}$ are representative of experiments performed by Mahadevan et al. (1998). Here the numerical solutions are given for $\epsilon = 10^{-3}$ and 10^{-4} . The inertial-coil solution is almost indistinguishable from the numerical solution for $\epsilon = 10^{-4}$.

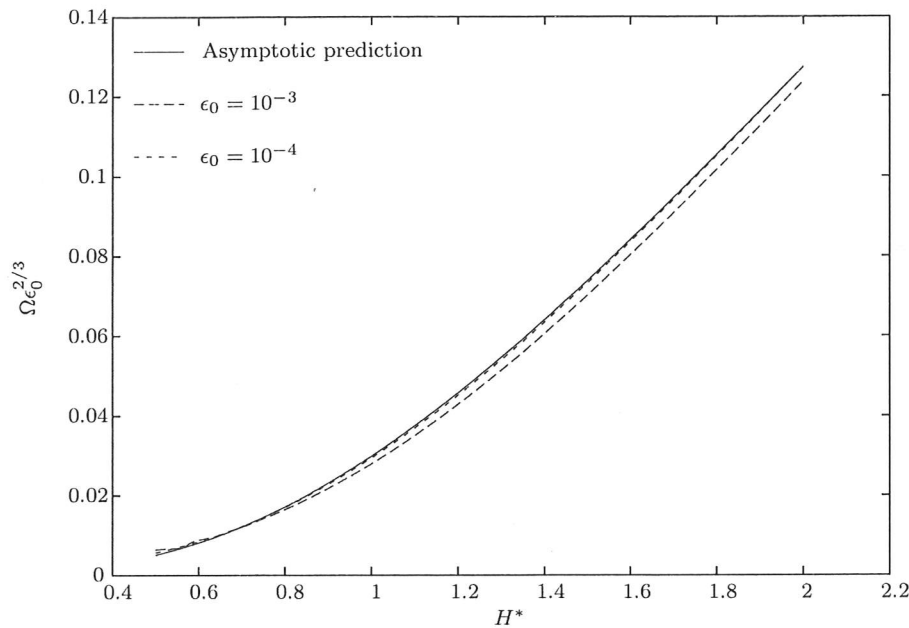


Figure 6.4: Comparison of the coiling frequency obtained from the solution to the full system (6.2.1)–(6.2.4) of coiling equations and the asymptotic estimate (6.4.9). The parameter values used are given by $\epsilon = \epsilon_0/H^{*2}$, $\text{Fr} = 26H^{*3}$ and $U_n = 2 \times 10^{-3}/H^{*2}$, where variations of H^* correspond to variations of the fall height with other experimental parameters fixed. The asymptotic estimate agrees closely with the numerical calculation for $\epsilon_0 = 10^{-4}$.

Figure 6.4 compares the asymptotic estimate (6.4.9) for the coiling frequency with the value calculated from the numerical solution to the full system (6.2.1)–(6.2.4) of coiling equations. To determine the dependence of coiling frequency on the height of fall while holding other experimental parameters at constant values, the parameter values are varied according to $U_n = 2 \times 10^{-3}/H^{*2}$, $\text{Fr} = 26H^{*3}$ and $\epsilon = 10^{-3}/H^{*2}$ and $10^{-4}/H^{*2}$, where H^* ranges between 0.5 and 2 and represents a variation of the fall height while all other parameters are held fixed. The parameter values when $H^* = 1$ are representative of the experiments of Mahadevan *et al.* (1998).

6.4.4 Stress exerted by the coil

In the experiments of Mahadevan *et al.* (1998), though inertia is dominant in the coil, Fr is small enough that inertia does not dominate viscous stress in the tail. For these experiments the compressive stress exerted by the coil is accommodated by a global modification to the velocity variation in the tail, in a similar way to that described in §3.4.1. However if $\text{Fr} \gg 1$ then the fall of the thread is dominated by an inertia–gravity balance everywhere except for thin boundary layers near the nozzle and near the bottom of the thread. The analysis in §3.5.2 shows that the stress condition (6.4.8) results in a significant deceleration

at the bottom of the thread, on a lengthscale that is greater than that of the coil but less than that of the tail. By substituting $\alpha = 0.35$ into (3.5.8), we find that U_c is related to the free-fall speed U_f by

$$U_c = \frac{U_f}{1.35}. \quad (6.4.11)$$

R04 estimated the radius of the thread in the coil by solving (3.5.1) subject to $U = U_n$ at the nozzle and the condition that there is no stretching at the bottom of the tail so that $U' = 0$ there. This corresponds to setting $\alpha = 0$ in (3.5.8), and when $\text{Fr} \gg 1$, the resulting estimate for the coiling speed is $U_c = \sqrt{2/\text{Fr}}$. From (6.4.11), we obtain $U_c = \sqrt{1.481/\text{Fr}}$ which differs from Ribe's estimate since we have shown that, although the compressional region at the bottom of the tail is thin, there is nonetheless a significant variation in velocity across it.

To demonstrate the effect of the compressional region for $\text{Fr} \gg 1$, we calculate the velocity variation in the thread for parameter values $\text{Fr} = 208$, $U_n = 5 \times 10^{-4}$, and $\epsilon = 2.5 \times 10^{-4}$ and 2.5×10^{-5} . These correspond to the experiments of Mahadevan *et al.* (1998) except with a height of fall that is twice as large. Figure 6.5 shows the variation in speed along the thread calculated using the full system (6.2.1)–(6.2.4) of coiling equations. The asymptotic estimate of the velocity variation, obtained by solving the extensional-flow equation (3.5.1) subject to $U = 10^{-3}$ at $s = -1$ and the stress condition (6.4.8), gives very good agreement with the solution to the full system.

R04 remarked that solving (3.5.1) subject to there being no stretching at the bottom of the tail (and with a small $O(R)$ modification to the fall height) typically introduces an error of around 5 per cent in the radius in the coil, compared with that predicted by solving the full system (6.2.1)–(6.2.4). Since $U_c = 1/a_c^2$, this means that the size of this error would equate to an error of around 10 per cent in the estimated coiling speed. Figure 6.6 shows the coiling speed predicted by solving the full system (6.2.1)–(6.2.4) of coiling equations and compares it with the estimates obtained by solving (3.5.1) for the velocity variation in the tail, subject to the velocity condition (3.3.2) at the nozzle and the stress condition (3.5.4) at the bottom with $\alpha = 0.35$ and $\alpha = 0$. The parameter values used are the same as those used in figure 6.4. While the error introduced by making the approximation $\alpha = 0$ is only around 10 per cent for $H^* \lesssim 1$, it is around 20 per cent for the larger fall heights considered here. The asymptotic estimate with $\alpha = 0.35$ clearly improves on that of R04, particularly for larger fall heights.

The asymptotic estimate neglects gravitational effects in the coil and, as described in §6.4.1, is valid provided $\epsilon^2 \ll \text{Fr}^4 U_c^8$. When $H^* = 0.5$, the numerical values of the parameters are $\epsilon = 4 \times 10^{-4}$, $\text{Fr} \approx 4$ and $U_c \approx 10^{-1}$. For these values $\epsilon^2 \sim \text{Fr}^4 U_c^8$, and hence inertial effects do not dominate gravitational effects. The use of the inertial-coil solution to estimate the coiling speed is therefore inappropriate when $H^* \lesssim 0.5$.

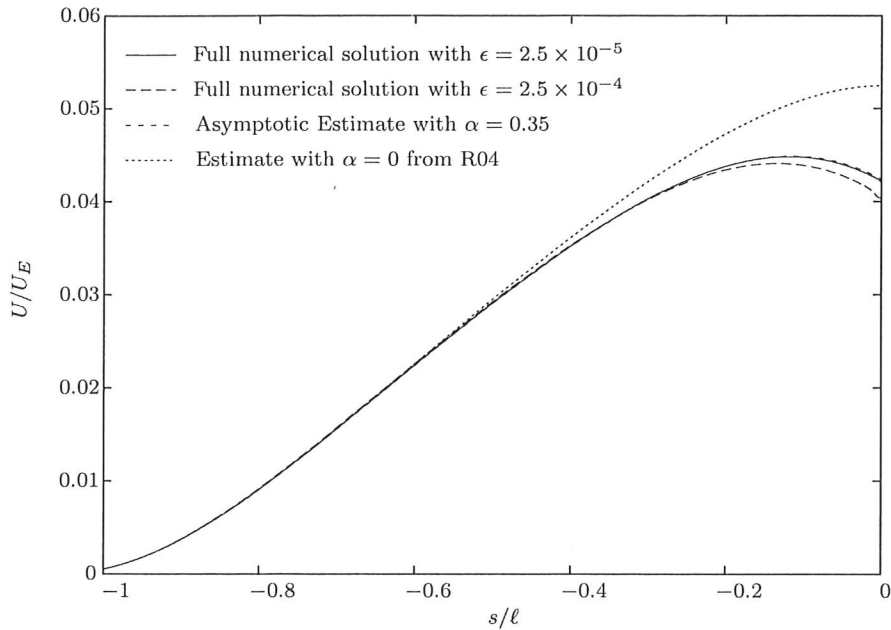


Figure 6.5: The velocity variation in the tail predicted by solving the extensional-flow equation (3.5.1), subject to $U = 10^{-3}$ at $s = -1$ and (3.5.4) with $\alpha = 0.35$, is in good agreement with the solution to the full system (6.2.1)–(6.2.4) of coiling equations for $\epsilon \approx 2.5 \times 10^{-4}$ and $\epsilon \approx 2.5 \times 10^{-5}$. The velocity profile obtained by instead using $\alpha = 0$ omits the compressive force exerted on the tail by the coil.

6.5 Gravity-dominated coiling for $\text{Fr} \ll \epsilon \ln \epsilon$

We now consider coiling in the regime where inertia is negligible everywhere in the thread, so that the motion of both the tail and the coil are governed by a gravity–viscosity balance. We neglect the effects of inertia entirely by setting $\text{Fr} = 0$. We will return to the effects of inertia in §6.6, where we show that the results obtained in this section are valid provided $\text{Fr} \ll \epsilon \ln \epsilon$.

In this regime, the bending stress in the coil does not need to support much axial compression since most of the weight of the tail is supported by extensional stress and the momentum flux is negligible. The bending stress in the coil causes a horizontal force to be exerted on the tail. The tail behaves like a catenary, and hence a small force exerted at the bottom results in a logarithmically large displacement at the bottom of the tail. This will in turn affect the coiling radius since the coil must match smoothly onto the tail. We will show that analysis of this interaction between the coil and the tail yields a quantitative prediction for the coiling frequency which includes a (square-root logarithmic) leading-order correction to previous scaling estimates.

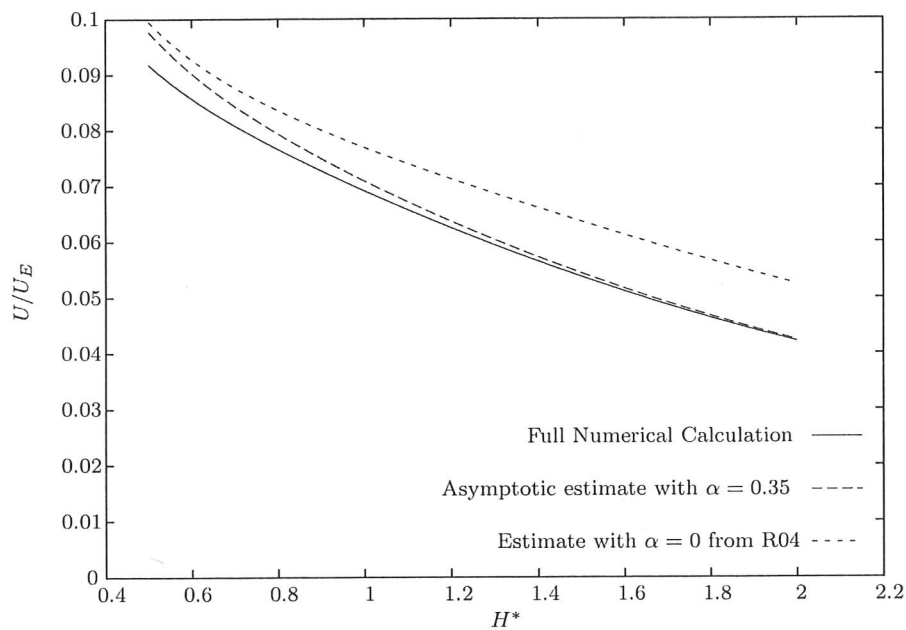


Figure 6.6: The coiling speed estimated by solving (3.5.1) subject to (3.3.2) and (3.5.4) with $\alpha = 0.35$ agrees well with the speed predicted by the solution to the full problem (6.2.1)–(6.2.4). The parameter values used are $\epsilon \approx 10^{-4}/H^{*2}$, $Fr = 26H^{*3}$ and $U_n = 2 \times 10^3/H^{*2}$, where variations in H^* correspond to variations in the fall height while all other parameters are fixed. The prediction obtained using $\alpha = 0$ rather than $\alpha = 0.35$ significantly overestimates the coiling speed due to the neglect of the compressive force exerted on the tail by the coil.

6.5.1 Stress and length scalings

Since the stress balance (6.3.2c) in this regime is dominated by a balance between viscous and gravitational stress, we compare the corresponding terms to obtain the balance

$$\frac{3\epsilon^2}{4\delta_*^4} \sim 1, \quad (6.5.1)$$

which implies that the lengthscale of the coil in this regime is

$$\delta_* \sim \delta_g = \left(\frac{3\epsilon^2}{4} \right)^{1/4}. \quad (6.5.2)$$

We note that this scaling is identical to that derived in §4.5, and also to the lengthscale obtained by R04 for coiling in this regime.

Since inertia is negligible, the stress balance (6.3.2c) implies that the rescaled horizontal stress components $\tilde{\phi}_x$ and $\tilde{\phi}_y$ are constant in the coil. This simplifies the analysis that follows.

6.5.2 Matching the bending stress towards the tail

As discussed in §6.3.1, twisting is decoupled from bending in the tail and we can again omit the dynamic effects of twisting in the following discussion of matching conditions. As in §6.4, the thread is almost vertical in the matching region and the motions in the x and y directions are decoupled from each other at leading order.

We follow a similar process to the derivation of matching conditions for the gravitational heel in §4.5. From (6.3.2e), $\tilde{M}_y = \tilde{\omega}_y$ at leading order, and we substitute this into (6.3.2d) and then project onto \mathbf{e}_y to obtain

$$\tilde{\omega}_y'' = \tilde{\phi}_x d_{3z} - \tilde{\phi}_z d_{3x}. \quad (6.5.3)$$

In the tail, $\mathbf{d}_3 \approx -\mathbf{e}_z$ and (6.3.2c) implies that the vertical stress component is given by $\tilde{\phi}_z \sim \eta + \eta_0$, where η represents the rescaled weight of the thread and η_0 is an offset due to the vertical force exerted by bending stress in the coil. Projection of (6.3.2b) onto \mathbf{e}_x and omission of twisting yields $\tilde{\omega}_y \sim -d'_{3x}$. Hence

$$d'''_{3x} \sim (\eta + \eta_0)d_{3x} + \tilde{\phi}_x, \quad 1 \ll -\eta \ll \frac{\ell}{\delta_g}. \quad (6.5.4)$$

The solution approaches

$$d_{3x} \sim -\frac{\tilde{\phi}_x}{\eta + \eta_0} + \sum_{i=1,2,3} A_i \exp\left(-\frac{3}{4}\lambda_i \eta^{4/3}\right), \quad 1 \ll -\eta \ll \frac{\ell}{\delta_g}, \quad (6.5.5)$$

where $\lambda_i^3 = -1$ and the A_i are the complex amplitudes of the three exponential modes. The first term on the right-hand side of (6.5.5) is a leading-order particular integral and the exponential modes are WKB approximations to the complementary function (neglecting an algebraic factor in the amplitude for simplicity).

As in §4.5, there are two bending modes in the x direction that do not decay towards the tail. There are two similar modes that represent bending in the y direction. All four of these modes are suppressed by imposing the matching conditions

$$d_{3x} \sim -\frac{\tilde{\phi}_x}{\phi_z}, \quad d_{3y} \sim -\frac{\tilde{\phi}_y}{\phi_z}, \quad d'_{3x} \sim \frac{\tilde{\phi}_x}{\phi_z^2}, \quad d'_{3y} \sim \frac{\tilde{\phi}_y}{\phi_z^2}, \quad 1 \ll -\eta \ll \frac{\ell}{\delta_g}, \quad (6.5.6 a-d)$$

where we have substituted $\eta + \eta_0 = \tilde{\phi}_z$.

Together with the matching condition $\tilde{M}_z = 0$ for twisting motion towards the tail, the conditions (6.5.6) prescribe the bending and twisting motion in the coil that matches smoothly onto the tail. The remaining two conditions required to complete the system must be consistent with the pinning of the thread at the rescaled position $(0, 0, \delta_g^{-1})$ of the nozzle.

6.5.3 Pinning of thread at the nozzle

The tail is governed by a balance between hoop stress and gravity, and it is pulled sideways from beneath the nozzle by bending forces in the coil. The horizontal stress components are constant throughout the thread, and so the tail lies in a plane at leading order. To be consistent with the condition that the thread is pinned at the nozzle, this plane must pass through $\tilde{x} = \tilde{y} = 0$. Hence the tangent \mathbf{d}_3 to the thread satisfies

$$\tilde{x}d_{3y} - \tilde{y}d_{3x} = O\left(\exp\left(\frac{3}{4}\eta^{4/3}\right)\right), \quad 1 \ll -\eta \ll \frac{\ell}{\delta_g}, \quad (6.5.7)$$

where the right-hand side represents the exponentially decaying bending mode in (6.5.5).

The condition (6.5.7) imposes the direction but not the magnitude of the tail's deflection. As discussed in §3.4.2, for a given force exerted on the tail we can obtain the leading-order deflection at the bottom of the tail by making the approximation that the thread

has constant radius in the tail. From (3.4.15) with rescaled force $\tilde{\phi}_h = F_h/\pi a_c^2 \delta_g$ and displacement $\tilde{x}_h = x_t/\delta_g$, we obtain

$$\tilde{x}_h(\eta) \sim \tilde{\phi}_h \ln \left(\frac{\tan(\theta_n/2)}{\tan(\theta/2)} \right), \quad 1 \ll -\eta \ll \ell/\delta_g,$$

where $\theta(\eta)$ is the deflection from vertical at rescaled arclength η and θ_n is the deflection from vertical that the tail would have if it were extrapolated upwards to the nozzle while the thread radius is fixed. By integrating (3.4.14) and again substituting $\tilde{\phi}_h = F_h/\pi a_c^2 \delta_g$, this angle is given at leading order by $\theta_n = \tilde{\phi}_h \delta_g/\ell$, while $\theta = \tilde{\phi}_h/|\eta|$. Substituting these into the above expression gives

$$\tilde{x}_h \sim \tilde{\phi}_h \ln \left(\frac{\ell}{\delta_g \eta} \right), \quad 1 \ll -\eta \ll \ell/\delta_g. \quad (6.5.8)$$

The conditions (6.5.7) and (6.5.8) complete the seven matching conditions that together with the boundary condition (6.2.4) close the system (6.3.2).

We will see that the coiling radius \tilde{R} is large when $\delta_g \ll 0$, and that the rescaled length ℓ/δ_g is even larger, with a square-root logarithmic scale separation \tilde{R} and ℓ/δ_g as $\delta_g \rightarrow 0$. Hence in this limit, resolving both the behaviour of the coil and of the tail introduces a very large computational cost. To avoid this difficulty we instead use a solution computed over a truncated domain by applying the matching conditions derived above at arclength $\eta = -10$. Figure 6.7 shows the agreement between the solutions computed on this truncated domain and those computed by instead applying the nozzle boundary conditions (6.2.3a–i) at rescaled height $\tilde{z} = 34$ and 340. These heights correspond to the parameter values $\epsilon = 10^{-3}$ and 10^{-5} . There is very good agreement, which might be expected since the errors introduced by imposing the matching conditions decay exponentially towards the tail. The use of the truncated solutions to determine the solution structure in the asymptotic limit $\epsilon \rightarrow 0$ is therefore justified.

6.5.4 Asymptotic structure of the coil for $0 < \epsilon \ll 1$

We now analyse the behaviour of gravity-dominated coiling in the asymptotic limit of an extremely slender thread. Figure 6.8 shows plan views of coils calculated using the truncated solution as described in §6.5.3, for $\delta_g = 10^{-2}$, 10^{-8} and 10^{-16} . These solutions suggest that as $\delta_g \rightarrow 0$, or equivalently $\epsilon \rightarrow 0$, the dominant contribution to the coiling radius is from the deflection of the tail, and that the direction in which the tail is deflected approaches the x axis. We will see that this is because the $O(\tilde{\phi}_h \ln \delta_g)$ displacement of the tail implied by (6.5.8) is asymptotically larger (just) than the axial lengthscale of the coil, which remains $O(1)$ by the choice of scaling made here.

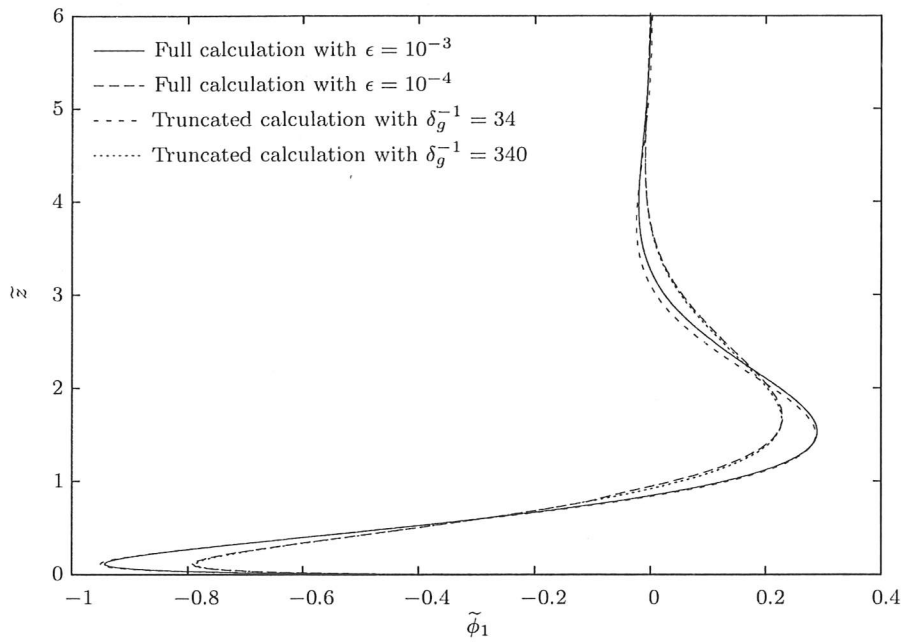


Figure 6.7: The solutions that are computed for the truncated thread are almost identical to the solutions to the full system (6.2.1)–(6.2.4). Here the stress component $\tilde{\phi}_1$ is plotted for $\epsilon = 10^{-3}$ and 10^{-5} and the truncated solution is obtained by applying the matching conditions (6.3.3) and (6.5.6)–(6.5.8) at rescaled arclength $\eta = -10$. The solutions agree to within the width of the line when $\epsilon \lesssim 10^{-5}$.

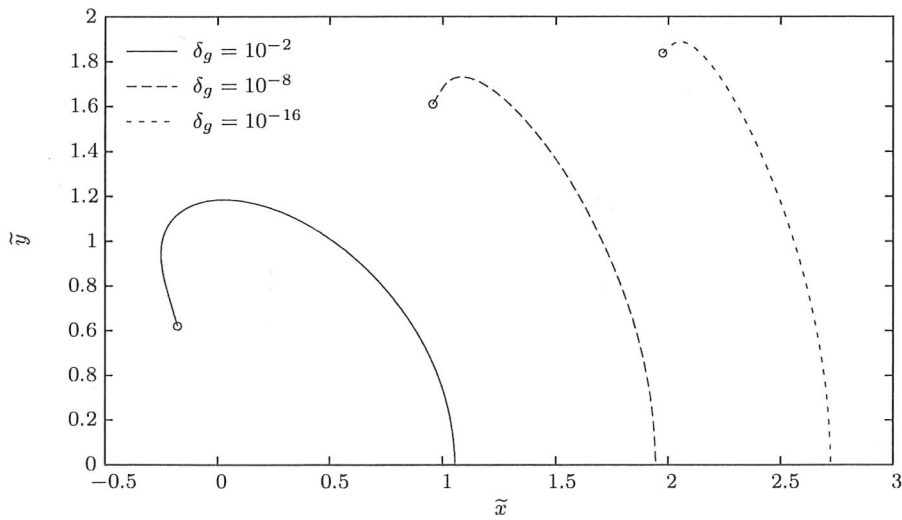


Figure 6.8: Plan views of gravitational coils, calculated for $\delta_g = 10^{-2}$, 10^{-8} and 10^{-16} using the truncated solution. The solutions were truncated at $\eta = -10$ and the truncation points are circled. As $\delta_g \rightarrow 0$, the coiling radius increases and the direction in which the tail is deflected approaches the positive x axis, but only very slowly due to a dependence on $\ln \delta_g$.

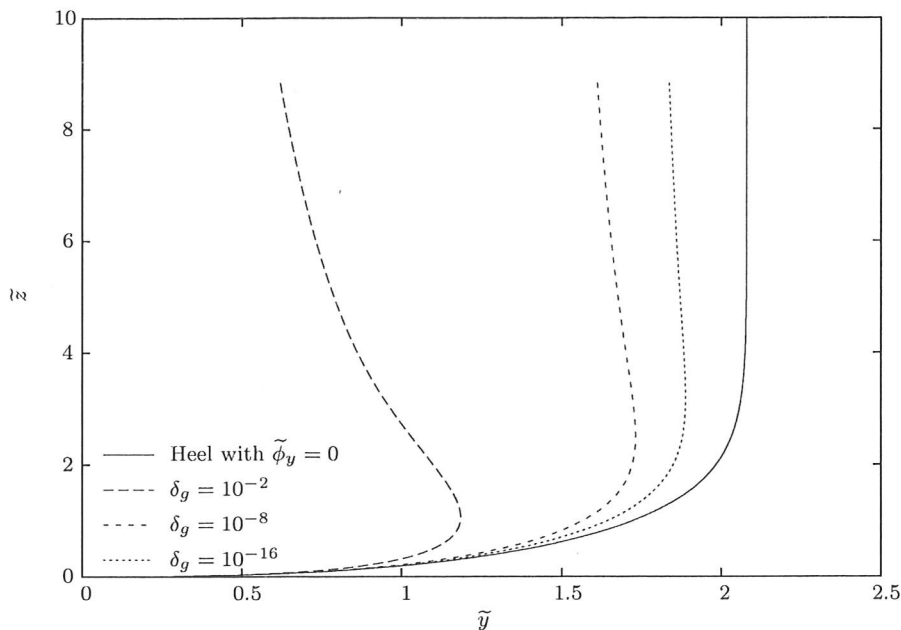


Figure 6.9: Side views of gravitational coils, calculated for $\delta_g = 10^{-2}$, 10^{-8} and 10^{-16} using the truncated solution. The shape of the thread when viewed from the side approaches that of the gravitational heel (analysed in §4.5) for which $\tilde{\phi}_y = 0$ and $\tilde{\Phi}_z = 0.82$.

We now show that at leading order, the coil behaves as a heel in the y - z plane that is perturbed by a small force in the x direction. The plan view of the coils in figure 6.8 suggests that while the total x -displacement of the contact point increases as $\delta_g \rightarrow 0$, the contribution from the coil decreases. In contrast, the y -component of displacement in the coil appears to remain $O(1)$ as $\delta_g \rightarrow 0$. This suggests that at leading order, the coil is simply a two-dimensional heel that rolls in the y direction with velocity $U_c \mathbf{e}_y$. It is prevented from rolling indefinitely in that direction by a small restoring force $\tilde{\phi}_x$ applied in the x direction, and we analyse the consequent (small) correction below. Figure 6.8 also shows that the orientation of the tail approaches the x axis, and we therefore expect that $\tilde{\phi}_y$ is even smaller than $\tilde{\phi}_x$ and hence that the two-dimensional heel in the y - z plane will have $\tilde{\phi}_y = 0$ at leading order. Figure 6.9 shows truncated coil solutions viewed from the x direction, and demonstrates their approach towards the two-dimensional heel (obtained in §4.5) for which $\tilde{\phi}_y = 0$ and $\tilde{\Phi}_z = 0.82$.

We now analyse the effect of the small force in the x direction on a heel in the y - z plane. The variables that govern the unperturbed heel are \tilde{y} , \tilde{z} , d_{3y} , d_{3z} , $\tilde{\omega}_x$, \tilde{M}_x , $\tilde{\phi}_y$ and $\tilde{\phi}_z$; the equations that govern their variation in the heel are obtained through expansion of (6.3.2), and are

$$\tilde{y}' = d_{3y} \quad \text{and} \quad \tilde{z}' = d_{3z} \quad (6.5.9a,b)$$

$$d'_{3y} = -\tilde{\omega}_x d_{3z} + O(\tilde{\phi}_x^2) \quad \text{and} \quad d'_{3z} = \tilde{\omega}_x d_{3y} + O(\tilde{\phi}_x^2), \quad (6.5.9c,d)$$

$$\tilde{\omega}'_x = \tilde{M}_x + O(\tilde{\phi}_x^2) \quad \text{and} \quad \tilde{M}'_x = \tilde{\phi}_y + O(\tilde{\phi}_x^2) \quad (6.5.9e,f)$$

$$\tilde{\phi}'_y = 0 \quad \text{and} \quad \tilde{\phi}'_z = 1 + O(\tilde{\phi}_x^2). \quad (6.5.9g,h)$$

The $O(\tilde{\phi}_x^2)$ terms are higher-order perturbations due to the coupling of motion in the x and y directions by rotation of the thread in the coil. The boundary and matching conditions applied to these variables are obtained through expansion of the boundary conditions (6.2.4b,c,e-g) and matching conditions (6.5.6b,d). This gives

$$\tilde{y} = \tilde{z} = d_{3z} = \omega_x = 0 \quad \text{and} \quad d_{3y} = -1 \quad \text{at} \quad \eta = 0 \quad (6.5.10a-e)$$

$$d_{3y} \sim -\frac{\tilde{\phi}_y}{\eta} \quad \text{and} \quad d'_{3y} \sim \frac{\tilde{\phi}_y}{\eta^2}, \quad 1 \ll -\eta \ll \frac{\ell}{\delta_g}. \quad (6.5.10f,g)$$

The system of equations (6.5.9) and (6.5.10) is equivalent to the equation (4.5.2), subject to (4.2.9f-i) and (4.5.11), that describes the motion of a gravitational heel formed when a thread is dragged by a moving belt; the solution is therefore a gravitational heel in the y - z plane.

The heel is perturbed out of the y - z plane by the restoring force $\tilde{\phi}_x$. The remaining variables are thus $O(\tilde{\phi}_x)$. The equations governing them are obtained at leading order through linearisation of (6.3.2) about the heel in the y - z plane, and are

$$(\tilde{x} - \tilde{R})' = d_{3x} \quad \text{and} \quad d'_{3x} = \tilde{\omega}_y d_{3z} - \tilde{\omega}_z d_{3y} \quad (6.5.11a,b)$$

$$\tilde{\omega}'_y = \tilde{M}_y + \frac{1}{3}\tilde{\omega}'_3 d_{3y} \quad \text{and} \quad \tilde{\omega}'_z = \tilde{M}_z + \frac{1}{3}\tilde{\omega}'_3 d_{3z} \quad (6.5.11c,d)$$

$$\tilde{M}'_y = \tilde{\omega}_z \tilde{\phi}_x - \tilde{\omega}_x \tilde{\phi}_z \quad \text{and} \quad \tilde{M}'_z = \tilde{\omega}_x \tilde{\phi}_y - \tilde{\omega}_y \tilde{\phi}_x \quad (6.5.11e,f)$$

$$\tilde{\phi}'_x = 0, \quad (6.5.11g)$$

where the twist rate

$$\tilde{\omega}_3 = \tilde{\omega}_x d_{3x} + \tilde{\omega}_y d_{3y} + \tilde{\omega}_z d_{3z}$$

is also an $O(\tilde{\phi}_x)$ variable. The boundary and matching conditions applied to the perturbation variables are obtained through linearisation of (6.2.4a,c,h-i) and (6.5.6a,c), and

are

$$(\tilde{x} - \tilde{R}) = d_{3x} = \tilde{\omega}_y = 0 \quad \text{and} \quad \tilde{\omega}_z = -\tilde{\Omega} \quad \text{at} \quad \eta = 0 \quad (6.5.12a-d)$$

$$d_{3x} \sim -\frac{\tilde{\phi}_x}{\eta}, \quad d'_{3x} \sim \frac{\tilde{\phi}_x}{\eta^2}, \quad \text{and} \quad \tilde{M}_z = 0, \quad 1 \ll -\eta \ll \frac{\ell}{\delta_g}. \quad (6.5.12e-g)$$

(The approximated matching condition (6.5.12g) introduces only an $O(\delta_g/\ell)$ error which is negligible compared to the leading-order perturbation to the heel.)

Equations (6.5.11) and (6.5.12) are a linear system of equations, whose only inhomogeneity is the non-zero right-hand-side in (6.5.12d). It follows that the entire solution is proportional to $\tilde{\Omega}$ and in particular that the (constant) stress component $\tilde{\phi}_x$ satisfies $\tilde{\phi}_x \propto \tilde{\Omega}$. The matching condition (6.5.8) implies that $\tilde{R} \sim \tilde{\phi}_h \ln \delta_g$ at leading order. Combining these results and $\tilde{\Omega}\tilde{R} = 1$, we obtain

$$\tilde{R} = O\left(\sqrt{\ln \delta_g}\right) \quad \text{and} \quad \tilde{\phi}_x = O\left(\frac{1}{\sqrt{\ln \delta_g}}\right). \quad (6.5.13a,b)$$

The above analysis has shown that at leading order the coil behaves like a heel in the y - z plane. We have rescaled variables with respect to the axial lengthscale of the coil, and the coil therefore gives an $O(1)$ contribution to the displacement $\tilde{R}\mathbf{e}_x$ of the contact point from underneath the nozzle. Hence (6.5.13a) justifies the earlier assumption that the tail gives the dominant contribution to \tilde{R} in the asymptotic limit $\delta_g \rightarrow 0$. At leading order, $\tilde{\phi}_h = \tilde{\phi}_x$ and so (6.5.13b) justifies the earlier assumption that $\tilde{\phi}_h \rightarrow 0$ as $\delta_g \rightarrow 0$.

6.5.5 Estimates of the coiling frequency and radius

The dependence of the coiling radius on δ_g may now be obtained at leading order by solving (6.5.9)–(6.5.12) numerically to determine the constant of proportionality between $\tilde{\phi}_x$ and $\tilde{\Omega}$. At leading order, the motion in the x direction is a perturbation to the heel in the y - z plane with $\tilde{\Phi}_z = 0.82$. Numerical solution of (6.5.11) and (6.5.12) for this heel yields

$$\tilde{\phi}_x = 0.198\tilde{\Omega} + O(\tilde{\Omega}^2). \quad (6.5.14)$$

From (6.5.14), the leading-order relationship $\tilde{R} \sim \tilde{\phi}_x \ln \delta_g$ and the relationship $\tilde{R}\tilde{\Omega} = 1$, we obtain $\tilde{R} = \sqrt{0.198 \ln \delta_g} + O(1)$ in the rescaled variables, or

$$R = \delta_g \sqrt{0.198 \ln \delta_g} + O(\delta_g) \quad \text{and} \quad \Omega = \frac{U_c}{\delta_g} \sqrt{\frac{5.044}{\ln \delta_g}} + O\left(\frac{U_c}{\delta_g \ln \delta_g}\right) \quad (6.5.15a,b)$$

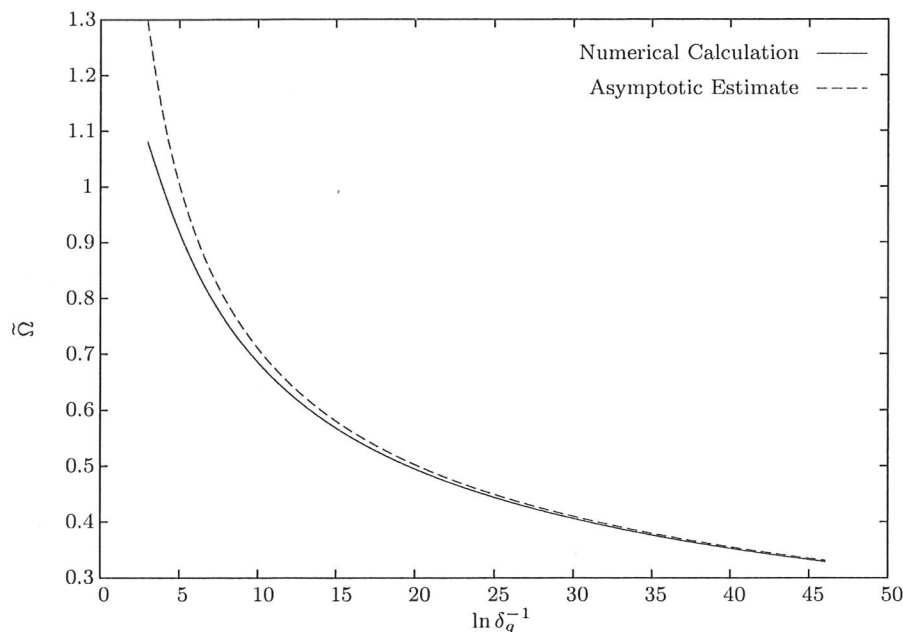


Figure 6.10: The asymptotic estimate $\tilde{\Omega} \sim \sqrt{5.044/\ln \delta_g}$ for the coiling frequency approaches the value obtained using the truncated coil solution as $\delta_g \rightarrow 0$. Values of δ_g representative of experiment range between 10 and 150, corresponding to $2.3 \leq \ln \delta_g^{-1} \leq 5.0$, and for these values the asymptotic prediction is accurate to within 20 per cent.

in the original dimensionless variables. Figure 6.10 compares the asymptotic estimate (6.5.15b) for $\tilde{\Omega}$ with the value obtained using the truncated numerical solution described in §6.5.3. The asymptotic estimate converges towards the numerical solution as $\delta_g \rightarrow 0$, albeit very slowly due to the logarithmic nature of the higher-order correction terms. Typical values of δ_g^{-1} encountered in experiments range between 10 and 150 and for these values the leading-order approximation is accurate to within 20 per cent.

As for the gravitational heel in §4.5, the behaviour of the coil depends on the speed U_c at the bottom of the thread. Since bending stress in the coil does not compress the tail very much, we may again estimate the coiling speed U_c by the free-fall speed U_f calculated in §3.3. The leading-order estimate for the dimensional coiling frequency is therefore

$$\Omega = \frac{U_E}{H} \frac{2U_f}{3^{1/4}} \left(\frac{5.044}{\epsilon \ln \epsilon} \right)^{1/2}. \quad (6.5.16)$$

Figure 6.11 compares this asymptotic prediction to the solution to the full system (6.2.1)–(6.2.4) of coiling equations for parameter values $\epsilon \lesssim 10^{-2}$, $U_n = 10^{-3}$ and $\text{Fr} = \Gamma = 0$. The leading-order estimate $U_f = 0.078$ was obtained using (3.3.6). Typical values of ϵ encountered in experiment range between 10^{-4} and 10^{-2} , which corresponds to values of δ_g between 10 and 100, and for this range (6.5.16) is accurate to within 20 per cent, despite the very slow logarithmic decay of the higher-order terms that have been omitted.

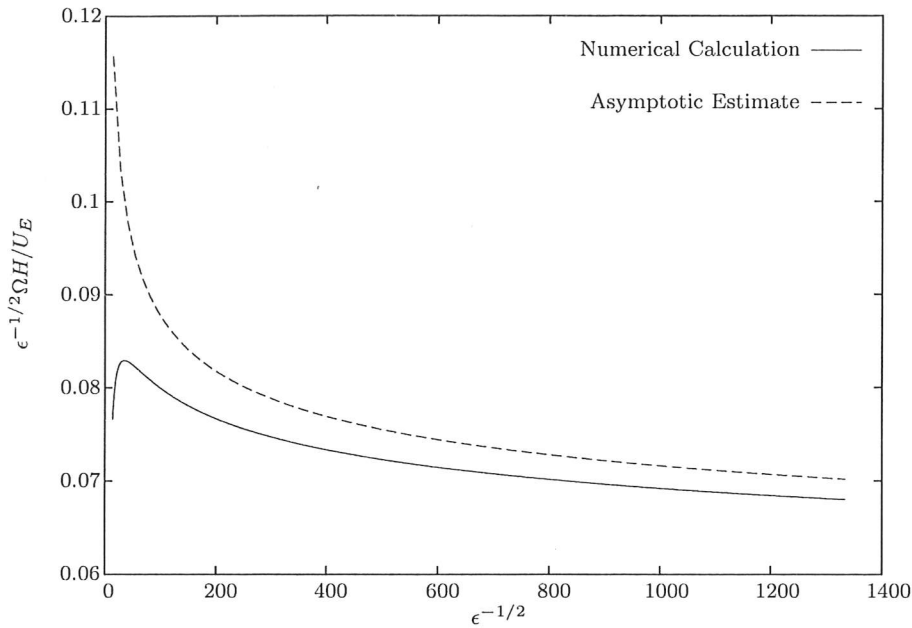


Figure 6.11: The asymptotic estimate (6.5.16) for the coiling frequency Ω of an extensible viscous thread agrees reasonably well with the value obtained from the full numerical solution to (6.2.1)–(6.2.4), for parameter values $Fr = \Gamma = 0$ and $U_n = 10^{-3}$.

6.6 Inertio-gravitational coiling for $Fr \sim \epsilon \ln \epsilon$

The analysis in §6.5 is valid only if inertia is negligible compared to gravity both in the coil and in the tail. R06b demonstrated that for a narrow range of fall heights, the thread exhibits a resonant behaviour when the coiling frequency is close to one of the eigenfrequencies Ω_n of a free circular pendulum. In §3.6 we analysed the behaviour of a forced circular pendulum, and showed that away from resonance the dominant balance involves the hoop stress and the centrifugal acceleration of the thread. From (3.6.4), the centrifugal acceleration of the tail is negligible compared to hoop stress provided $\Omega^2 Fr \ll 1$, which from (6.5.15b) requires

$$Fr \ll \delta_g^2 \ln \delta_g \sim \epsilon \ln \epsilon. \quad (6.6.1)$$

When $Fr \sim \delta_g^2 \ln \delta_g$, centrifugal acceleration is comparable with hoop stress in the tail. If the thread is very slender, then $\delta_g \ll 1$. It thus follows that $Fr \ll 1$ and the axial momentum flux remains negligible compared with the extensional stress in the tail. In this section we try to understand in more detail the dynamic interaction between the coil and the tail in this regime. We will see that while centrifugal acceleration changes the behaviour of the tail, the coil remains unaffected provided the coiling frequency does not excite an eigenmode of the tail. Bending stress in the coil causes a force to be exerted at the bottom of the tail, and we will obtain a prediction for the behaviour of the thread by modelling the tail as a weakly forced circular pendulum.

6.6.1 Stress and length scalings

R06b suggested that in the inertio-gravitational regime, inertia is negligible in the coil provided the coiling frequency is not close to one of the eigenfrequencies of a free thread. This motivates us to reuse the lengthscale δ_g , given by (6.5.2) and appropriate for coils that are dominated by a viscosity-gravity balance. The rescaled stress balance (6.3.2c) is then given by

$$\tilde{\phi}' = \mathbf{e}_z + \frac{U_c^2 \text{Fr}}{\delta_g} [\tilde{\Omega} \times (\tilde{\Omega} \times \tilde{\mathbf{x}}) + 2\tilde{\Omega} \times \mathbf{d}_3]. \quad (6.6.2)$$

We assume for the moment that the coil remains unchanged by inertia, and hence from (6.5.15b) that $\tilde{\Omega} = O(1/\delta_g \sqrt{\ln \delta_g})$ and $\tilde{\phi}_h = O(1/\sqrt{\ln \delta_g})$. Since $\text{Fr} \ll 1$, the fall speed is governed by extensional flow in the tail. There is negligible velocity variation in the coil and hence $U_c = \tilde{\Omega} \tilde{R}$ is $O(1)$ as $\delta_g \rightarrow 0$. The horizontal displacement $\tilde{\mathbf{x}}$ scales like \tilde{R} and the inertial terms in (6.6.2) are therefore $O(\text{Fr} \tilde{\Omega}/\delta_g)$. The total change in $\tilde{\phi}_h$ across the coil may be obtained through integration of (6.6.2) over the $O(1)$ axial lengthscale of the coil. Hence the change in $\tilde{\phi}_h$ across the coil is $O(\text{Fr} \tilde{\Omega}/\delta_g)$, and is much smaller than the $O(1/\sqrt{\ln \delta_g})$ bending stress in the coil provided $\text{Fr} = O(\delta_g^2 \ln \delta_g)$ and $\tilde{\Omega}$ is not too close to one of the eigenmodes $\tilde{\Omega}_n$ of the tail. Under these circumstances, the behaviour of the coil is the same as for the gravitational coil analysed in §6.5.

6.6.2 Forcing of the tail by the coil away from resonance

In §3.6 we analysed the behaviour of a forced tail that is governed primarily by a balance between centrifugal acceleration and hoop stress. We saw that the Coriolis acceleration of the thread is negligible provided the coiling frequency is not close to one of the eigenfrequencies of an unforced thread. In this case the motion of the tail in the x and y directions are decoupled at leading order, which means that the deflection of the tail is in the same direction as the stress exerted on it by the coil.

We reuse (6.5.14) to link the stress component $\tilde{\phi}_x$ to the rescaled coiling frequency $\tilde{\Omega}$ by

$$\tilde{\phi}_x = 0.198\tilde{\Omega} + O(\tilde{\Omega}^3), \quad (6.6.3)$$

while the stress component $\tilde{\phi}_y = O(\tilde{\Omega}^2)$. These stress components must match smoothly towards the bottom of the tail, and excite motion in the tail. We model this forcing empirically by prescribing (in the original unscaled dimensionless variables)

$$N_x = 0.198 \frac{\pi a_c^2 \delta_g^2 \Omega}{U_c} \quad \text{and} \quad N_y = 0 \quad \text{at} \quad z = \delta_g, \quad (6.6.4)$$

which is obtained through substitution of (6.3.1*b,d*) into (6.6.3). We prescribe the forcing at $z = \delta_g$ as an approximation that represents the presence of the coil in an $O(\delta_g)$ boundary layer at the bottom of the thread. This approximation is used to patch the solution of §6.5 for the coil to the solution (3.6.14) for the tail; proper matching would require calculation of terms beyond the leading-order logarithmic variation.

For simplicity, we now focus on the behaviour of a thread of constant radius for which we have an analytic solution. However, since the behaviour of the tail is qualitatively unchanged by variations in its radius, we expect that the following arguments may equally be applied to predict the behaviour of extensible threads.

The height $z = \delta_g$ corresponds to $\tau_0 = 2\sqrt{\text{Fr}}\Omega^2\delta_g$ in the analysis in §3.6. We substitute this into the leading-order estimate (3.6.14) for the response of the tail to obtain an estimate for the displacement at the bottom of the tail. This is given by

$$\pi a_c^2 x \sim N_x \left| \frac{8J_0(2\mathcal{W}) \ln \tau_0 - 4\pi Y_0(2\mathcal{W})}{4J_0(2\mathcal{W}) + \pi\tau_0^2 Y_0(2\mathcal{W})} \right| \quad \text{and} \quad y = o(x), \quad (6.6.5)$$

where $\mathcal{W} = \Omega\sqrt{\text{Fr}}$. As in §6.5, we make the leading-order estimate that the radius at the bottom of the tail is equal to the coiling radius so that $x = R$. We substitute this together with (6.6.4) and $R = U_c/\Omega$ into (6.6.5) to obtain

$$\frac{U_c^2}{0.198\Omega^2\delta_g^2} = \left| \frac{8J_0(2\mathcal{W}) \ln \tau_0 - 4\pi Y_0(2\mathcal{W})}{4J_0(2\mathcal{W}) + \pi\tau_0^2 Y_0(2\mathcal{W})} \right|. \quad (6.6.6)$$

The rescaled coiling frequency is given by $\mathcal{W} = \Omega\sqrt{\text{Fr}}$; we substitute this into (6.6.6) to obtain

$$\frac{\text{Fr}}{\delta_g^2} = \frac{0.198\mathcal{W}^2}{U_c^2} \left| \frac{8J_0(2\mathcal{W}) \ln \tau_0 - 4\pi Y_0(2\mathcal{W})}{4J_0(2\mathcal{W}) + \pi\tau_0^2 Y_0(2\mathcal{W})} \right|, \quad \mathcal{W} = \Omega\sqrt{\text{Fr}}. \quad (6.6.7)$$

This is an implicit equation for the coiling frequency Ω as a function of ϵ and Fr .

Figure 6.12 compares this estimate against the value calculated numerically by solving the full system (6.2.1*a-e*), (6.2.3) and (6.2.4) of coiling equations for a thread whose radius is constant ($U = a = 1$) and for values of ϵ equal to 4×10^{-5} and 2.5×10^{-6} . There is a fairly good empirical fit.

6.7 Summary and discussion

In this chapter we have analysed the structure of a steadily coiling thread in the asymptotic limit of a very slender thread. We have focussed on the dynamic interactions between the coil and the tail, and have thereby obtained quantitative estimates for the coiling frequency

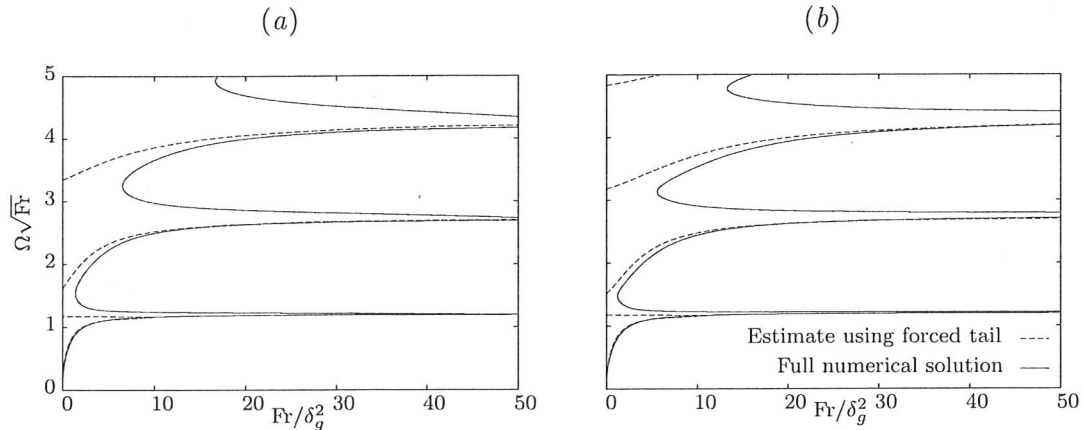


Figure 6.12: Plot of $\mathcal{W} = \Omega\sqrt{\text{Fr}}$ against Fr/δ_g^2 , calculated for a thread whose radius is constant ($U = a = 1$) by solving the full coiling problem (6.2.1a–e), (6.2.3) and (6.2.4) numerically and estimated by (6.6.7). The parameter values used are (a) $\epsilon = 4 \times 10^{-5}$ and (b) $\epsilon = 2.5 \times 10^{-6}$. There is reasonable agreement despite the rather empirical nature of the estimate.

and radius. These estimates improve on previous scaling laws that are based only on force balances in the coil.

We summarise the force balances that govern coiling in each of the regimes considered in table 6.1 and compare the scalings derived here with those derived by R06b. To facilitate this comparison, we note that their parameters are given by

$$\hat{H} \sim \text{Fr}^{1/3}, \quad \hat{\Omega} \sim \text{Fr}^{1/3}\Omega \quad \text{and} \quad \Pi_1 \sim \epsilon^{-6/5}\text{Fr}^{-4/5}. \quad (6.7.1)$$

Their scaling $\hat{\Omega} \sim \hat{H}^2\Pi_1^{5/12}$ for the coiling frequency in the gravitational regime corresponds to $\Omega \sim \epsilon^{1/2}$, and is missing the logarithmic factor in (6.5.15) due to omission of the effects of the tail. They estimate the onset of inertio–gravitational coiling by $\hat{H} \sim \Pi_1^{-1/6}$, which corresponds to $\text{Fr} \sim \epsilon$ and again misses the logarithmic factor owing to the influence of the tail. They estimate that inertio–gravitational coiling persists until $\hat{H} \sim \Pi_1^{-5/48}$, which is consistent with the conclusion that inertia is dominant in the coil when $\text{Fr} \gg \epsilon^{1/2}$. When $\text{Fr} \lesssim \epsilon^{1/2}$ and the tail is close to resonance, inertia is comparable with viscosity and gravity in the coil, and the tail appears to be governed by a balance between inertia and gravity, with no significant forcing by bending stress at the bottom (R06b). The quantitative structure of the coil in this regime remains an open question.

When $\hat{H} \gg \Pi_1^{-5/48}$, or $\text{Fr} \gg \epsilon^{1/2}$ in the notation used here, coiling falls within the inertial regime. The scaling obtained by R06b for the coiling frequency was $\hat{\Omega} \sim (\hat{H}/\mathcal{H})^{10/3}\Pi_1^{5/9}$, where

$$\mathcal{H}(\hat{H}) \propto U_c^{-1/2}(\text{Fr}) \quad (6.7.2)$$

represents the extent to which the coiling speed is decreased relative to the extensional velocity scale owing to inertia in the tail. Maleki *et al.* (2004) obtained $\mathcal{H}(\hat{H})$ numerically,

Regime	Stress balance in coil	Horizontal stress balance in tail	Vertical stress balance in tail
$Fr \ll \epsilon \ln \epsilon$ Gravitational $\Omega \sim U_f (\epsilon \ln \epsilon)^{-1/2}$	Bending Gravity	Hoop stress Forcing from coil	Gravity Extensional stress
$\epsilon \ln \epsilon \lesssim Fr \lesssim \epsilon^{1/2}$ Inertio-gravitational, <i>away from resonance</i> $\Omega \sim U_f \epsilon^{-1/2}$	Bending Gravity	Hoop stress Centrifugal acceleration Forcing from coil	Gravity Extensional stress
$\epsilon \ln \epsilon \lesssim Fr \lesssim \epsilon^{1/2}$ Inertio-gravitational, <i>near resonance</i> $\Omega \sim U_f \epsilon^{-1/2}$	Bending Gravity Inertia	Hoop stress Centrifugal acceleration Coriolis acceleration	Gravity Extensional stress
$\epsilon^{1/2} \ll Fr \ll 1$ Inertial $\Omega \sim Fr^{1/3} U_c^{5/3} \epsilon^{-2/3}$	Bending Inertia	<i>Very small deflection in tail</i>	Gravity Extensional stress
$1 \ll Fr$ Inertial $\Omega \sim Fr^{-1/2} \epsilon^{-2/3}$	Bending Inertia	<i>Very small deflection in tail</i>	Gravity Momentum flux

Table 6.1: The stress balances that govern the motion of the thread, for each of the regimes considered in the preceding sections. The stress balances for the resonant case of the inertio-gravitational regime have been taken from R06b.

but (in the absence of surface tension) \mathcal{H} may be obtained analytically using the solution (3.1.13) that satisfies both the nozzle velocity condition and the stress condition (6.4.8). Here we state that the estimate $\hat{\Omega} \sim (\hat{H}/\mathcal{H})^{10/3} \Pi_1^{5/9}$ corresponds to $\Omega \sim U_c^{5/3} Fr^{1/3} \epsilon^{-2/3}$ which is consistent with (6.4.9).

In the regime $Fr \gg 1$, inertia is dominant both in the coil and in the tail. The upward force exerted by the coil on the tail above it gives rise to a boundary layer at the bottom of the tail which is under compression. The lengthscale of this boundary layer is independent of bending stress in the coil at leading order, and therefore remains $O(Fr^{-1/2})$ as $\epsilon \rightarrow 0$. Since a very slender thread has a very small bending resistance, it might be anticipated that this boundary layer could be unstable to buckling, and hence that inertial coiling could be unstable when $Fr \gg 1$. Conversely, this potential instability might be suppressed through the advection of perturbations towards the coil before they have time to grow. Laboratory and numerical experiments to date involve values of Fr small enough that the deceleration at the bottom of the tail is fairly small. Possible avenues for future research include laboratory experiments at larger fall heights, and performing a linear stability analysis of steady fluid coiling (Ribe *et al.*, 2006a) for $Fr \gg 1$.

R06c noted that there is a close correspondence between the coiling speed U_c of a fluid thread and the critical belt speed \bar{U}_b^* below which the same thread is unstable to meandering when it is dragged by a belt. The coiling frequency was also found to be close to the frequency of meandering at onset. At first sight the two phenomena appear to be unrelated due to their differing geometries. However, the results of chapter 5 and §6.5 now reveal a clear link between the two phenomena for fall heights small enough that inertia is negligible in the tail:

For both steady coiling and the onset of meandering of a dragged thread, the frequency of unsteady motion (coiling or meandering) is governed at leading order by a balance between bending forces at the bottom of the thread and the tension in the tail. This similarity is manifested in the relationships $\sigma^* = (0.198 \ln \delta_g^{-1})^{-1/2}$, from (5.4.6), for the dimensionless meandering frequency at onset, and $\tilde{\Omega} = (0.198 \ln \delta_g^{-1})^{-1/2}$, from (6.5.15*b*), for the dimensionless coiling frequency. The solution structure of a coiling thread when $\text{Fr} \ll \epsilon \ln \epsilon$ is also very similar to that of the neutrally-stable linear eigenmode of a dragged thread for which inertia is negligible. At leading order, the coil behaves like a two-dimensional heel that rolls along the surface with velocity $U_c \mathbf{e}_y$ in the plane $x = R$. This is analogous to the leading-order behaviour of the eigenmode in the dragged thread problem, which is simply a heel rolling with velocity $U_b \mathbf{e}_x$ after being translated sideways into the plane $y = \hat{A} e^{\sigma t}$. For both steady coiling and neutrally-stable meandering, the leading-order solution requires a small correction so that the (very long) tail satisfies pinning conditions at the nozzle. In the coiling problem, this correction involves an $O(\tilde{\Omega})$ modification in the x direction. Since $\tilde{\Omega} \tilde{R} = 1$, this correction is $O(\tilde{R} \tilde{\Omega}^2)$ and is analogous to the $O(\hat{A} \sigma^2)$ correction in (5.5.4*b*) that is in phase with the leading-order out-of-plane displacement of the eigenmode for the dragged-thread problem.

In §6.6 we made progress towards understanding the physical processes that govern the thread in the ‘inertio-gravitational’ regime. We have given empirical evidence that the tail behaves like a forced circular pendulum, and have thereby built on the observation of R06b that the tail exhibits a resonant behaviour when the coiling frequency is close to an eigenfrequency of a ‘free whirling string’. R06b also found (through numerical calculation) that inertia is unimportant in the coil when the thread is not close to resonance. We have shown analytically that this is indeed the case. However, while the forcing caused by bending stress in the coil is the same as that for gravity-dominated coiling in §6.5, centrifugal acceleration of the tail changes the forced response of the tail.

We note that the correspondence between steady coiling and neutrally stable meandering applies also to heights of fall that correspond to the inertio-gravitational regime. A possible avenue for future research is therefore to extend the above analogy between meandering and coiling in the gravitational regime to analyse the onset of meandering of

dragged threads when the height of fall is large enough that inertia is significant in the tail.

While the results of §6.6 provide some insight into the physical processes that govern coiling in the inertio-gravitational regime, there are several ways in which it could be extended and placed on a more rigorous footing. The estimate (6.6.7) was derived by modelling the effect of the coil through prescribing a force at a height $z = \delta_g$ that corresponds roughly to the height of the coiling region. A more accurate estimate may instead be obtained through calculation of higher-order terms concerning the matching between the tail and the coil. Coriolis acceleration of the tail was also neglected, which is not valid when the coiling frequency $\tilde{\Omega}$ is close to one of the eigenfrequencies $\tilde{\Omega}_n$ of an unforced thread. This is a possible reason that the estimate (6.6.7) does not agree with the numerical calculation in figure 6.12 when $\Omega \approx \Omega_n$. The analysis should therefore be extended by modifying the estimate (6.6.5) of the deflection of a forced thread so that it includes the effects of Coriolis acceleration.

CHAPTER 7

CLOSING REMARKS

This thesis has analysed the physical processes that govern the bending and buckling of a slender fluid thread as it falls through air and lands onto a horizontal surface. Here I summarise the results obtained in the preceding chapters, and describe some of the aspects that merit further investigation.

7.1 Summary of results

The steady fall of a viscous thread onto a moving belt was analysed in chapter 4. While the bending resistance of a slender thread is small, it is nonetheless important in a short boundary layer near the belt, where it balances hoop stress and gravity. There is negligible variation in the radius of the thread in this boundary layer. After nondimensionalising with respect to scalings that are appropriate near the belt, the behaviour of the boundary layer can be described by a single parameter that is related to the relative sizes of the belt speed and the free-fall speed of the thread. There are two limiting cases, which correspond to the belt speed being much larger or much smaller than the free-fall speed.

In the case that the belt speed is much smaller than the free-fall speed, the thread forms a backward-facing 'compressional heel'. In this regime the thread must slow down before it lands on the belt, which places the bottom of the thread under vertical compression. This compression is supported by bending stresses in the heel. The shape of this heel is unique up to a rescaling of variables. In the case that the belt speed is much larger than the free-fall speed, the thread is instead dragged out to form a catenary-like shape, with a 'curvature-adjustment layer' at the bottom across which the shape of the thread is slightly modified so that rolling conditions are satisfied at the belt. This 'curvature-adjustment layer' is also unique up to a rescaling of variables. The intermediate regime matches smoothly between the compressional-heel and curvature-adjustment solutions, and the solutions are governed by a balance between bending stress and gravity.

The stability of a steadily dragged thread to a meandering instability was analysed in chapter 5. Near the onset of meandering the thread forms a backward-facing heel which is able to support some, but not much compression. The pinning of the thread at the nozzle causes there to be a restoring force that is exerted on the heel, which prevents the thread from falling sideways indefinitely. The meandering frequency at onset can be estimated by means of a balance between the restoring force in the tail and bending stress in the heel. At leading order, the thread is stable if bending stresses in the heel pull the tail in the same direction as the belt motion, and is unstable if bending stresses instead push the tail in the opposite direction.

Steady fluid coiling was analysed in chapter 6. For fall heights large enough that extensional stress is significant, the bottom of the thread forms a 'coil' where bending stress is important, and the remainder of the thread forms a tail in which bending stress is negligible. The tail plays a significant role during coiling. The interaction between the tail and the coil must be considered in order to make an accurate prediction of the coiling frequency. For very large fall heights, the coil is governed by a balance between centrifugal and bending stresses, and the inertial-coil solution is unique up to a rescaling of parameters. The coil exerts an upward vertical stress on the tail, and if the fall of the tail is dominated by an inertia-gravity balance, then this stress gives rise to a boundary layer at the bottom of the tail where the thread decelerates but does not bend.

If the fall height is small enough that inertia is negligible both in the coil and in the tail, then the motion of the thread is governed by a balance between bending forces in the coil and the restoring force in the tail that is caused by the pinning of the tail at the nozzle. The dynamical role of the tail during steady gravitational coiling is closely analogous to the role of the tail during neutrally-stable meandering of a dragged thread. If the fall height is within the narrow range that corresponds to the 'inertio-gravitational' regime, then the tail typically behaves like a forced circular pendulum. In this case the forcing is due to the balance of bending stress with gravitational stress in the coil.

7.2 Future work

The examination of inertio-gravitational coiling in §6.6 has yielded evidence in support of the hypothesis that the tail behaves as a forced pendulum. However, more detailed analysis is required before a more rigorous argument can be made. For example, the matching between the tail and the coil should be considered at higher orders than have been calculated here. The matching conditions obtained should significantly improve the rather ad-hoc ‘patching’ conditions described in §6.6. These matching conditions would also allow the use of a truncated domain, similar to that used in §6.5, which would allow calculations to be performed for extremely slender threads and the asymptotic behaviour of the thread to be examined in far more detail. The higher-order matching conditions are also likely to include terms that relate the rescaled stress $\tilde{\phi}_x$ to the rescaled coiling frequency $\tilde{\Omega}$ at higher order than the linear expansion (6.5.15*b*), which should yield more accurate predictions of the coiling frequency even for values of ϵ that are not extremely small.

The behaviour of a steadily coiling thread whose frequency is close to one of the eigenfrequencies of an unforced thread has not been considered. The precise role of bending stress in this regime remains an open problem whose solution requires a detailed analysis of the dynamic interaction between the coil and the tail.

If the fall height is such that steady coiling falls within the ‘inertio-gravitational’ regime, R06c observed a close correspondence between the coiling frequency of the thread, and the neutrally-stable meandering frequency of the thread when it is instead dragged by a moving belt. The similarities drawn between coiling and meandering in §6.7 suggest that once coiling in the inertio-gravitational regime is properly understood, it should be straightforward to re-apply the analysis to understand the onset of meandering in the same regime.

The analysis in §6.4 suggests that for very large fall heights, a steadily coiling thread has a region above the coil where the thread is under compression and yet which does not bend. The stability of this solution is an open question, but it should be straightforward to resolve by means of laboratory experiments or a linear perturbation analysis.

The effects of surface tension on the thread have not been considered in much detail, but they may readily be incorporated into the analysis of the preceding sections through recalculation of the behaviour of the tail and by rescaling \tilde{N}_3 in the boundary layer according to (3.2.7). The main effect of surface tension is that the tail is thinned more rapidly as it falls. Consequently, the thread diameter is smaller near the belt than if the effects of surface tension were omitted. Since the asymptotic estimates derived apply for very slender threads, it might be anticipated that their accuracy improves when surface tension is included. This hypothesis should be confirmed through numerical calculation.

BIBLIOGRAPHY

- BARNES, G. & MACKENZIE, J. 1959 Height of fall versus frequency in liquid rope-coil effect. *American Journal of Physics* **27**, 112–115.
- BARNES, G. & WOODCOCK, R. 1958 Liquid rope-coil effect. *American Journal of Physics* **26**, 205–209.
- BATCHELOR, J., BERRY, J. P. & HORSFALL, F. 1973 Die swell in elastic and viscous fluids. *Polymer* **14**, 297–299.
- BLAKE, K. R. & BEJAN, A. 1984 Experiments on the buckling of thin fluid layers undergoing end compression. *Journal of Fluids Engineering* **106**, 74–79.
- BROWN, D. R. 1960 A study of the behaviour of a thin sheet of moving liquid. *Journal of Fluid Mechanics* **10**, 297–305.
- BUCKMASTER, J. D., NACHMAN, A. & TING, L. 1978 The buckling and stretching of a viscida. *Journal of Fluid Mechanics* **69**, 1–20.
- CHIU-WEBSTER, S. & LISTER, J. R. 2006 The fall of a viscous thread onto a moving surface: a 'fluid mechanical sewing machine'. *Journal of Fluid Mechanics* **569**, 89–111.
- CLARKE, N. S. 1966 A differential equation in fluid mechanics. *Mathematika* **13**, 51–53.

- CLARKE, N. S. 1968 Two-dimensional flow under gravity in a jet of viscous liquid. *Journal of Fluid Mechanics* **31**, 481–500.
- CRUICKSHANK, J. O. 1988 Low-Reynolds number instabilities in stagnating jet flows. *Journal of Fluid Mechanics* **193**, 111–127.
- CRUICKSHANK, J. O. & MUNSON, B. R. 1981 Viscous fluid buckling of plane and axisymmetric jets. *Journal of Fluid Mechanics* **113**, 221–239.
- CRUICKSHANK, J. O. & MUNSON, B. R. 1982 An energy loss coefficient in fluid buckling. *Physics of Fluids* **25**, 111935.
- CUBAUD, T. & MASON, T. G. 2009 High-viscosity fluid threads in weakly diffusive microfluidic systems. *New Journal of Physics* **11**, 075029.
- DEWYNNE, J. N., HOWELL, P. D. & WILMOTT, P. 1994 Slender viscous fibres with inertia and gravity. *Quarterly Journal of Mechanics & Applied Mathematics* **47**, 541–555.
- DOEDEL, E. J. 2007 *AUTO-07P: Continuation and bifurcation software for ordinary differential equations*. Available at <http://indy.cs.concordia.ca/auto/>.
- DYSON, R. J. 2007 Mathematical modelling of curtain coating. PhD thesis, University of Oxford.
- EGGERS, J. 1997 Nonlinear dynamics and breakup of free-surface flows. *Reviews of Modern Physics* **69**, 865–929.
- ENTOV, V. M. & YARIN, A. L. 1984 The dynamics of thin liquid jets in air. *Journal of Fluid Mechanics* **140**, 91–111.
- FITT, A. D., FURUSAWA, K., MONRO, T. M. & PLEASE, C. P. 2001 Modelling the fabrication of hollow fibers: Capillary drawing. *Journal of Lightwave Technology* **19**, 1924–1931.
- GOLDSTEIN, H. 1980 *Classical Mechanics*. Reading, MA: Addison-Wesley.
- GOREN, S. L. & WRONSKI, S. 1966 The shape of low-speed capillary jets of newtonian liquids. *Journal of Fluid Mechanics* **25**, 185–198.
- GOTZ, T., KLAR, A. & WEGENER, R. 2008 Numerical evidence for the non-existence of stationary solutions of the equations describing rotational fiber spinning. *Mathematical Models and Methods in Applied Sciences* **18**, 1829–1844.
- GRIFFITHS, I. M. & HOWELL, P. D. 2008 Mathematical modelling of non-axisymmetric capillary tube drawing. *Journal of Fluid Mechanics* **605**, 181–206.

-
- GRIFFITHS, R. W. & TURNER, J. S. 1988 Folding of viscous plumes impinging on a density or viscosity interface. *Geophysical Journal* **95**, 397–419.
- GUILLOU-FROTTIER, L., BUTTLES, J. & OLSON, P. 1995 Laboratory experiments on the structure of subducted lithosphere. *Earth and Planetary Science Letters* **133**, 19–34.
- HLOD, A. 2009 Curved jets of viscous fluid: Interactions with a moving wall. PhD thesis, Eindhoven University of Technology.
- HLOD, A., AARTS, A. C. T., VAN DE VEN, A. A. F. & PELETIER, M. A. 2007 Mathematical model of falling of a viscous jet onto a moving surface. *European Journal of Applied Mathematics* **18**, 659–677.
- HOWELL, P. D. 1996 Models for thin viscous sheets. *European Journal of Applied Mathematics* **7**, 321–343.
- HUANG, H., MIURA, R. M., IRELAND, W. P. & PUIL, E. 2003 Heat-induced stretching of a glass tube under tension: Application to glass microelectrodes. *SIAM Journal on Applied Mathematics* **63**, 1499–1519.
- HUNT, R. 2002 Numerical solution of the flow of thin viscous sheets under gravity and the inverse windscreen sagging problem. *International Journal for Numerical Methods in Fluids* **38**, 533–553.
- LOVE, A. E. H 1944 *The Mathematical Theory of Elasticity*. Dover, New York.
- MAHADEVAN, L., RYU, W. S. & SAMUEL, A. D. T. 1998 Fluid ‘rope trick’ investigated. *Nature* **392**, 140.
- MAHADEVAN, L., RYU, W. S. & SAMUEL, A. D. T. 2000 Correction: Fluid ‘rope trick’ investigated. *Nature* **403**, 502.
- MALEKI, M., HABIBI, M., GOLESTANIAN, R., RIBE, N. M. & BONN, D. 2004 Liquid rope coiling on a solid surface. *Physical Review Letters* **93**, 214502.
- MALEKI, M., HABIBI, M., GOLESTANIAN, R., RIBE, N. M. & BONN, D. 2006 Dynamics of liquid rope coiling. *Physical Review E* **74**, 066306.
- MARHEINEKE, N. & WEGENER, R. 2009 Asymptotic model for the dynamics of curved viscous fibres with surface tension. *Journal of Fluid Mechanics* **622**, 345–369.
- MATOVICH, M. A. & PEARSON, J. R. A. 1969 Spinning a molten threadline. Steady-state isothermal viscous flows. *Industrial and Engineering Chemistry Fundamentals* **8**, 512–520.

- MORRIS, S. W., DAWES, J. H. P., RIBE, N. M. & LISTER, J. R. 2007 The meandering instability of a viscous thread. *Physical Review E* **77**, 066218.
- MUNSON, B. R. 1981 Viscous buckling of slender horizontal jets. *Physics of Fluids* **24**, 1780–1783.
- RIBE, N., BADR, S. & MORRIS, S. 2009 Cowboy Fluid Mechanics: Lariat Modes of a Viscous Rope. *APS Meeting Abstracts* pp. B8+.
- RIBE, N. M. 2001 Bending and stretching of thin viscous sheets. *Journal of Fluid Mechanics* **433**, 135–160.
- RIBE, N. M. 2002 A general theory for the dynamics of thin viscous sheets. *Journal of Fluid Mechanics* **457**, 255–283.
- RIBE, N. M. 2003 Periodic folding of viscous sheets. *Physical Review E* **68**, 036305.
- RIBE, N. M. 2004 Coiling of viscous jets. *Proceedings of the Royal Society of London A* **460**, 3223–3239.
- RIBE, N. M., HABIBI, M. & BONN, D. 2006a Stability of liquid rope coiling. *Physics of Fluids* **18**, 084102.
- RIBE, N. M., HUPPERT, H. E., HALLWORTH, M. A., HABIBI, M. & BONN, D. 2006b Multiple coexisting states of liquid rope coiling. *Journal of Fluid Mechanics* **555**, 275–297.
- RIBE, N. M., LISTER, J. R. & CHIU-WEBSTER, S. 2006c Stability of a dragged viscous thread: Onset of “stitching” in a fluid-mechanical “sewing machine”. *Physics of Fluids* **18**, 124105.
- SENCHENKO, S. & BOHR, T. 2005 Shape and stability of a viscous thread. *Physical Review E* **71**, 056301.
- SKOROBOGATIY, M. & MAHADEVAN, L. 2000 Folding of viscous sheets and filaments. *Europhysics Letters* **52**, 532–538.
- TAYLOR, G. I. 1968 Instability of jets, threads and sheets of viscous fluid. *Proceedings of the 12th International Congress of Applied Mathematics* .
- TCHAVDAROV, B., YARIN, A. L. & RADEV, S. 1993 Buckling of thin liquid jets. *Journal of Fluid Mechanics* **253**, 593–615.
- TEICHMAN, J. & MAHADEVAN, L. 2001 The viscous catenary. *Journal of Fluid Mechanics* **478**, 71–80.

-
- TIMOSHENKO, S. P. & GOODIER, J. N. 1970 *Theory of Elasticity*. McGraw-Hill, New York.
- TOME, M. F. & MCKEE, M. 1999 Numerical simulation of viscous flow: Buckling of planar jets. *International Journal for Numerical Methods in Fluids* **29**, 705–718.
- TROUTON, F. T. 1906 On the coefficient of viscous traction and its relation to that of viscosity. *Proceeding of the Royal Society London A* **77**, 426–440.
- TUCK, E. O., STOKES, Y. M. & SCHWARTZ, L. W. 1997 Slow slumping of a very viscous liquid bridge. *Journal of Engineering Mathematics* **32**, 27–40.
- UNILEVER 2006 Production line shots: Vienetta. Movie clip viewable at <http://www.unilever.com/mediacentre/multimedia/foods/Vienetta.aspx>.
- WHITTAKER, E. T. 1944 *A treatise on the analytical dynamics of particles and rigid bodies*. New York: Dover.
- WILSON, S. D. R. 1988 The slow dripping of a viscous fluid. *Journal of Fluid Mechanics* **190**, 561–570.
- YAMAMURA, M., SUEMATSU, S., KAJIWARA, T. & ADACHI, K. 2000 Experimental investigation of air entrainment in a vertical liquid jet flowing down onto a rotating roll. *Chemical Engineering Science* **55**, 931–942.
- YARIN, A.L. & TCHAVDAROV, B.M. 1996 Onset of folding in plane liquid films. *Journal of Fluid Mechanics* **307**, 85–99.